ECAP-2019-003

Towards a new Analysis of the Super Star Cluster Westerlund 1

Master's Thesis in Physics

Presented by
Jacqueline Catalano
28.03.2019

Erlangen Centre for Astroparticle Physics
Physikalisches Institut I
Friedrich-Alexander-Universität Erlangen-Nürnberg

Supervisors: Prof. Dr. Christopher van Eldik and Prof. Dr. Manami Sasaki

Abstract

The open stellar cluster Westerlund 1 was discovered in the early 1960's and is one of the most massive clusters in our Galaxy. It is located in the Galactic plane and hosts $\sim$ 80-150 very massive ($> 50\,\mathrm{M}_\odot$) young stars. In stellar clusters several objects can produce relativistic electrons and protons which create very high energy γ-rays and perhaps non-thermal X-rays. In order to distinguish between a hadronic and leptonic origin of the γ-ray emission, multi-wavelength observations are useful.

In this thesis, analysis of γ-ray data from the H.E.S.S. telescope as well as X-ray measurements from the *XMM-Newton* telescope are presented. The γ-ray analysis was carried out with the open source analysis tool *ctools* which applies a new method to analyze γ-ray data. One of the advantages using *ctools* for the analysis of this very extended source is its approach to describe the full field of view at once. This removes the necessarity to find source-free regions in the same field of view as used in the standard analysis technique. A step-by-step derivation of a field of view model of Westerlund 1 is given as well as spectral studies of the emission regions around Westerlund 1. Furthermore, the spectra were modeled with different radiative models (inverse Compton, π^0 decay).

X-ray images show some diffuse emission around the position of Westerlund 1. Unfortunately, there were no useable observations taken in regions for which an excess of γ-rays is apparent. No filaments or rims are found in the X-ray data. In addition, it was tested if these measured X-rays could be of non-thermal origin, e.g. synchrotron photons arising when eletrons are deflected in magentic fields. Indeed, a non thermal component was found in the data.

Contents

1 Motivation

Stellar clusters host a number of stars around the same age but perhaps in different stages of their evolution depending on their initial mass (Irrgang, 2018). These clusters are assumed to be a source of high energy cosmic rays which are accelerated in shocks of stellar winds of massive stars or of supernovae, between colliding winds of massive binaries and at turbulances in superbubbles inflated by stellar winds and supernovae (HESS Collaboration, 2011). These high or even very high energetic particles can create γ-rays via the inverse Compton process in the case of accelerated leptons (e.g. electrons) or via the decay of neutral pions into two high energy photons when relativistic hadrons (protons) interact with target material. Electrons representing the leptonic channel could also create synchroton radiation in the X-ray regime when they get deflected by magnetic fields (Longair, 2011). Around stellar clusters diffuse γ-ray emission is measured with space-based telescopes like the Large Area Telescope on board of the *Fermi* satellite (Ohm et al., 2013) and ground-based ones like H.E.S.S. (HESS Collaboration, 2011), MAGIC (MAGIC Collaboration, 2019) or VERITAS (Weinstein, 2015) but it is still unclear where these γ-rays come from. The young and most massive stellar super cluster in our Galaxy, Westerlund 1, shows a diffuse γ-ray emission with an extent of about 2.2° diameter. Therefore, it is a perfect target to investigate from which mechanism the emission could originate (HESS Collaboration, 2011). Analyzing data of instruments measuring different wavelength regimes could shed light on the origin of high energy radiation in Westerlund 1. Consequently, an analysis of γ-ray data from the H.E.S.S. instrument and X-rays measured by the EPIC camera on board of the *XMM-Netwon* satellite was carried out to investigate the radiation observed from Westerlund 1.

The classical way of analyzing γ-ray data from the H.E.S.S. telescope is the so called *On-Off* analysis. Here, a source region (*On* region) containing the source is analyzed, for deriving appropriate background estimates, *Off* regions, not containing any γ-ray source, are chosen in the same field of view (Berge et al., 2007). But applying this technique makes the analysis of diffuse and extended γ-ray sources almost impossible. A new open source software package that has been developed for the future γ-ray observatory CTA called *ctools* is able to deal with such diffuse emission because it makes use of a *template* based analysis like it is already done within the *Fermi* Collaboration. In this approach, a model containing the source and the background is used to describe the data measured within the whole field of view seen by a telescope (Cherenkov Telescope Array Analysis Software Team, 2019). The following thesis makes use of *ctools* to study the field of view around Westerlund 1 measured by H.E.S.S.

2 Introduction

The following section deals with stellar clusters, stars and phenomena occuring in these like winds of stars, colliding wind binaries, supernove, their remnants and turbulances in the magnetic field. These could lead to X-ray and γ-ray radiation arising from accelerated particles. Particle acceleration mechanisms like first- and second-order Fermi acceleration as well as origin of the radiation emitted by relativistic particles are explained.

2.1 Stellar Clusters

A stellar cluster is a group of stars which formed from the same gas cloud at the same time, leading to the same metallicity[1] and age of the stars. Therefore, members of the cluster are more strongly gravitationally bound to each other than other stars in the same region. In general, one can distinguish between two types of stellar clusters: globular clusters and open clusters. Globular clusters are long-lived (several billion years) clusters hosting a lot of old stars ($\sim 10^5$ stars), have a spherical shape and are located in the halo of a galaxy. On the other hand, open clusters are more short-lived (several hundred million years) than globular clusters. Additionally, they show a more irregular grouping of young stars in the galacic disk of a galaxy. Moreover, the number of stars contained in such open clusters is much less, only up to a few hundred (Irrgang, 2018).

2.2 High Energy Astrophysics in Stellar Clusters

2.2.1 Stars

Stars are objects that balance their own gravity with the radiation pressure arising from the nuclear fusion in the core. They can be characterized as a blackbody[2] with temperature T. The Hertzsprung-Russell diagram is the most important diagram for stellar evolution, it shows how luminosity and temperature change (Irrgang, 2018) during the stars' livetime. In Figure 1 (a) one can find an example of such a diagram with different evolutionary tracks for stars of different masses. The color indicates the color/temperature and hence the spectral class of the star (ESA, 2018a).
For this work the evolution of massive stars (M > 8 solar masses ($M_\odot$)) is shortly discussed because the stellar cluster Westerlund 1 contains mostly of very massive (and evolved) stars such as Wolf-Rayet stars and OB supergiants (Clark et al., 2005).
Massive stars experience hydrogen burning (main sequence phase) for two-thirds of their lifetime. After the central hydrogen ran out, the star is entering the Red Giant (RG) phase

[1] The metallicity describes the chemical abundance of elements (Irrgang, 2018).
[2] A blackbody is an object in thermal equilibrium emitting a continous spectrum with a specific temperature Irrgang (2018).

in which the core is contracting and heating and at the same time the radius is expanding[3]. As the core is heating up helium burning is ignated and later on also burning of heavier elements (in the following referred as metals) resulting in an onion-shell like structure of the star (see Figure 1 (b)) (Irrgang, 2018).

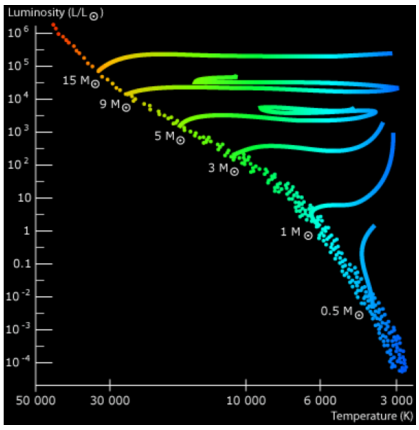

(a) Hertzsprung-Russell diagram with evolutionary tracks for stars of different masses. The color indicates the color/spectral class of the star (ESA, 2018a).

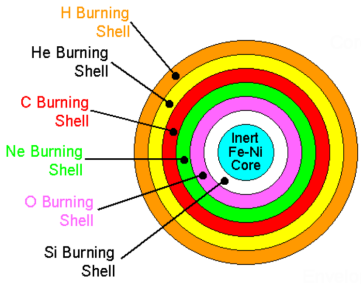

(b) Onion shell like structure of evolved stars (Pogge, 2018).

Figure 1: Evolution and spectral classification of stars.

Some stars contained in Westerlund 1 are Wolf-Rayet stars. Typical masses of Wolf-Rayet stars are ranging between 10 to 25 $M_\odot$ but can exceed up to 80 $M_\odot$. Furthermore, they evolve from O stars ($\sim$ 40000 K) (Crowther, 2007). Wolf-Rayet stars are observed close or even in star forming regions located in the Galactic Disk. One forth of the known Wolf-Rayet stars in our galaxy are hosted by massive clusters in the Galactic Center or in Westerlund 1.
On the other hand, Westerlund 1 has a rich content of OB supergiants, which are stars with the spectral class O or B (left hand side in a Hertzsprung-Russell diagram) that entered the supergiant phase (beyond the evolutionary track of 15 $M_\odot$ in Figure 1).
A large fraction of massive stars are members of binary systems (Longair, 2011). For binaries with long orbital periods (wide binary) the stars may evolve independent from each other (Crowther, 2007) but in a close binary system the stars' evolution can be strongly affected by mass transfer from one to the other star. In the end of the stars evolution within a binary there are several possible end stages.
For example, a binary consisting of a low mass white dwarf (WD) and an intermediate/high mass star, a WD binary or WD-NS (Neutron Star) binary will form. Another possibility is

[3]The Virial theorem implies that if one part of the star is contracting another one has to expand to conserve energy (Irrgang, 2018).

that one of the stars undergoes a supernova (SN) explosion connected to a considerable mass ejection leaving either a bound or unbound system (Longair, 2011).

2.2.2 Stellar Winds

In general, massive stars have mass losses, e.g. in form of ultra-violet (UV) radiation and strong line-driven winds leading to changes of the structure and evolution of the stars. Mass loss also affects the star's luminosity, temperature, lifetime, emitted radiation, He core mass and the death (Smith, 2012).
One of the major mass loss mechanism are winds (Longair, 1994) which are diven by radiation pressure arising from photons. These get absorbed by atoms in the stellar atmosphere. The transfer of the momentum to the atoms can be observed as absorption lines in the X-ray spectra. Because of that the atom is experiencing a recoil leading to a movement away from the star (Crowther, 2007) which collectively forms a stellar wind.

2.2.2.1 Evolution of a Stellar Wind

Winds have a great effect on the interstellar medium (ISM) around the star similar to that of a supernova remnant (see also 2.2.3). The arising structure of the propagating wind into the interstellar medium can be described by four zones (see Figure 2):

(a) supersonic stellar wind,

(b) hot, shocked wind mixed with swept-up material,

(c) thin, cold, dense shell with most of the swept-up material inside and

(d) ambient interstellar gas.

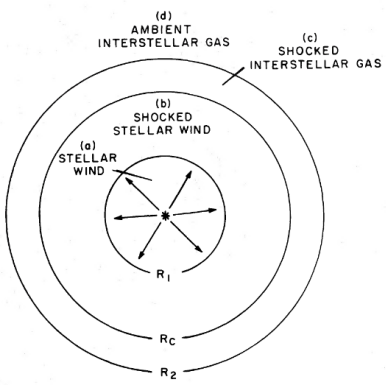

Figure 2: Schematic sketch of the outflowing wind (Weaver et al., 1997).

The first phase deals with the stellar wind expanding freely at supersonic velocity (free-expanding phase) into the ISM until the swept-up material mass is comparable to the one of the wind itself. This phase takes roughly $10 - 100$ years (Sasaki, 2017). For a typical WR star the free expansion phase into a homogenous ISM takes about 100 years.
After the free expansion phase a shock propagating inwards arises which transformes the kinetic energy of the wind into hot plasma with a temperature of about 10^7 Kelvin (region (b) in Figure 2). As gas/material of the ISM enters the contact surface it is heated up to 10^6 K. But due to line emission the swept-up material gets then cooled down to 10^4 K. This adiabatic expansion phase takes a few thousand years.
As the cool mass of the swept-up material is at some point larger than the hot wind, a thin cool shell is created (see (c) in Figure 2). The shell is expanding outward into the ISM due to the high pressure of the hot wind bubble. This phase is lasting as long as the star can provide a strong wind with higher pressure compared to the ISM. But the bubble can sustain the dissipation into the ISM if the star evolves to a SN which re-pressurizes the bubble (Ramirez-Ruiz et al., 2001).

2.2.2.2 *Diffusive Shock Acceleration*

Supersonic stellar winds of massive stars are, according to Cassé and Paul (1980), able to accelerate charged particles up to 10^{15} eV via the first-order Fermi acceleration mechanism. First discovered by Axford, Leer and Skadron (1977) and others independently in the late 1970s, the acceleration of particles by strong shock waves (first-order Fermi acceleration), also called *diffusive shock acceleration* (DSA), can be illustrated as shown in Figure 3.
Here, a shock front (vertical black line) is propagating at supersonic velocity $\mathrm{U} \gg \mathrm{c}_s$ (c_s: speed of sound) from left to right. The dark grey shaded side is called downstream and the light grey side upstream. In the rest frame of the shock, the plasma is flowing at a velocity $v_1 = U$ from upstream by crossing the shock to the downstream medium. As a consequence of a discontinuity at the shock front (see chapter 11.3 in Longair (2011)), the velocity of the shocked plasma behind the shock front is only one forth of the velocity U ($v_2 = \frac{1}{4}v_1$, for strong shocks). In the rest frame of the upstream gas the particles become isotropic by scattering off streaming instabilities and turbulences. Because the shock front moves at velocity U the downstream medium travels at $\frac{3}{4}U$ relative to the upstream medium. When particles cross the shock from the downstream to the upstream (or vice versa) they gain an average energy fraction of $\langle \frac{\Delta E}{E} \rangle = \frac{1}{2}\frac{\mathrm{U}}{c}$ (see Longair (2011)) and their velocity distribution becomes isotropic due to the aforementioned streaming instabilities and turbulances. This process happens over and over again and particles gain more and more energy until they finally escape. Calculations in Longair (2011) show that this mechanism leads to a power-law

differential energy spectrum with an index of 2:

$$N(E)\mathrm{d}E \propto E^{-2}\mathrm{d}E. \tag{1}$$

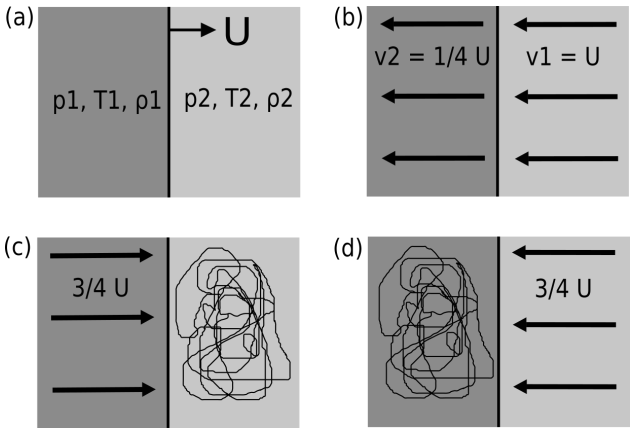

Figure 3: Illustration of the *diffuse shock acceleration* (first-order Fermi acceleration) of a strong shock. (a) A strong shock propagtes to the right-hand side with velocity U. The physically relevant parameters are given for both regions. (b) In the rest frame of the shock the flow of plasma in the upstream (in front of the shock) is $v_1 = U$, behind the shock (downstream) the velocity is $v_2 = \frac{1}{4}v_1$. (c) In the rest frame of the upstream the particle distribution is isotropic and the upstream is flowing at velocity $\frac{3}{4}$U because the shock is propagating with U. (d) When particles cross the shock they scatter, become isotropic again and the velocity of the upstream is $\frac{3}{4}$ U (modified by the author) (Longair, 2011).

However, the acceleration of particles by stellar winds is only possible under following conditions:

- supersonic stellar winds propagating in the ISM,
- continous injection of particles,
- larmor radius[4] $\mathrm{r_L} \gg$ shock thickness δ,
- mean free path $\lambda_{\mathrm{MFP}} \gg \delta$.

With typical wind velocities of $2 \cdot 10^3\,\mathrm{km\ s^{-1}}$ the constraint $\mathrm{r_L} \gg \delta$ translates into a minimal injection energy of protons and electrons of about 20 keV and 1 MeV, respectively. When the energy of a particle is high enough ($\mathrm{r_L} = \lambda$) it can leave the shock (Cassé and Paul, 1980).

[4]The larmor radius, which is also called gyroradius or cyclotron radius, is the radius of a circular motion of a charged particle in the presence of a magnetic field (Longair, 2011).

2.2.2.3 Emitted Radiation by Relativistic Particles

When a strong shock is present it accelerates all types of charged particles either leptons (dominantly electrons) or hadrons (mostly protons) via DSA. It thus produces a power-law energy spectrum as given in Equation 1 (Longair, 2011). In some ealy-type stars (OB stars) non-thermal[5] radio emission is detected which could arise from relativistic electrons deflected in magnetic fields emitting synchrotron radiation. Additionally, Pollock (1987a) suggested that non-thermal radiation in the radio regime, strong X-ray emission and possibly γ-rays from Wolf-Rayet stars arise from relativistic electrons, accelerated via the first-order Fermi mechanism. They could manifest themselves in inverse Compton scattering[6] at UV photons to X-ray and γ-ray energies, and synchrotron radio emission. In interactions of high energy protons with other protons, nuclei of atoms or even molecules of interstellar gas pions are produced. Charged pions decay into muons and they in turn decay into relativistic electrons:

$$\pi^{\pm} \rightarrow \mu^{\pm} + \overset{(-)}{\nu}_{\mu} \rightarrow e^{\pm} + \overset{(-)}{\nu}_{e} + \overset{(-)}{\nu}_{\mu} + \overset{(-)}{\nu}_{\mu}, \tag{2}$$

the neutral pion on the other hand decays into two high energy photons (Longair, 2011):

$$\pi^{0} \rightarrow 2\gamma. \tag{3}$$

2.2.2.4 Colliding Wind Binaries (CWB)

At least 40 % of Wolf-Rayet stars are members of binary systems with massive OB stars as secondary components. Such systems are brighter in X-rays than single stars indicating that additional X-ray emission is produced. These X-rays arise from collisions of stellar winds from the stars in that binary, forming a shock at the contact region (Usov, 1992).
According to Pollock (1990) in the scenario of colliding wind binaries non-thermal radio and maybe high energy X-rays (even γ-rays) can arise from relativistic shock-accelerated electrons through synchroton radiation, IC scattering and bremsstahlung[7] (Stevens, Blondin and Pollock, 1992). Because of the contact discontinuity between the winds also protons can be accelerated and create neutral pions via p-p collisions which subsequently decay into high energetic photons (Eichler and Usov, 1993).

[5] Non-thermal radiation is electromagnetic radiation not emitted by a blackbody Ridpath (2012).

[6] In the inverse Compton scattering a low energy photon will be upscattered by a high energy electron (Longair, 2011).

[7] Bremsstrahlung is electromagetic radiation emitted by an electron or positron due to deceleration in the coulomb field of a nucleus (Povh and Zetsche, 1999).

2.2.3 Supernovae and Supernova Remnants

If nuclear burning stops in the core of the star because the fuel ran out there is no thermal pressure that can prevent a collapse by gravitational forces. The core starts to contract and is transfered to a non-equilibrium state. Then there are several ways to establish a new equilibrium depending on the mass of the star, e.g. transfering to a white dwarf (WD), a neutron star (NS) or a black hole (BH) depending on the mass of the star. Collapse of the core of massive stars result in an explosion of the star, known as supernova (SN). SNe can be devided into two classes: Type I and Type II, depending on the abscence or presence of hydrogen lines (Longair, 2011). They can be characterized by the exploding mechanism as a thermonuclear or a core-collapse supernova:

- **Type Ia:** The state-of-the-art explanation of thermonuclear SNe is a disruption of a WD via an explosion caused by mass transfer of a companion leading to masses exceeding the Chandrasekhar limit $M_{Chan} = 1.4\,M_{\odot}$ of WDs. As WD are evolved stars located in the lower left corner of the Hertzsprung-Russell diagram they already stripped of their outer layers explaining the absence of hydrogen.

- **Type II, Ib, Ic:** Type II, Ib and Ic are triggered by the collapse of the core of massive stars when the star runs out of fuel. Neutrinos arising from transitions of protons to neutrons, lead to an energy release in form of kinetic energy and therefore drive the ejection of matter, referred as explosion. This transition from a massive star to a neutron star is referred as a core-collapse, the subsequent ejection of matter as the supernova (Longair, 2011).

A supernova remnant arises from the shocks of a supernova explosion. As mentioned in 2.2.2 the evolution of stellar winds and shell-type SNRs is similar and will be explained only shortly for supernova remnants in this section. The main difference between the evolution of a stellar wind bubble and a SNR is that in the case of a stellar wind bubble the injection of energy happens on a continous level whereas a one-time energy input takes place for SNe (Sasaki, 2017).
The first phase is the free expansion of the shock and ejected material into the interstellar medium at supersonic velocities. Considering a spherically symmetric expansion a characteristic shell around the former star arises. In the shocks, acceleration of particles takes place (DSA) as well as heating of the shocked material (Gaisser et al., 2016). In the heated downstream region thermal X-rays will be emitted by very hot plasma (Longair, 2011).
After several hundred years of the shock propagating the next phase is arising: the adiabatic or Sedov-Taylor phase (Gaisser et al., 2016). From here on the mass of swept up material becomes greater than the ejected mass and a deceleration of the shock velocity is apparent

(Longair, 2011). As the formed shock is reflected by swept-up ISM a reverse shock is created. This reverse shock reheats the plasma (ejected gas) which has cooled during this phase resulting in X-ray emission inside of the shell while the outer shock is further decelerating leading to possible instabilities.
The term 'snowplow' phase is often used to refer to the evolution step at which a dense cool shell arises as cooling becomes more dominant (Longair, 2011). The last phase of the evolution of supernova remants is the merging with the ISM, distributing the kinetic energy to interstellar gas (Gaisser et al., 2016).
In star-forming regions supernova remnants are common objects as well as gas and molecular clouds which could serve as target material for interactions of accelerated particles escaping from SNRs.

2.2.4 Further Phenomena

Massive stars are predominantly formed in associations by collapses of (giant) molecular clouds (see 2.1). Molecular clouds are not homogeneous, they have **clumps** with higher denisities than the cloud which can't be swept up by SNRs or stellar winds. Because shock fronts hit the clumps reflected shocks and magnetohydrodynamic (MHD) waves arise. More reflected shocks and MHD waves are created by further interactions originating from new wind phases of massive stars or SNe. The energy injection in such associations is more or less constant by the interplay of the evolution of OB stars, exploding supernovae and further star formation.
Another feature appearing around associations are **higher magnetic fields** ($10 - 20\,\mu$G) (Parizot et al., 2004) compared to the interstellar magnetic field in the Galactic Disk (few μG) (Ferriére, 2015). Also possible is that particles once accelerated by a shock can be **reaccelerated** if the time for a particle to leave the shock is much larger than between two SNe (Parizot et al., 2004).
Turbulences play an important role in all astrophysical objects in terms of acceleration. In the *diffusive shock acceleration* mechanism (first-order Fermi accerlation) turbulences are needed create an isotropic particle distribution in the down- and upstream medium (see 2.2.2), without them the shock is not able to accelerate particles at all. Another mechanism to accelerate particles is the **second-order Fermi acceleration** or *stochastic acceleration* (SA). Turbulances are also able to accelerate particles via SA in addition to just scatter them. Usually the acceleration of particles by a shock is dominant because the scattering off a turbulance happens much faster than the acceleration. For efficient SA the energy of particles have to be low and/or a strongly magnetized plasma has to be omni-present (Petrosian, 2012).

In 1949, Fermi proposed that charged particles reflected by so called magnetic mirrors[8] are able to gain energy, $\langle \frac{\Delta E}{E} \rangle = \frac{8}{3}\left(\frac{V}{c}\right)^2$ with V being the velocity of the random motion of the mirror, stochastically leading to a power-law distribution (Longair, 2011).
Connected to turbulences is the phenomenon of **magnetic reconnection** which also accelerates particles. Magnetic reconnection possibly appears if two magnetic field lines of opposite polarity converge and annihilate. Proposed by de Gouveia Dal Pino and Lazarian (2005) charged particles experience an energy gain in the reconnection region of the magnetic field lines by bouncing back and forth similar to DSA.
Another phenomenon that could arise is a so-called **superbubble** inflated by collective behavior of stellar winds and SNe, as revealed in the case for 30 Dor C in the Large Magellanic Cloud (Kavanagh et al., 2019).

2.3 Detection of X-Rays and Gamma Rays

The Earth is constantly exposed by electromagnetic radiation, cosmic radiation and neutrinos. Measuring these gives insight to emission and acceleration processes within the astrophysical sources of this radiation. As cosmic rays (CR) consist of charged particles which get deflected by interstellar and intergalactic magnetic fields they don't carry any information about the location of their source. Nevertheless, measuring them with cosmic ray detectors like the Pierre Auger Observatory gives information about the composition, spectrum, sources of cosmic rays (CRs), propagation, etc.
Neutrinos are elementary non-charged particles with almost zero mass interacting only via the weak force making the detection very difficult but point directly back to the source. Detectors like IceCube (South Pole) or KM3Net (Mediterranean Sea) have large volumes of target material in which the neutrinos can interact (Gaisser et al., 2016). Measuring neutrinos is a hint that hadronic interactions take place, e.g. in the vicinity of blazars (Ansoldi et al., 2018).
Electromagnetic radiation like γ-rays and X-rays are not deflected by magnetic fields which gives them the ability to travel in straight lines towards Earth (Gaisser et al., 2016). The Earth's atmosphere is opaque to electromagnetic radiation beyond the optical band, so that X-rays and γ-rays have to be measured either by space-based experiments or for the case of the γ-rays also indirectly by Imaging Atmospheric Cherenkov Telescopes (IACTs) on ground (Degrange and Fontaine, 2016).

[8] When magnetic field lines in a static magnetic field converge the magnetic flux density increases as well as the perpendicular kinetic energy $w_\perp$ component of particles gyrotating around magnetic field lines. Magnetic fields don't carry out any work on a particle but as the kinetic energy $w_\perp$ increases a parallel component of the particle's motion arises to compensate for that resulting in a reflection (Longair, 2011)

2.3.1 Measuring Gamma Rays with the H.E.S.S. telescope

Because this work deals with γ-rays measured with the H.E.S.S. (High Energy Stereoscopic System) instrument which is a ground-based γ-ray telescope array located in Namibia the focus is on ground-based detection of γ-rays.
Photons entering the atmosphere with energies greater than $2m_ec^2$ are able to create an electron-positron pair in the field of a nucleus. The produced electrons and positrons emit new photons in the process of bremsstrahlung. They can create new electron-positron pairs if their energy is still high enough. These processes continue until the energy is not sufficiently high anymore and a so-called electromagnetic shower or cascade arises (see Figure 4 (a)) (Longair, 2011).
Proposed by Cherenkov in 1934 charged particles emit a characteristic radiation while travelling though a solid or liquid. However, Blackett suggested that the emission of this (Cherenkov) radiation to be also apparent in gases (Degrange and Fontaine, 2016).
The electrons/positrons in the cascade can be faster than the speed of light in the atmosphere. If this is the case the aforementioned Cherenkov radiation will be emitted at frequencies lying in the optical range forming a light cone (see Figure 4 (b)) (Longair, 2011).

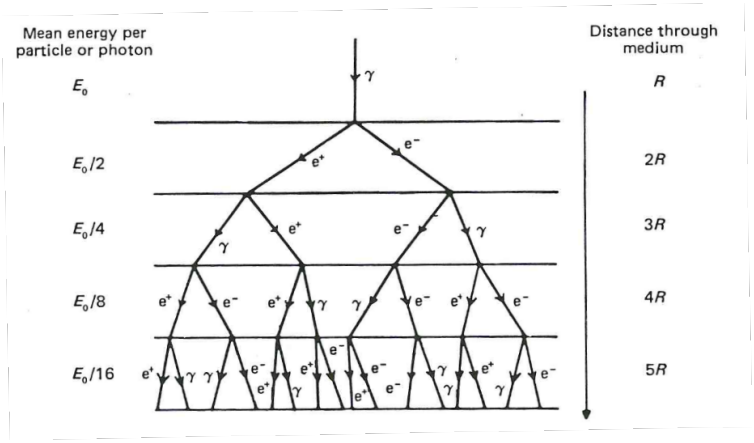

(a) Sketch of an electromagnetic cascade arising from electron positron pair production with subsequent bremsstrahlung (Longair, 2011).

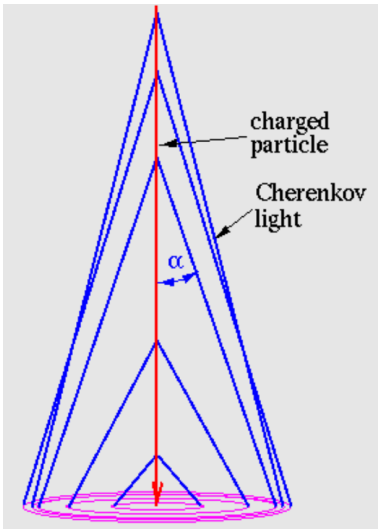

(b) Cone-like emission of Cherenkov radiation with opening angle α (Bernlöhr, 2019).

Figure 4: Illustration of a particle cascade and the subsequent arising Cherenkov radiation if the particle is faster than the local speed of light.

The shower reaches its maximum[9] at a height of about 10 km above ground and therefore illuminates an area of 250 m diameter on the ground called Cherenkov light pool. To catch a

[9]The shower maximum appears if the number of particles in the shower is the most (Hofmann, 2019).

snapshot of the shower, which is lasting only a few nanoseconds, optical telescopes should be placed within that light pool. An example of a Cherenkov telescope can be found in Figure 5 (a). It has a large mirror area collecting and reflecting the light onto a camera consisting of photomultiplier tubes. The camera captures the light via these photomultiplier tubes which are represented in Figure 5 (b) as a pixel. Measuring the amount of light captured gives information about the energy of γ-rays.

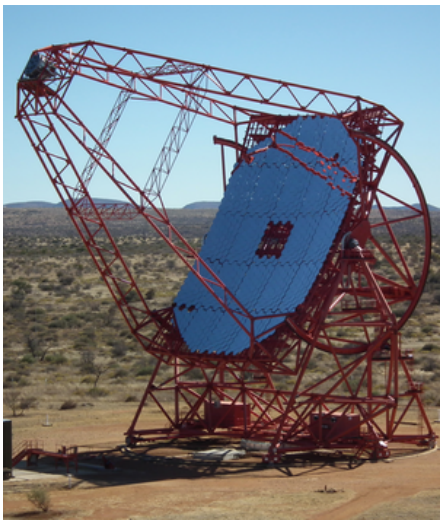

(a) One of the H.E.S.S. telescopes (Hofmann, 2019).

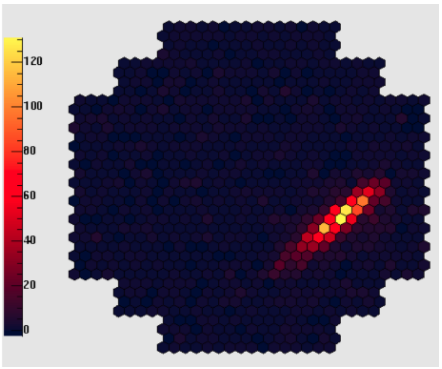

(b) Shower image of the measured Cherenkov radiation most likely of a γ-ray (Hofmann, 2019).

Figure 5: Illustration of a Cherenkov telescope as well as a detected γ-ray shower.

Figure 5 (b) shows an event measured by the H.E.S.S. telescope system (Hofmann, 2019) which is most likely a γ-ray event. The classification of events is important to distinguish between γ-rays and background events. Background events are cosmic rays such as protons or even heavier nuclei or muons created by interactions of CRs with the atmosphere. Events are discriminated by their shape in the camera. γ-rays have an elliptical shape (see Figure 5 (b)), cosmic rays show an irregular behavior with blobs and several hot spots (Shilon et al., 2018) and muons can be measured as rings (Hofmann, 2019), examples are shown in Figure 6. Measuring the shower with a single telescope gives only one view of the shower which makes the reconstruction of the γ-ray direction inaccurate. However, having more than one telesope in the Cherenkov light pool makes the reconstruction easier. The H.E.S.S. telescope has four small (12 m dish diameter) telescopes arranged in a rectangle (H.E.S.S. I) and one big (28 m dish diameter) in the middle of the array. It is operating from tens of GeV to tens of TeV with a field of view of 5° and a collecting area of 108 m^2 (small telescope) and 614 m^2 (big telescope). Furthermore, it takes measurements since 2002 in the first phase (H.E.S.S. I) and since 2012 with the whole array of five telescopes (H.E.S.S. II) with an improvement in sensitivity.

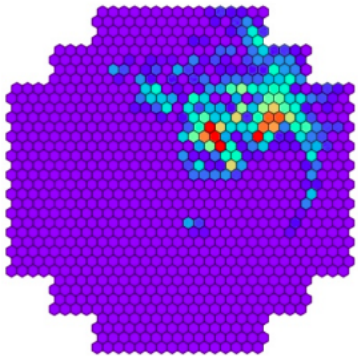

(a) Topology of a cosmic ray measured by H.E.S.S. (Shilon et al., 2018).

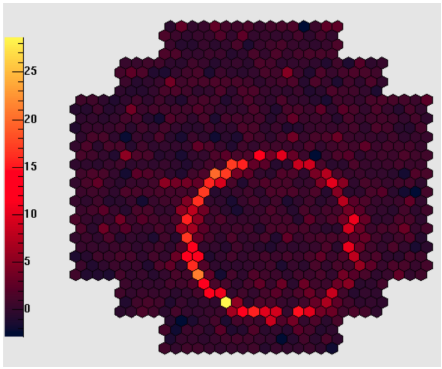

(b) Topology of a muon created by interactions in the atmosphere (Hofmann, 2019).

Figure 6: Camera images of events measured by the H.E.S.S. telescope classified as background.

The Cherenkov Telescope array (CTA) will be the next generation ground-based Cherenkov telescope with even more Cherenkov detectors spread over a larger area on the Northern and Southern hemisphere, respectively. It will have a better resolution and sensitivity than the existing systems (Cherenkov Telescope Array Observatory gGmbH , 2019).

2.3.2 Measuring X-rays with the *XMM-Newton* satellite

On contrary to γ-rays, X-rays are not energetic enough to create a particle shower in the Earth's atmosphere. Therefore, they have to be measured by space-based instruments like the *XMM-Newton* (X-ray Multi-Mirror (Strüder et al., 2001)) space observatory (see Figure 9). The space craft, launched 1999, consists of three X-ray telescopes each having 58 grazing-incident shell-like mirrors arranged coaxial to each other archieving a large effective area. This arrangement also ensures a very small grazing angle of 30 ' for being able to reflect the high energy photons (European Space Agency, 2019a). Moreover, X-rays have to be reflected twice (Snowden and Kuntz, 2019) by a paraboloid and hyperboloid mirror for X-ray imaging. X-ray baffles collimate the reflected photons and additionally reduce straylight (see Figure 64), which is arising when photons from outside the field of view are reflected only one time onto the detectors (European Space Agency, 2019a).
The camera detecting the X-ray photons is called EPIC (European Photo Imaging Camera) and consists of two MOS CCDs (Metal Oxide Semi-Conductor (European Space Agency, 2019a) Charge Coupled Devices[10] (Bignami et al., 1990)) arrays and one PN CCD (European Space Agency, 2019a).

[10]CCDs store charge carriers originating from high energy photons in potential wells at the surface of a semiconductor which can be moved by appling different voltages leading to a shift of the potential well (Boyle and Smith, 1970).

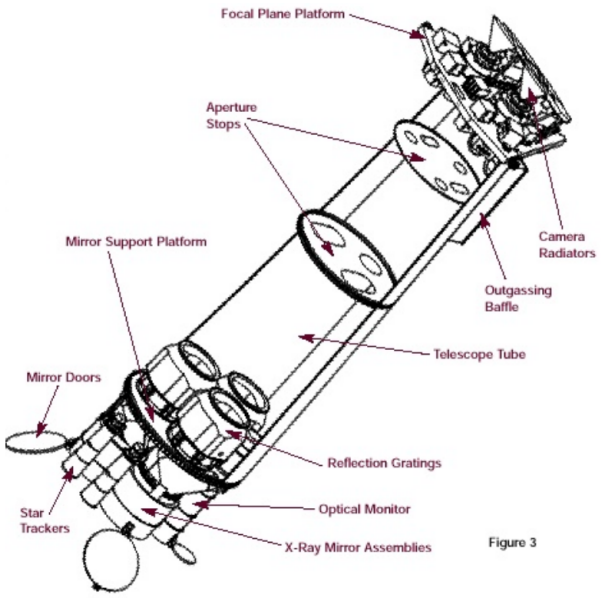

Figure 7: Sketche of the XMM-Newton satellite and one of the X-ray telescopes.

Also apparent in the detection of X-rays are backgrounds which can be divided into cosmic X-ray and instrumental background. The background of the detector can either arise from noise in the detector itself or by particles interacting with the mechanical structure or the detector. Also there are two components of the cosmic background, namely a strong rapid variation caused by soft protons ($< 100\,\mathrm{keV}$) from the sun and an internal one caused again by particles interacting with the surroundings and the detector itself (European Space Agency, 2019c).

With a field of view of $30'$ the *XMM-Newton* telescope measures X-ray with energies between $0.15 - 15\,\mathrm{keV}$ and is able to operate the CCDs in different modes (see 4.3) (European Space Agency, 2019a).

3 Westerlund 1

In this section, basic information like mass, age and distance to Westerlund 1 are introduced. Additionally, state of the art knowledge obtained from observations in different wavelength ranges (γ-ray, X-ray and radio) are presented.

3.1 Basic Information

In 1961, Bengt Westerlund found a heavily reddened[11] cluster with the Schmidt telescope of the Uppsala Southern Station in Australia (Westerlund, 1961) at the postion of right ascension R.A.(1900): 250.25 °, declination Dec(1900): −45.65 °. Later on the optical position of Westerlund 1 was determinded to be at R.A.(2000): 251.7625 ° Dec(2000): −45.8436 ° (Brandner et al., 2008). The position of Westerlund 1 within the Milky Way is directly in the Galactic Disk which habors a lot of objects and material.
Forty years later, Clark et al. (2005) performed spectroscopic and photometric observations and identified around 200 post-main sequence (MS) stars within that cluster. Around one forth of the stellar content could be classified as 14 Wolf-Rayet stars, 25 OB supergiants and 14 short lived transitional objects like hot LBVs[12] and extreme B supergiants and cool Yellow Hyper- and Red Supergiants.
Furthermore, they determined the mass of known Westerlund 1 to $\sim 10^5\,M_\odot$ by applying the IMF[13] concluding that it is the most massive young cluster in the Milky Way and even in the Local Group, a Super Star Cluster (SSC). Crowther at al. (2006) enlarged the number of Wolf-Rayet stars to 24, the OB supergiants to ~ 150 and suggest a binary fraction of Wolf-Rayet stars to be least 62 %. From the ratio of Wolf-Rayet stars to red and yellow supergiants they measured the age of Westerlund 1 to $4.5 - 5.0\,\mathrm{Myr}$. For approximating the distance Luna et al. used HI line emission and extrapolated the distance to $\sim 4.3\,\mathrm{kpc}$, Aghakhanloo et al. (2019) measured the distance of Westerlund 1 to $3.2 \pm 0.4\,\mathrm{kpc}$ using *Gaia* Data Release 2 data (Aghakhanloo et al., 2019).

3.2 Known Objects in the Field of View of Westerlund 1

Magnetar[14] CXOU J164710.2-455216: This object was discovered in 1998 at a position of R.A.: 251.7925 °, Dec: −45.9214 ° with the *Chandra X-ray Observatory* and has a distance

[11] As dust particles have a size comparable to blue light they absorb blue light and make the object appearing more red than it actually is (Swinburne University of Technology, 2019).
[12] Luminous Blue Variables are luminous blue stars with short variability (Conti, 2005).
[13] An IMF is the initial mass function of stars which gives an estimate of the number of stars in a mass interval (Kroupa, 2019).
[14] Magnetars are neutron stars with ultrastrong magnet fields which can have X-ray and γ-ray bursts (An et al., 2012).

of $2.5 - 5\,\mathrm{kpc}$ located in Westerlund 1. The period of the rotation was determined to 10.6 s. It was observed by various X-ray observatories (*Chandra*, *XMM-Newton*, *Swift* and *Suzaku*) after a short 20 ms burst measured by *Swift* BAT (Burst Alert Telescope) in 2006. Additionally, An et al. set an upper limit of the magnetic field of CXOU J164710.2-455216 to be $7 \cdot 10^{13}\,\mathrm{G}$ which is comparable small for magnetars (An et al., 2012). The X-ray luminosity is $\mathrm{L}_X = 3 \cdot 10^{33}\,\mathrm{erg\ s^{-1}}$ (Israel et al., 2007).

Low Mass X-ray Binary (LMXB) 4U 1642-45: Also called GX 340+00 the LMXB 4U 1642-45 consists of neutron stars (Miller et al., 2016) and is located at R.A.: 251.4483 °, Dec: −45.6111 ° (Université de Strasbourg/CNRS, 2019) at a distance of $8.5 - 11.8\,\mathrm{kpc}$ (van Paradijs and White, 1995). An analysis of archival *Chandra* data revealed a relativistic strong iron line around 6.9 keV. To produce such a feature a complex disk wind driven by radiative pressure, thermal driving and magnetic processes would be a plausible explaination (Miller et al., 2016). The wind's energy is estimated to $\sim 10^{39}\,\mathrm{erg\ s^{-1}}$ (Miller et al., 2016).

Pulsar PSR 1648-4611: The radio pulsar PSR 1648-4611 was found by the Parkes Multibeam Pulsar Survey at a posion of R.A.: 252.0917 °, Dec: −46.1878 °. It has a pulse period of 0.1649 s and an estimated distance of 5.7 kpc. Additionally, it is spatially consistent with the *Suzaku* source J1648-4610 and also detectable in γ-rays with energies in the GeV range with the *Fermi* LAT (Large Area Telescope). These measurements suggest the existance of a Pulsar Wind Nebula (PWN[15]) based on the spatial distribution and photon index of the diffuse emission. The X-ray luminosity expected from PSR 1648-4611 is $L_X \sim 10^{32}\,\mathrm{erg\ s^{-1}}$ in the $0.1 - 2.4\,\mathrm{keV}$ band (Sakai et al., 2013).

HESS J1640-465: Discovered during the H.E.S.S. Galactic Plane Survey HESS J1640-465 is an extended TeV γ-ray source located at R.A.: 250.18 °, Dec: −46.53 ° (HESS Collaboration, 2006). It was also measured in low energy γ-rays by *Fermi* connecting smoothly to the spectrum of very high energy γ-rays measured by H.E.S.S. (Xin et al., 2018). Due to two objects being in close approximity: a PWN (PWN J1640-4631) and a SNR shell of G338.3-0.0, it is still under debate where the γ-ray emission of HESS J1640-465 comes from. The HESS Collaboration (2014) suggested that the observed emission arises from the SNR shell at which cosmic rays can be accelerated and interact with dense gas of the HII complex G338.4+0.1. They argue that an explaination of the PWN scenario is disfavored due to the TeV morphology, recent radio data and the overall γ-ray spectrum. On the other hand Xin et al. (2018) rule out the SNR scenario because HESS J1640-465 would follow specific values comparable to a PWN scenario such as spin-down luminosity or the characteristic age (Xin et al., 2018).

[15] A PWN arises when an active pulsar loses energy in form of relativisitc particles (Sakai et al., 2013).

HESS J1641-463: HESS J1641-463 is a source which was hidden by the bright nearby source HESS J1640-465 for quite a long time and is only revealed significantly above 4 TeV (Oya et al., 2015) at a position of R.A.: 250.2588 °, Dec:−46.3036 ° (HESS Collaboration, 2014). It is spatially consistent with the SNR G338.5+0.1. So far there is also no counterpart measured in the X-ray regime. To explain the observed hard emission a hadronic scenario is favored as cosmic rays could be accelerated by the close sources G338.5+0.1 and/or G338.3+0.0 and interact with dense medium (Oya et al., 2015).

An illustration of all sources within the Westerlund 1 field of view (FoV) of H.E.S.S. is shown in Figure 8. Additional X-ray and γ-ray sources not mentioned here but measured with *XMM-Newton* and *Fermi*, respectively, are also shown.

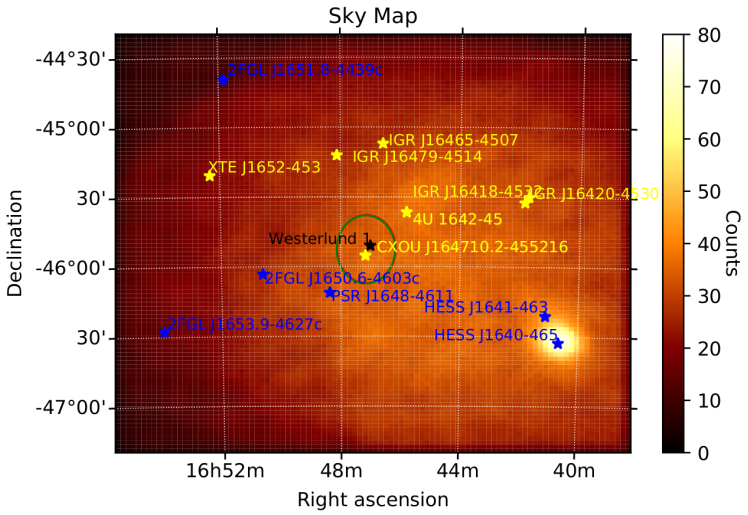

Figure 8: Sky map of the stellar cluster Westerlund 1 carried out by the H.E.S.S. telescope with a large field of view in the energy range of $0.1 - 100$ TeV including *Fermi* (blue stars), H.E.S.S. (blue stars) and *XMM* (yellow stars) sources. The colored ellipses (red: MOS1, green: MOS2, black: PN) indicate the *XMM-Newton* FoV at a pointing position of Westerlund 1

3.3 X-ray Observations

After *Chandra* performed measurements of Westerlund 1 and it was not clear if this X-ray emission is of thermal or non-thermal origin *XMM-Newton* also took a measurement of Westerlund 1 in September 2006 of ~ 48 ks in the energy band $0.3 - 10$ keV (see Figure 9). Kavanagh et al. (2011) extract spectra in the *Chandra* standard hard band $2 - 8$ keV in annuli of $<1', 1 - 2', 2 - 3.5'$ and $3.5 - 5'$. A spectrum of the inner $2'$ is shown in Figure 9 for a combined analyis of the MOS detectors, the PN CCDs were excluded.

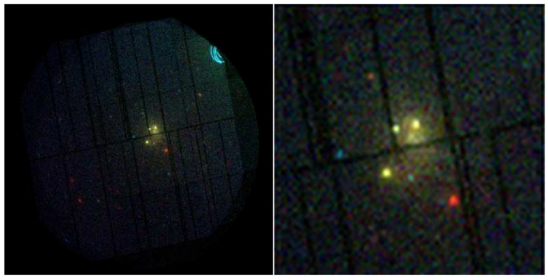

(a) Left: 30′ image of Westerlund 1 observed by *XMM-Newton*. Red, green and blue corresponds to different energy bands ($0.3-2\,\mathrm{keV}$, $2-4.5\,\mathrm{keV}$ and $4.5-10\,\mathrm{keV}$). The stray light in the upper right corner is most likely due to the close by LMXB 4U 1642-45. On the right hand side is a zoomed $5'$ by $5'$ view resolving point sources as well as diffuse X-ray emission (Kavanagh et al., 2011).

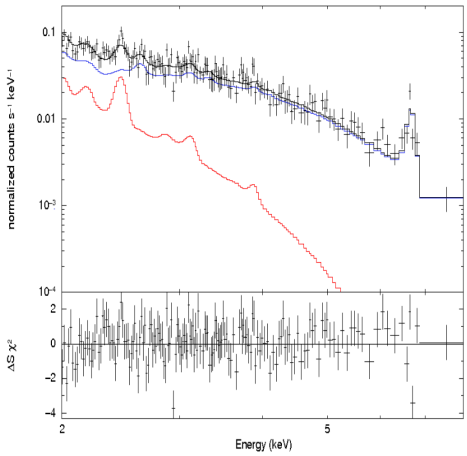

(b) Spectrum of a combined analysis of the MOS detectors fitted with an absorbed two temperature plasma model. The hard and soft thermal components are shown as blue and red lines (Kavanagh et al., 2011).

Figure 9: Image and spectrum of the Westerlund 1 observation from the *XMM-Newton* telescope.

An absorbed two temperature thermal plasma model and absorbed plasma model with an addtional power law component gave similar fit statistics in the inner annuli. This was suprising to the authors because the hard diffuse emission of Wolf-Rayet stars in Westerlund 1 is expected to be thermal due to a thermalized cluster wind. On contrary, in the spectrum of *Chandra*, Kavanagh et al. (2011) were able to measure the He-like Fe 6.7 keV line[16]. This line is used as an indicator for thermal diffuse hard emission.

This leads to the assumption that in the inner $2'$ the hard component is dominantly of thermal origin. Additionally, Kavanagh et al. (2011) applied this analysis to the outer annuli as well but failed to uncover any lines in the hard continuum which still leaves the question of thermal or non-thermal origin of the hard emission. They determined a luminosity of $1.7 \cdot 10^{33}\,\mathrm{erg\ s^{-1}}$ for Westerlund 1. In the end they draw the conclusion that no additional diffuse non-thermal component was found in Westerlund 1 and explained the line to be a feature of the cluster diffuse emission suggesting the origin of the hard emission to be a thermalized cluster wind with a contribution of unresolved pre main sequence stars (Kavanagh et al., 2011).

[16]This emission line originates from an iron atom with just two electrons like helium.

3.4 Gamma Ray Observations

An analysis of Westerlund 1 and the region around it was carried out by the HESS Collaboration (2011) including γ-ray data from the H.E.S.S. Galactic Plane Survey (2004 and 2007) and follow-up observations in 2008 at zenith angles between 21° and 45° and an average pointing offset from the postion of Westerlund 1 of 1.1° (HESS Collaboration, 2011). Due to large γ-ray emission around Westerlund 1 of a size of 1.1° (HESS J1646-458) a classical approach for analyzing the measured data is not easily possible. Therefore, other background estimation techniques have to be applied and HESS Collaboration (2011) made use of a modified version of the classical *On-Off* analysis and a *template* based method.
The *template* background model[17] was applied to generate a sky image and study the overall morphology of Westerlund 1 and the region around it (see Figure 10 (a)) (HESS Collaboration, 2011).
The two bright spots in Figure 10 are considered as two emission regions A (upper spot) and B (lower spot) for investigating a multi-source hypothesis expecting an energy-dependent morphology. Indeed a multi-source hypothesis is preferred over a single Gaussian profile although no energy-dependent morphology is observed. While the image and morphology was determined by the *template* background model the spectrum of the whole emission region (white circle in Figure 10) was obtained by a modified *On-Off* background estimation[18] (HESS Collaboration, 2011). A differential energy spectrum can be found in Figure 10 (b) for the whole 1.1° region as well as for each of the bright spots A and B extracted with the *ring* background method[19].
The HESS Collaboration (2011) determined a VHE γ-ray luminosity of $1.9 \cdot 10^{35}\,\mathrm{erg\ s^{-1}}$ at a distance of 4.3 kpc. In the end they conclude that the emission of the entire 1.1° region as well as the subregions A and B might be explained by a hadronic origion because there are some dense structures seen in HI and CO data. They suggest that also a superposition of sources might lead to the emission observed around Westerlund 1 (HESS Collaboration, 2011).

In 2013, Ohm et al. (2013) published a paper of measurements with the *Fermi* LAT telescope between 3 and 300 GeV. They analyzed ~ 4.5 years of data taken from August 2008 until January 2013 and found an extended emission which overlaps partially with the measured TeV emission of H.E.S.S. A counts map of the *Fermi* data is shown in Figure 11 as colored pixels.

[17] It is created based on image-shape parameters distinguishing signal and background events by specified intervals in the parameter space. Events located in these intervals are characterized either as γ-ray-like (*On* counts) or hadronic events (*Off* counts) (Berge et al., 2007).
[18] The *Off* region here was not extracted in the same FoV but from observations with no γ-ray source in the FoV within four months under similar observation conditions as the *On* data (HESS Collaboration, 2011).
[19] In this model a circle containing the whole γ-ray source will be used as the *On* region whereas the *Off* region is a ring around the *On* region (Berge et al., 2007).

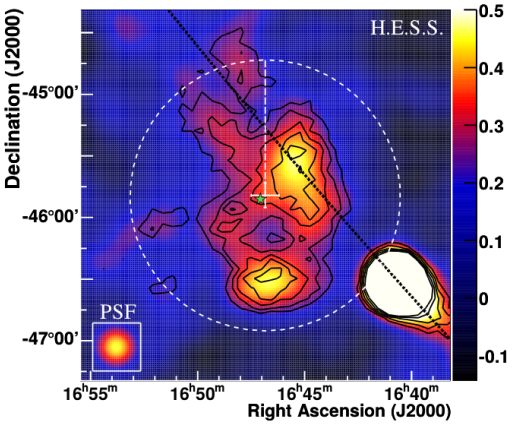

(a) H.E.S.S. excess map of Westerlund 1 and the region around it. The color code shows the nummer of measured γ-ray events per arcmin^2; the contours give significances from 4σ to 8σ. A green star indicates the position of Westerlund 1 whereas the white cross is the best-fit position of the VHE γ-ray emission. Also shown is the 95% containment radius of 1.1° as a white cirlce used for the spectrum and the black dashed line shows the Galacic Plane. The big bright extended region in the lower right corner is HESS J1640-465 (HESS Collaboration, 2011).

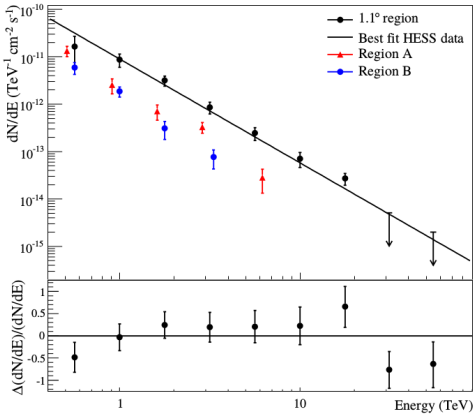

(b) Differential energy spectrum extracted for the whole 1.1° region as well as for each of the bright spots A and B fitted with a power law (HESS Collaboration, 2011).

Figure 10: Illustration of the morphology and spectrum of the Westerlund 1 region.

The determined energy content in γ-ray between $3 - 300\,\mathrm{GeV}$ is $< 1.5 \cdot 10^{34}\,\mathrm{erg\ s^{-1}}$. For explaining the emission in GeV and TeV energies Ohm et al. (2013) suggest proton acceleration in or close by Westerlund 1 by SNe. These could diffuse away and interact with dense material leading to very high energy γ-rays. But for this an energy injection of $\sim 10^{51}\,\mathrm{erg}$ and a slow diffusion of the particles are needed to explain the high and very high energy emission.

3.5 Other Wavelength Bands

Measurements in other wavelengths are needed to trace the dense environment such as (giant) molecular clouds (MC) of Westerlund 1 and the region around it. Observing H_2 directly is almost impossible in cold interstellar regions so that CO is used as a tracer of moluecular gas. Therefore, measurements of Galactic CO (rotational transitions) at 115 GHz have been perfomed over two decades by small millimeter-wave telescopes from Cambridge, Massachusetts and at the Cerro Tololo Interamerican Observatory in Chile (Dame et al., 2001). A CO map of the region around Westerlund 1 reveals dense CO emission (see Figure 12)

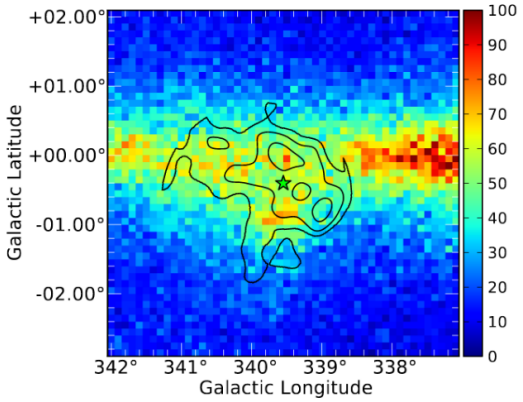

Figure 11: *Fermi* counts map of measurements of Westerlund 1 and the region around it seen as colored pixels. The black contours give the 35%, 55% and 85% peak emission of the smoothed H.E.S.S. excess and the green star gives the Westerlund 1 position (Ohm et al., 2013).

(Ohm et al., 2013).

As HESS J1640-465 and HESS J1641-463 are in the same field of view as Westerlund 1 it is also interessing in other wavelengths to reveal structures. HESS J1640-465 is overlapping with the SNR shell of G338.3+0.0 and HESS J1641-463 is concident with the SNR G338.5+0.1. Measurements of Lau et al. (2016) show that a HII region connects the two SNRs and CO data reveal diffuse molecular gas coincident with HESS J1640-465 and HESS J1641-463 providing target material for high energy CRs (Lau et al., 2016).

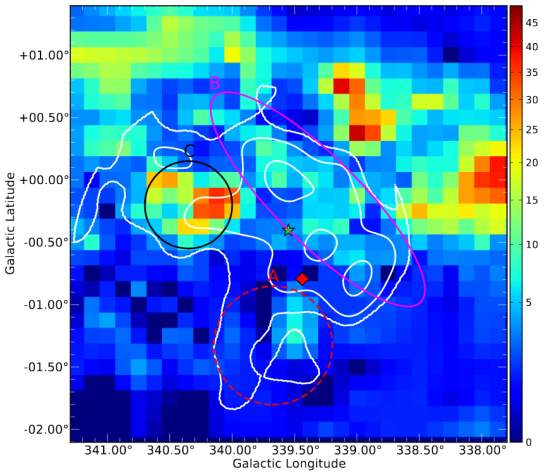

Figure 12: CO map of the region around Westerlund 1. White contours indicate the H.E.S.S. excess, the green star the Westerlund 1 position and the red diamond the pulsar PSR 1648-4611. The circles and the ellipse (denoted as A, B and C) are used for estimation of H_2 and HI density and masses (Ohm et al., 2013).

4 Analysis

In the following analysis data from the H.E.S.S. instrument and the *XMM-Newton* satellite were used. The γ-ray data were analyzed with the open source software package *ctools* which is based on a model template likelihood fitting approach. For the analysis of the X-ray data from *XMM-Newton* ESAS (Extended Source Analysis Software) was used. A description of the tools and the implemented tasks will be given in sections 4.1 and 4.3.

4.1 The *ctools* Way

ctools is an open software package written for the analysis of γ-ray data for the next generation ground-based Imaging Atmospheric Cherenkov Telescope array CTA (Cherenkov Telescope Array). But also analysis of data from other experiments like H.E.S.S. , MAGIC or VERITAS and even space-based experiments like *Fermi* and COMPTEL is supported (Cherenkov Telescope Array Analysis Software Team, 2019). The main motivation using *ctools* is that the γ-ray emission around Westerlund 1 has such a large extent of $\sim 2.2°$ that a selection of source free regions in the field of view of the system which are needed for a proper background estimation is not easily possible. *ctools* does not need source free regions by construction because it is applying a model template likelihood fitting routine so that no particular *Off* region is needed. Also the contamination of sources among each other will be taken into account properly which might be powerful in the analysis of Westerlund 1 because it is located in the crowded Galactic Plane.

As mentioned earlier it is based on a maximum likelihood template fit which means that it takes the field of view model containing a source model and a model describing the background and fits them via a maximul likelihood optimization to the data. The maximum likelihood method estimates the best values for free parameters of a model describing the data set by maximizing the logarithm of the likelihood function L. $\log(L)$ is given as the sum over probability density funtions (pdf) describing probability distributions of the measured variables:

$$\log(L) = \sum_i \mathrm{pdf}(x_i; \Theta),$$

with x_i denoting measured variables and Θ the parameter determining the pdfs (Cowan, 1998). In γ-ray astronomy the propability density function of events are mostly Poisson distributed ($f(n;\nu) = \frac{\nu^n}{n!}e^{-\nu}$, n: interger variable, ν: parameter determining the statistics) due to low photon count rates (Jung, 2016).
In *ctools* actually the negative log-likelihood value will be minimized which is equivalent to a maximization of the positive log-likelihood:

$$-\ln L_i(M) = \sum_k e_{k,i}(M) - n_{k,i} \ln e_{k,i}(M),$$

where the sum is taken over all bins k in a data cube and $n_{k,i}$ the number of measured events in bin k and observation i. $e_{k,i}$ gives the number of predicted events from the model M in the kth bin and ith observation (Knödelseder et al., 2016). The TS value is used to distingush between two hypotheses and represents a measure of the improvement of the model in comparison to the previous model in the following way:

$$\mathrm{TS} = -2 \log \frac{L_1}{L_2}. \tag{4}$$

A measure how much the model improved is the significance σ (Cherenkov Telescope Array Analysis Software Team, 2019) which can be calculated from the TS value via

$$\sigma = \sqrt{\mathrm{TS}} \tag{5}$$

(Ziegler, 2018).
For modelling the data in general several spatial as well as spectral models are available in *ctools*. There exists spatial models for a point source, several models for extended and diffuse sources and composite models. `RadialGaussian (RD)`, `RadialDisk (RD)`, `RadialShell (RS)`, `EllipticalDisk (ED)` and `EllipticalGaussian (EG)` are the models that can be

used for fitting extended sources. The model `RadialGaussian` uses a 2d radially symmetric Gaussian for describing an intensity distribution at a specific position with a width of σ:

$$M_{\mathrm{RG}}(\Theta) = \frac{1}{\sqrt{2\pi\sigma}} \exp\left(-\frac{\Theta^2}{2\sigma^2}\right).$$

A uniform distribution of the intensity will be assumed for the `RadialDisk` model with the spatial parameters (R.A., Dec) and the disk radius. Later on the `EllipticalGaussian` model will be used. It has R.A., Dec, an orientational angle, a minor radius a and a major radius b as parameters:

$$M_{\mathrm{EG}}(\Theta, \phi) = \exp\left(\frac{-\Theta^2}{2r_{\mathrm{eff}}^2}\right),$$

$$r_{\mathrm{eff}} = \frac{ab}{\sqrt{(a\sin(\phi-\phi_0))^2} + \sqrt{(b\cos(\phi-\phi_0))^2}},$$

with ϕ the azimuth angle and ϕ_0 the position angle. The models for diffuse emission were not used in this thesis but composite models were used to try to model the emission correctly. This model takes an arbitrary number of models describing the morphology of different components with the same spectral model.
Spectral models used in this analysis are `PowerLaw (PL)` and `ExponentialCutoffPowerLaw (ECPL)` . The PL is given by

$$\mathrm{PL} = \phi_0 \left(\frac{E}{E_0}\right)^{\gamma},$$

with ϕ_0 being the normalization at E_0, E_0 the pivot energy[20] and γ the spectral photon index, and the ECPL by

$$\mathrm{ECPL} = \phi_0 \left(\frac{E}{E_0}\right)^{\gamma} \exp\left(-\frac{E}{E_C}\right),$$

with the additional parameter E_C indicates the energy at which the cutoff is located (Cherenkov Telescope Array Analysis Software Team, 2019).

[20]The pivot energy gives the point at which the spectrum is tilted and is always fixed to 1 TeV in this analysis.

4.2 Gamma-Rays

For this analysis γ-ray data containing runs with up to 2.0° pointing offset from the Westerlund 1 position at R.A.: 251.7500 ° and Dec: −45.8514 ° are used. In total, 75 h (173 runs) of data including three and four telescope runs between 2004 and 2011 at different zenith angles between 20° and 60° were analyzed. Distributions of the time of data taking, pointing offsets and zenith angles of the data set are shown in Figure 13. About one half of the data where measured at low pointing offsets ($\sim 0.5°$) and the majority of runs are taken under small zenith angles ($20° - 30°$).

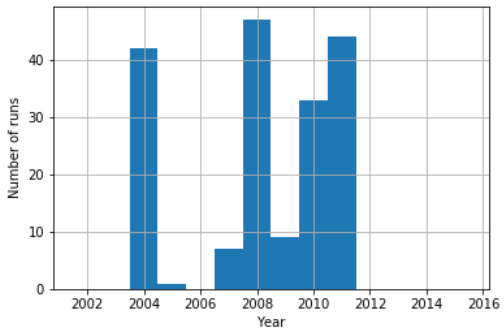

(a) Years in which the used data were taken.

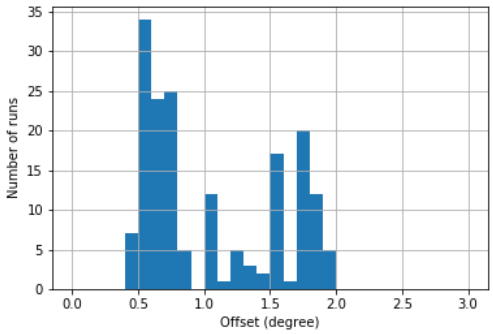

(b) Source to pointing offset.

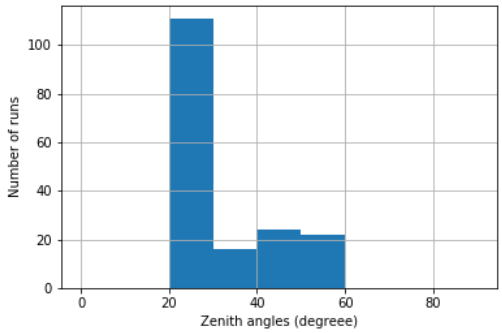

(c) Zenith angles under which the used measurements were performed.

Figure 13: Information about the data set measured by H.E.S.S. used for this analysis.

Each run stors information about the single events, effective area, *point spread function* PSF, energy dispersion and field of view background.

The effective area of the instrument is a function of zenith angle, event offset, energy of the event, selection cuts applied to the data and on the optical efficiency[21] if it's changing dramatically. It is given either as function of simulated γ-ray energy (A*true*) or reconstruced

[21]The optical efficiency gives the ability of the mirror to reflect light and is monitored by measuring muons because the amount of light emitted by them can be very good predicted (Aharonian et al., 2006).

energy (A*reco*); both methods use the assumption of a power law particle distribution with an index of 2.0 and are used for different purposes (Aharonian et al., 2006). How the system can spatially resolve a point source is given by the *point spread funtion* PSF where the value $\frac{\mathrm{d}P}{\mathrm{d}\Omega(r)}$ is stored and describes the propability P to detect an event within a solid angle $\mathrm{d}\Omega$ at a pointing offset r. A measure for describing the ability of the detector reconstructing (E_{reco}) the true energy (E_{true}) based on Monte Carlo[22] simulations provided by look-up tables is the energy dispersion, i. e. E_{reco} as function of E_{true}, $\frac{E_{reco}}{E_{true}}$ (Gamma-ray astronomy community Revision, 2019).

The background is described with a *Field of View* background model developed by Christopher Sobel in 2018. For that he took 5265 h of data (11986 runs) grouped them in zenith angle, azimuth angle and energy with the result of 26 independent backgrounds describing the whole field of view without any known γ-ray source (Sobel, 2018).

The normalization of the background for each observation is set to 1 assuming that every background contributes similary. Figure 14 shows measured events in a $4°$ by $4°$ FoV filled with γ-ray events denoted as counts. To be sure to include all measurements selected the figure illustrates data between $0.1 - 100\,\mathrm{TeV}$ as all following maps if not mentioned differently. Runs might have different energy thresholds calculated from the IRFs[23]. Additionally, a smoothing was applied by convolving data with a tophat 2D kernel[24] to take the PSF of $\sim 0.1°$[25] into account (this is done for all following plots). To keep things simple and speed up the fitting a 3D binned stacked analysis is performed. This means that data are binned in 3-dimensional cubes that are used for the analysis containing all selected observations as a function of right ascension, declination and energy. By creating a counts cube (containing just the counts of the measurement) one is able to investigate the emission in 24 (in this analysis) individual energy slices (see Figure 56 in the appendix) or in energy bands/bins defined as $0.1 - 1\,\mathrm{TeV}$, $1 - 10\,\mathrm{TeV}$ and $10 - 100\,\mathrm{TeV}$ (see Figure 15). These energy bins were choosen to cover one decade per bin. As one recognizes most of the diffuse emission is apparent in the lowest energy band and less in the highest. Also present is that at the edges is less emission than around the middle (shifted a little bit to the right lower corner). This is due to the fact that most measurements were taken towards the right lower corner leading to higher exposures[26] as displayed in Figure 16.

[22] This method is based on a numerical technique for calculations of probablities by using random numbers (Cowan, 1998).

[23] The instrument response is a function of effective area, the PSF and the energy dispersion and describes the response of the detector to an incident photon (Cherenkov Telescope Array Analysis Software Team, 2019).

[24] Convolving a tophat 2D kernel with data has the effect of an isoctopic smoothing within a given radius by taking the value of the central pixel (The Astropy Developers, 2019).

[25] This value describes a 68% containment radius and is in general around $0.1°$ (Aharonian et al., 2006).

[26] The exposure is the effective area multplied by the livetime of the observation (Cherenkov Telescope Array Analysis Software Team, 2019).

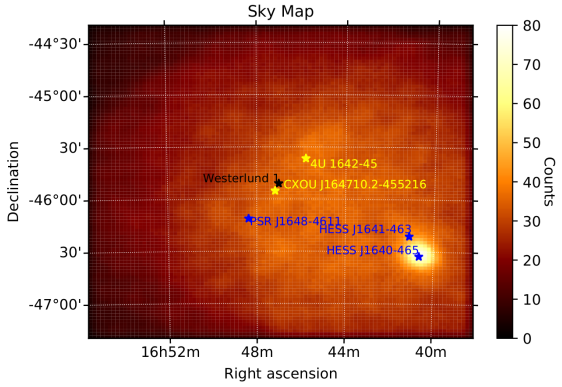

Figure 14: Skymap showing measured γ-ray events from Westerlund 1 (black star) and the region around it including some other known sources within the FoV. Yellow: X-ray sources, blue: γ-ray sources.

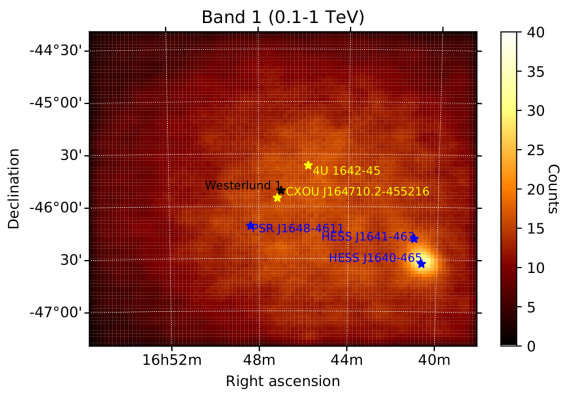

(a) Sky map in the energy band 1 ($0.1 - 1$ TeV).

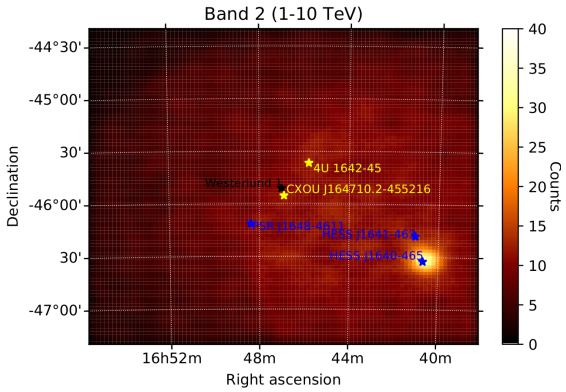

(b) Sky map in the energy band 2 ($1 - 10$ TeV).

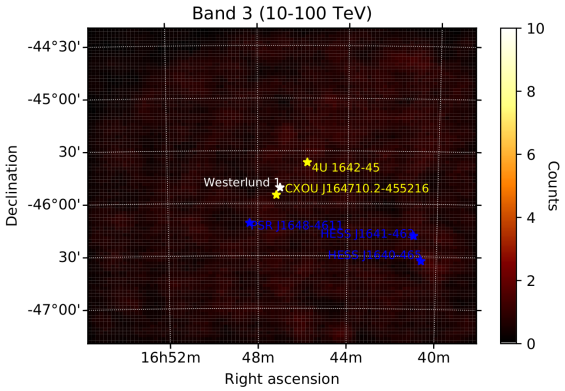

(c) Sky map in the energy band 3 ($1 - 100$ TeV) with an other color scale for a better illustration.

Figure 15: Sky map sliced in different energy bands.

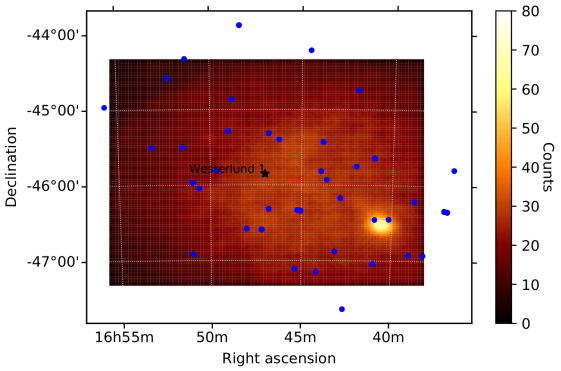

Figure 16: Sky map showing the pointing positions of the measurements.

Similar cubes as the counts cube can be created for the exposure, PSF, energy dispersion and background. If a cube gets stacked which means all counts are integrated over all energy bins a map is created, the sky map for example corresponds to the stacked counts cube. A map of the stacked background cube is displayed in Figure 17.

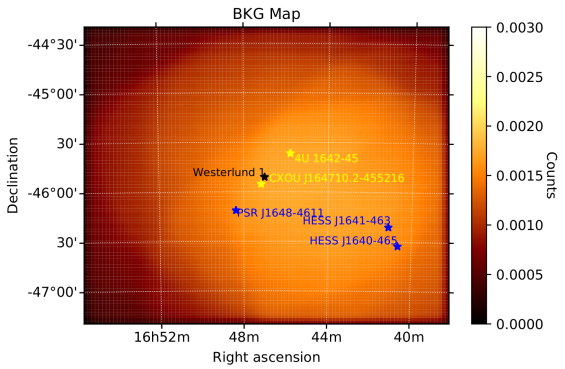

Figure 17: Background map created via stacking of the background cube of the observation. Here, the counts are given per second.

Also here it is visible that most of the background events appear where most of the measurements were taken.

Figure 18 (b) shows the radial profile of a 1.4° region around the Westerlund 1 position in four different sky parts (see Figure 18 (a)) extracted from the counts map. Slice 4 shows clearly the HESS J1640-465 emission at a distance of $\sim 1.35°$ wheras slices 2 and 3 have much lower counts because of the measurements concentrated to the lower right corner as mentioned before. The vertical black line indicates the 95 % containment radius of 1.1° determined by HESS Collaboration (2011). The radial profile is extracted in the way that all counts in each "quarter" ring of each slice are sumed and corrected by the covered ring area, therefore one gets the unit counts/arcmin^2.

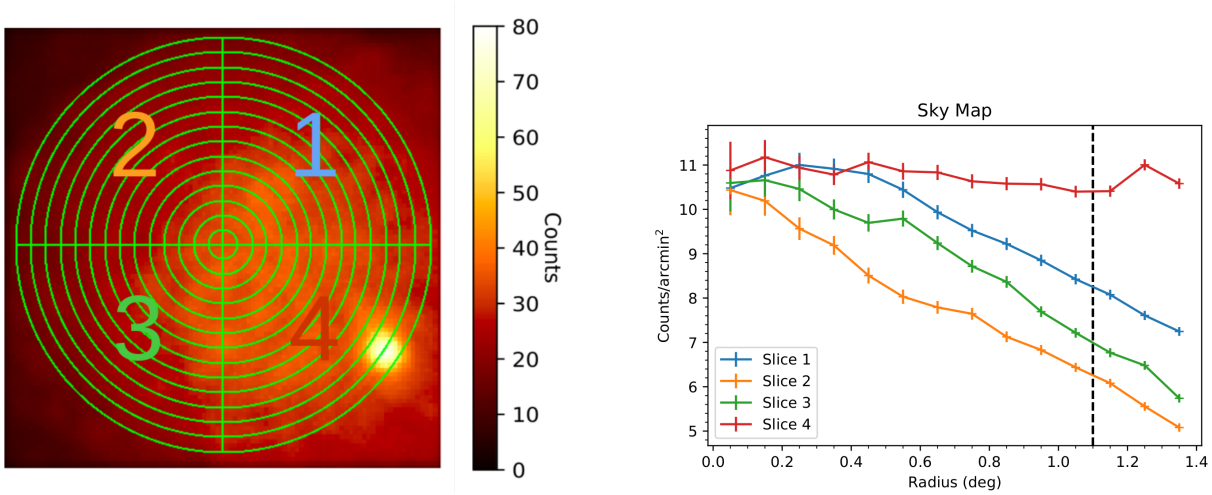

(a) Illustration of the choosen regions for extracting the radial profiles.

(b) Radial profile for the different slices where the emission at $\sim 1.35°$ in slice 4 shows clearly the HESS J1640-465 excess. The black line denotes the 1.1° containment radius of 95 % (HESS Collaboration, 2011).

Figure 18: Region for extracting the radial profile and the radial profiles of the sky map.

4.2.1 Derivation of a Field of View Model

In the following paragraphs a derivation of a model template describing the whole field of view is described. The first step in this analysis is to determine the excess of either diffuse γ-rays or γ-rays from a particular source in the FoV. This is done by fitting a proper background to the data.

If fitting just the background (Model 0) to the data one obtains a fitted background map which will be subtracted from the counts map to get a excess map of the whole field of view (see Figure 19). This procedure is also applied to the following models but not shown explicitly every time. Figure 19 shows a highly significant excess at the position of HESS J1640-465 and HESS J1641-463. There is also diffuse emission above Westerlund 1 in the direction of the right corner and beneath Westerlund 1. Because a stacked analysis is performed the background normalization as well as a spectral tilt is fitted globally to all data simultaneously in each energy bin. The background normalization was fitted to 1.042 ± 0.003 and the relative index (tilt) to 0.037 ± 0.003. The normalization of the background is expected to be 1 which would mean that the predicted background matches the measured one. So when the fitted background normalization is bigger than 1 as it is the case, for Model 0, it means that the predicted background counts are less than the measured ones. The fitted tilt can be interpreted such that there are slightly more background events in the higher energies than in the lower energies predicted as measured.

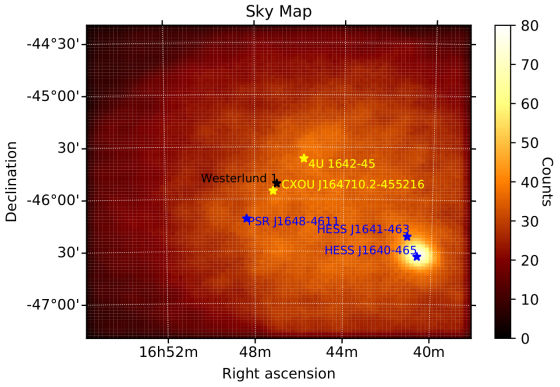

(a) Sky map showing all counts measured.

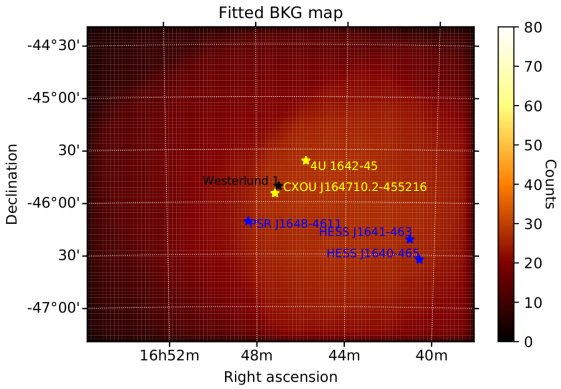

(b) Fitted background model map.

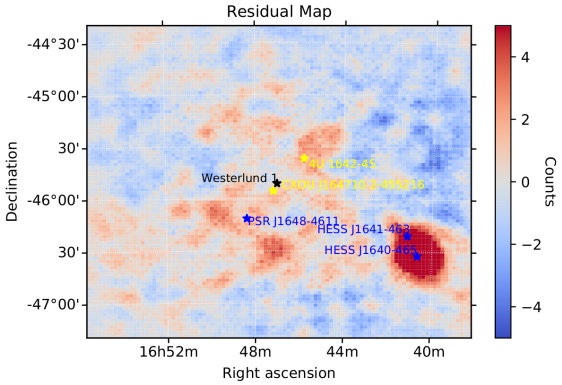

(c) Residual map showing the subtraction of the fitted model map from the sky map.

Figure 19: Sky, fitted background model and residual map.

A determination of the optimized function value $(-\log L)$ gave 65714.353 which will be used for comparison to future models.

In Figure 20 (a) a significance map is given showing the detection significance of the excesses as well as a distribution of the shown significances. The significance of an observation is given by:

$$\sigma = (C_{\text{data}} - C_{\text{model}})\sqrt{2\left(C_{\text{data}}\log\left(\frac{C_{\text{data}}}{C_{\text{model}}}\right) + C_{\text{model}} - C_{\text{data}}\right)},$$

where C_{data} and C_{model} are the measured and predicted counts respectively (Cherenkov Telescope Array Analysis Software Team, 2019). As expected the excess of HESS J1640-465 and HESS J1641-463 is highly significant ($\sigma > 5$)[27] whereas the excess around Westerlund 1 is indicating to an evidence of a detection ($\sigma \approx 4$) in many bins. The distribution of significances after subtracting the background (see Figure 20 (b)) shows a shoulder right of

[27] At the International Cosmic Ray Conference in 1985 it was decided that the significance of a positive detection requires at least 5σ (Degrange and Fontaine, 2016).

the Gaussian distribution. Typically, the Gaussian is centered around zero with a width of 1 representing statistical fluctuations (Aharonian et al., 2006). The shoulder in Figure 20 (b) indicates that there are sources not only statistical fluctuations within the field of view. Here, it has a fitted width of 1.36 way bigger than 1 which indicates systematics arising during the applied procedure.

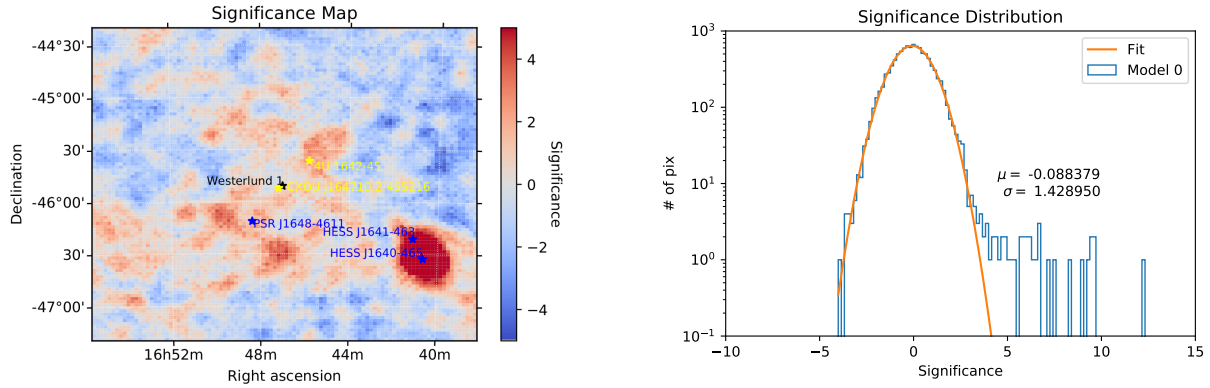

(a) Residual detection significances after fitting of the background.

(b) Significance distribution of after fitting the background to the data.

Figure 20: Significance map and distribution after fitting the background.

A plot of the radial profiles before and after subtraction of the fitted background is shown in Figure 21 (a). The solid lines indicate the excess of the residual map in which the fitted background is subtracted and dashed lines the counts before subtraction. It is clearly visible that the main contribution of the sky map counts were background events and that HESS J1640-465 /HESS J1641-463 still have the highest excess beyond the 1.1° containment region (see Figure 21 (b)).

The next step is to reveal the diffuse emission around Westerlund 1, for that several models were applied to model of the HESS J1640-465 emission and later on also for HESS J1641-463. An extraction of a spectrum will be not carried out for all models described, only for the final model representing the best description of the field of view.

4.2.1.1 Modelling of HESS J1640-465

First, it was tried to model HESS J1640-465 with several different models such as RD and/or RG as spatial models in combination with a power law (PL) or exponential cutoff power law (ECPL) as spectral models. The spatial models were choosen based on profile plots showing counts along a given line illustrated in Figure 22. These kind of profiles were extracted with the help of the DS9 software[28]. The red line is choosen to pass HESS J1640-465 and HESS

[28]DS9 is an application for visualization of astronomical data in FITS format and is also able beyond other things to extract profiles (Joye and Mandel, 2003).

J1641-463. Here, the assumption was that the distribution of events follow either a Gaussian or disk model.

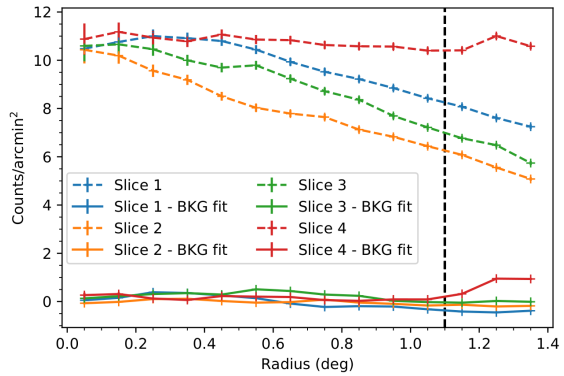

(a) Comparison of the radial profiles between the sky map (dashed) and the residual map (solid) after subtraction of the fitted background. It shows that most of the measured events were background events.

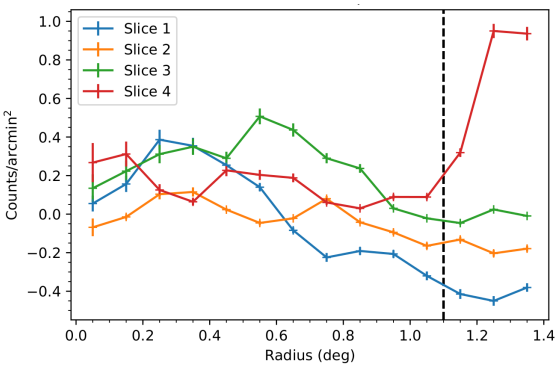

(b) Radial profile after subtraction of the fitted background showing the great excess of HESS J1640-465 /HESS J1641-463 in slice 4.

Figure 21: Radial profiles: (a) comparison before and after the subtraction of the fitted background and (b) a zoomed view showing just the residual excess of Model 0.

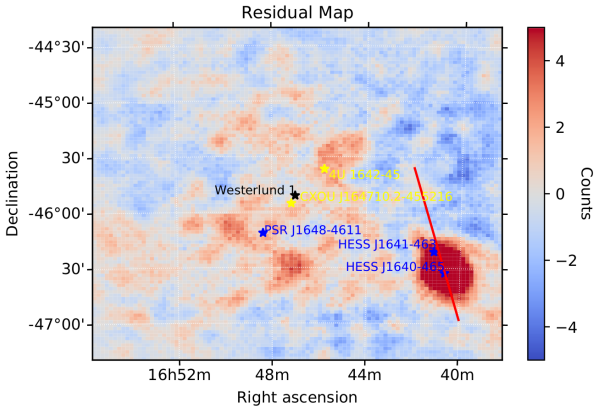

(a) Residual map of the subtracted background fit with a red line along which the profile was extracted.

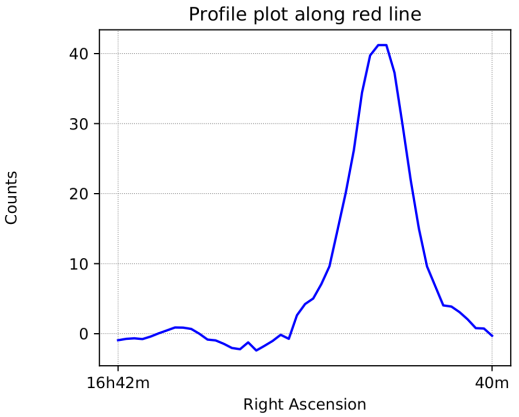

(b) Profile plot extraced along the red line.

Figure 22: Residual map (a) showing the red line along which the profile plot (b) was extracted.

The start parameters for the spatial extension were first guessed and for the spectral parameters either taken from Xin et al. (2018) or the HESS Collaboration (2014b). The best model (Model I) converging and not running into parameter limits was the one with start parameters as given in Table 1 from HESS Collaboration (2014b), the position taken from the *TeVCat*[29] with the usage of a `RadialGaussian` as spatial model and ECPL as spectral

[29]The *TeVCat* is an online catalog of high energy sources (TeV) provided by Scott Wakely and Deirdre Horan Wakely and Horan (2019).

model.

Model	Component	Start	Fit
I	R.A. (°)	250.175	250.165 ± 0.004
	Dec (°)	-46.5457	-46.541 ± 0.003
	σ (°)	0.49	0.049 ± 0.003
	ϕ_0 ($\mathrm{cm^{-2}s^{-1}TeV^{-1}}$)	$3.3 \cdot 10^{-12}$	$5.542 \cdot 10^{-12} \pm 3.831 \cdot 10^{-13}$
	γ	-2.11	-1.442 ± 0.109
	E_C (TeV)	6.0	2.593 ± 0.347

Table 1: Start and fitted parameters for HESS J1640-465.

A residual map showing the fitted model map subtracted from the sky map can be found in Figure 23 as well as the belonging radial profile plot compared to Model 0. Again the solid lines indicate the newest model here Model I and the dashed the model in which only the fitted background is subtracted from the sky map. One recognizes that the excess counts in slice 4 around 1.35° are gone. Also apparent is that there is in general more counts in the slices as the background normalization was fitted a little bit lower ($\phi_0 = 1.029 \pm 2.413 \cdot 10^{-3}$, $\gamma = 0.036 \pm 2.482 \cdot 10^{-3}$) compared to Model 0. Already visible are the excesses around Westerlund 1, also there are still some positive residuals left below HESS J1640-465 and also excess around the position of HESS J1641-463. Figure 23 shows also a profile plot extracted along the red line (as given in Figure 22) with much less counts for Model I in comparison to Model 0. But there is still some enhanced emission left which might corresponds to HESS J1641-463. The fit of Model I gave an optimized function value $-\log L$ of 64761.511 when calculating the TS value via Equation 4 one gets 1905.684 and out of that one is able to determine a significance $\sigma = 43.66$ (see Equation 5). This means that the inclusion of HESS J1640-465 in the model significantly improved the description of the FoV.

4.2.1.2 Modelling of HESS J1641-463

Further modelling is based on an iterative procedure. This method is applied for the next models for describing the enhanced emission regions around Westerlund 1. As in Figure 23 (a) recognizable there is still some emission left above HESS J1640-465 , around the position of HESS J1641-463 as mentioned in the paragraph before. So the fit values of Model I were used as start parameters for the next input model. First, a RD for modelling HESS J1641-463 was used also some composite models were tried but in the end Model II has an additional RG with a PL spectrum as input. The start parameters for the additional components were obtained from HESS Collaboration (2014a). A residual map of Model II is shown in Figure 24 with an additional profile plot again extracted along the red line for Model II and Model I.

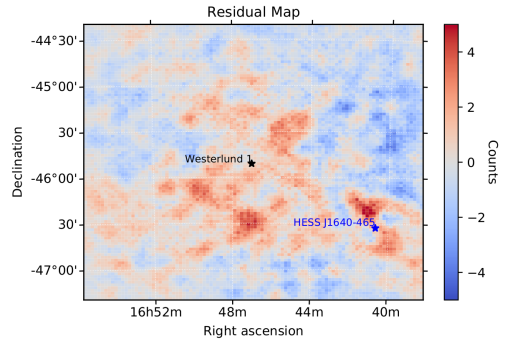

(a) Residual map of Model I showing that a lot emission at the postion of HESS J1640-465 is gone.

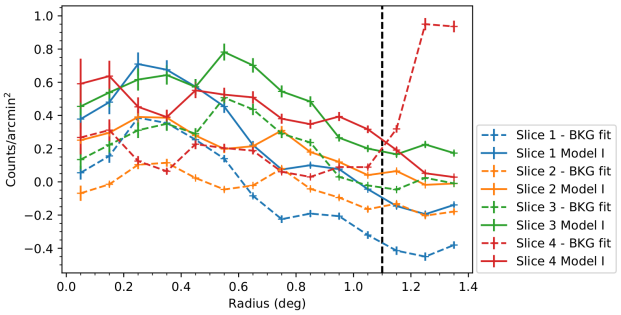

(b) Radial profile plot illustrated in comparision with the subtraction of the background only. The emission in slice 4 is gone.

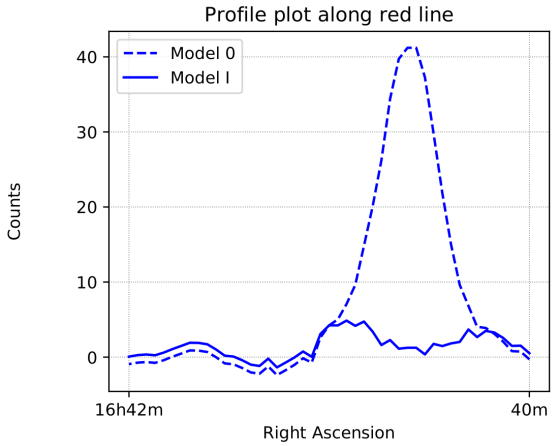

(c) Profile plot extraced along the red line showing that most of the emission is gone (solid line) but some enhanced emission is still apparent.

Figure 23: Residual map (a) of the applied Model I and the corresponding radial profile plot (b). (c) shows the profile plot extracted again along the red line.

There is still a concentration of small positive residuals in the region around HESS J1640-465 and HESS J1641-463 but it is way less than before in Model I. Also given are the radial profile plots comparing Model I and II with a slight change at 1.15°. Table 2 shows the start and fitted parameters in comparison. As the fitted parameters for HESS J1640-465 and the background of Model II didn't change that much they are not printed in this table but can be found in the appendix in Table 17. Since the optimized function value of Model II is 64748.071, it improved significantly with 5.18σ compared to Model I. The remaining excess seen in Figure 24 (a), except around HESS J1640-465 and HESS J1641-463, is the Westerlund 1 excess. Further attempts of getting rid of the posivite residuals around HESS J1640-465 and HESS J1641-463 unfortunately failed. It was tried to add radial Gaussians left of HESS J1641-463, between HESS J1640-465 and HESS J1641-463, at the lower right of HESS J1640-465 or combinations of those with different spatial models (RD and/or RG). These fits either ran in limits or even stalled.

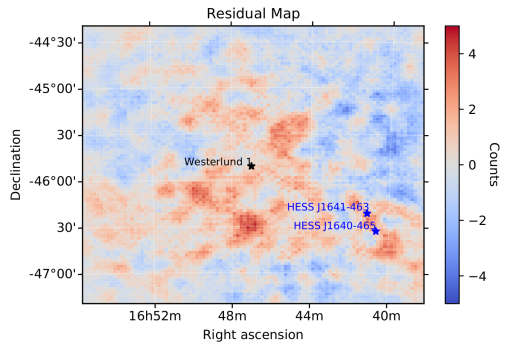

(a) Residual map of Model II.

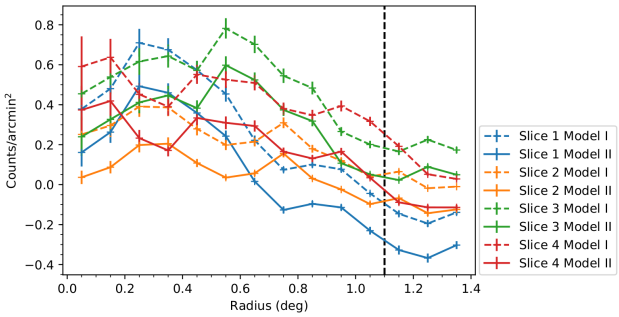

(b) Radial profile plots comparing Model I and II.

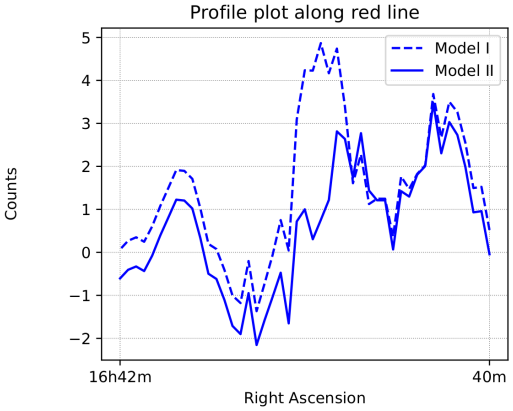

(c) Profile plot extracted along the red line. The big peak at the position of HESS J1641-463 is way less than before.

Figure 24: Residual map of Model II (a) and the corresponding profile plot a long the red line (b) shown before. Additionally, profile plots of Model II and I are given in which the emission at the HESS J1641-463 position is less then before.

Model	Component	Start	Fit
II	R.A. (°)	250.2583	250.279 ± 0.023
	Dec (°)	-46.3036	-46.353 ± 0.017
	σ (°)	0.09	0.036 ± 0.015
	ϕ_0 ($\mathrm{cm^{-2}s^{-1}TeV^{-1}}$)	$3.91 \cdot 10^{-13}$	$2.654 \cdot 10^{-13} \pm 8.709 \cdot 10^{-14}$
	γ	-2.07	-2.071 ± 0.163

Table 2: Start and fitted parameters compared for Model II.

4.2.1.3 Modelling of the excess around Westerlund 1

As HESS J1640-465 and HESS J1641-463 were modeled sucessfully up to concentrated positive residuals around them the excess around Westerlund 1 was next. Therefore, the labelling of HESS Collaboration (2011) was followed: the upper right excess is called A, the one below to the right of the Westerlund 1 position B and the other one C (see Figure 25). Also profile plots extracted along lines from C to B, C to A and B to A are generated and

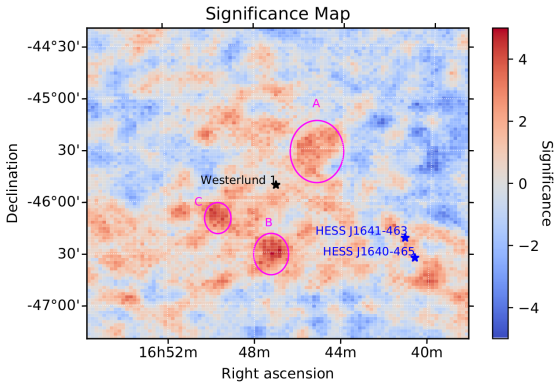

Figure 25: Residual map of Model II with the labeled regions A, B and C.

displayed in Figure 26 for a quantitive analysis how the models improve. First, it was tried to model A with a RG and a PL model but the fit didn't converge even with partly fixing some components. So it was decided to start modelling the emission region B and add A later on. Furthermore, this degree-scale diffuse γ-ray emission is also referred as HESS J1646-458 or in this thesis also just 1646.

Modelling of Region B An additional `RadialGaussian` with a Pl was included in the model. The positional start parameters were estimated, the extension taken from HESS Collaboration (2011), whereas for the spectral values a power law index of 2.0 and a normalization of $3.0 \cdot 10^{-18} \frac{\text{ph}}{\text{cm}^2\,\text{s}\,\text{MeV}}$ was used. As the first attempt resulted in a wrongly fitted position of 0.36° offset of region B the position was fixed in a second approach. A comparision of the residual maps of the two approaches can be found in Figure 27.

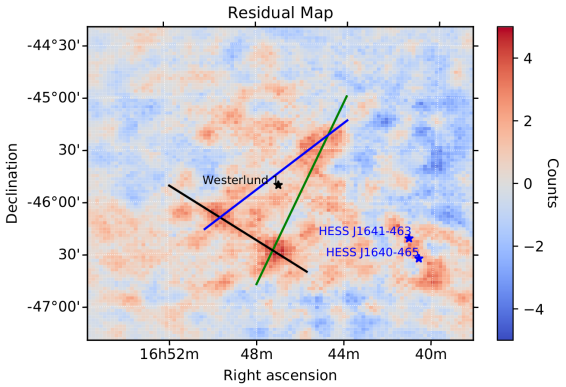

(a) Residual map of Model II showing the lines along which the profiles were extracted.

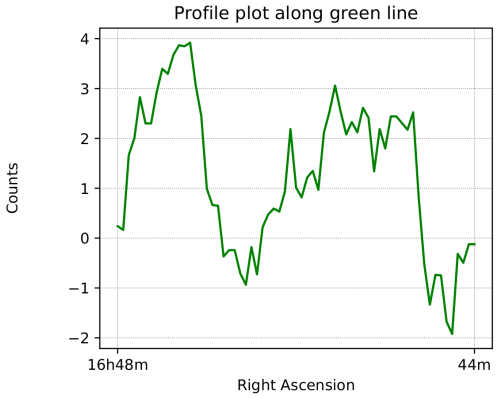

(b) Profile extracted along the green line.

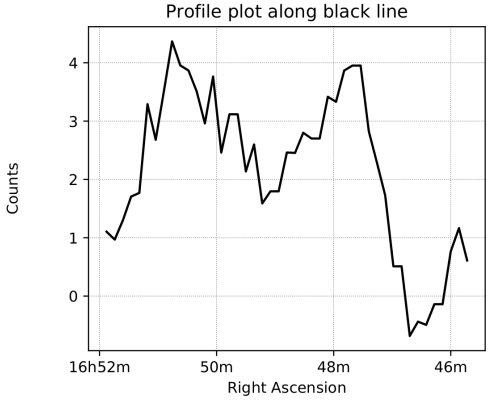

(c) Profile extracted along the black line.

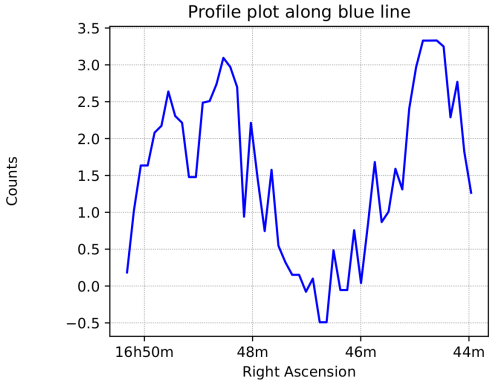

(d) Profile extracted along the blue line.

Figure 26: Residual map of Model II showing a green (B to A), black (C to B) and blue (C to A) line (a) along which the profiles in (b), (c) and (d) are extracted.

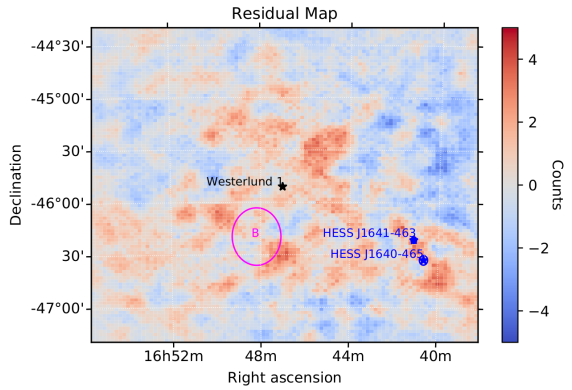

(a) Residual map with all model defining parameters free.

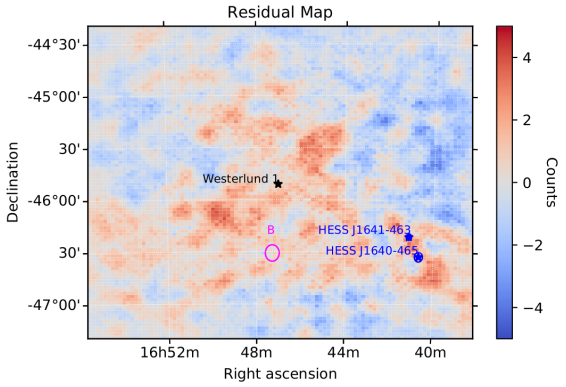

(b) Residual map with a fixed position of B.

Figure 27: Residual maps of the different approaches.

The fitted values as well as the start parameters for both attempts to describe the emission region B can be found in Table 3. In the mentioned table only values for emission region B are given as the other ones for the background, HESS J1640-465 and HESS J1641-463 didn't vary that much but can be found in Table 18 in the appendix.

Model	Component	Start	Fit
IIIa	R.A.$_{\text{free}}$ (°)	251.819	252.044 ± 0.102
	Dec$_{\text{free}}$ (°)	-46.513	-46.328 ± 0.017
	σ_{free} (°)	0.25	0.274 ± 0.056
	$\phi_{0,\text{free}}$ (cm^{-2}s^{-1}TeV^{-1})	$3.0 \cdot 10^{-12}$	$1.222 \cdot 10^{-12} \pm 3.697 \cdot 10^{-13}$
	γ_{free}	-2.0	-2.053 ± 0.134
IIIb	R.A.$_{\text{fix B}}$ (°)	251.819	-
	Dec$_{\text{fix B}}$ (°)	-46.513	-
	$\sigma_{\text{fix B}}$ (°)	0.25	0.079 ± 0.021
	$\phi_{0,\text{fix B}}$ (cm^{-2}s^{-1}TeV^{-1})	$3.0 \cdot 10^{-12}$	$4.674 \cdot 10^{-13} \pm 1.223 \cdot 10^{-14}$
	$\gamma_{\text{fix B}}$	-2.0	-2.252 ± 0.178

Table 3: Start and fitted paramters for the modelling of emission region B with all parameters free (Model IIIa) and a fixed postion of B (Model IIIb).

Figure 28 shows the profile plots extracted along the green and black line as given in Figure 26 for Model IIIb (fixed position of B) and Model II in comparison. The profile along the blue line is not given since there is almost no difference (see Figure 57 in the appendix). It can be seen that most of the emission at the postion of B is gone as expected.

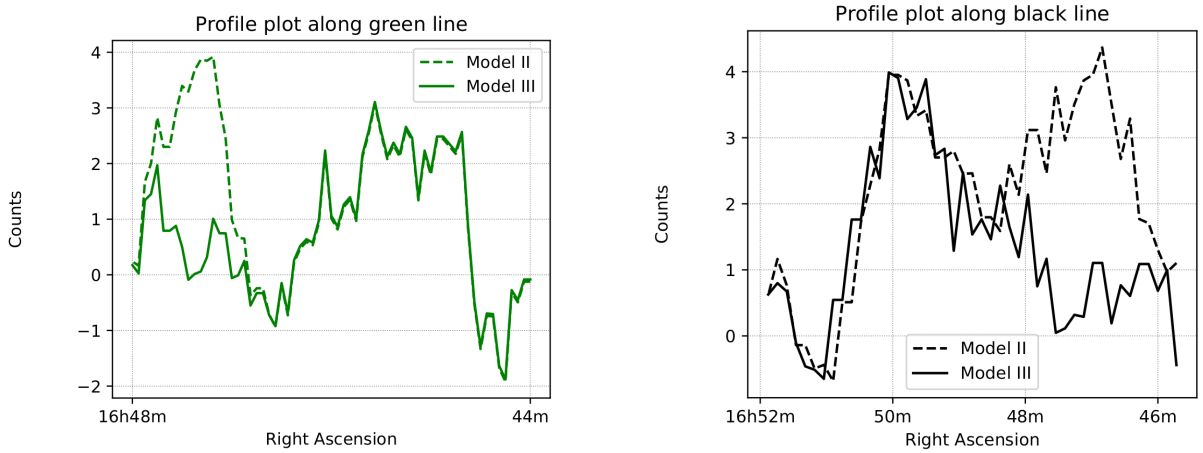

(a) Profile plot extracted along the green line.

(b) Profile plot extracted along the black line.

Figure 28: Profile plots along the green and black line given before for Model III with fixed position of B and II.

Since the TS value of the model with the fixed position was a little bit better ($TS_{free} = 64733.659$, $TS_{fix\ B} = 64732.877$) it was decided to continue with this model as input for the next one by trying to let the position of B free again in the next iteration step. With $TS_{fix\ B}$ a significant improvment with respect to the last model, Model II, of 5.51σ can be determined.

Modelling of Region C Model IIIb was used as a basis for the input model for fitting the emission region C. The spatial start parameters are guessed and for the spectral ones $2.0 \cdot 10^{-18}\ \frac{\mathrm{ph}}{\mathrm{cm^2\,s\,MeV}}$ for the spectrum and 2.0 for the index were choosen.
Start and fitted parameters are given in Table 4 .

Model	Component	Start	Fit
IV	$\mathrm{R.A._C}$ (°)	252.443	252.413 ± 0.063
	$\mathrm{Dec_C}$ (°)	−46.155	-46.167 ± 0.044
	σ_C (°)	0.2	0.129 ± 0.035
	$\phi_{0,\mathrm{C}}$ ($\mathrm{cm^{-2}s^{-1}TeV^{-1}}$)	$2.0 \cdot 10^{-12}$	$5.448 \cdot 10^{-13} \pm 1.871 \cdot 10^{-13}$
	γ_C	−2.0	-2.137 ± 0.193
	$\mathrm{R.A._B}$ (°)	251.819	251.805 ± 0.063
	$\mathrm{Dec_B}$ (°)	−46.513	-46.519 ± 0.025
	σ_B (°)	0.079	0.076 ± 0.021
	$\phi_{0,\mathrm{B}}$ ($\mathrm{cm^{-2}s^{-1}TeV^{-1}}$)	$4.673 \cdot 10^{-13}$	$4.411 \cdot 10^{-13} \pm 1.19 \cdot 10^{-13}$
	γ_B	−2.252	-2.183 ± 0.169

Table 4: Start and fitted parameters for including the emission region C in the model (Model IV) as well as for the emission region B with free positional parameters.

In this model, Model IV, the position of B was free and those parameters among others are also given in Table 4. Also noticeable is that the spectra parameters of the emission regions

B and C seem to be similar within the statistical fluctuations. As usal the parameters for the other sources (background, HESS J1640-465 and HESS J1641-463) didn't change that much (see Table 19 in the appendix).
A residual map can be found in Figure 29 (a) which looks up to now satisfying as the bright emission regions B and C are basiaclly gone except for small concentrated positive residuals. For a quantitative illustration the corresponding profile plots along the black and blue line (see Figure 26) are given in Figure 29 (b) and (c). There is no profile plot shown here for the green line because as before there weren't much changes (see Figure 58 in the appendix).

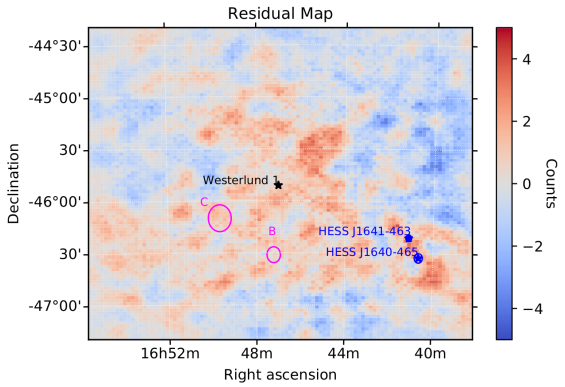

(a) Residual map of a model including emission region C (Model IV).

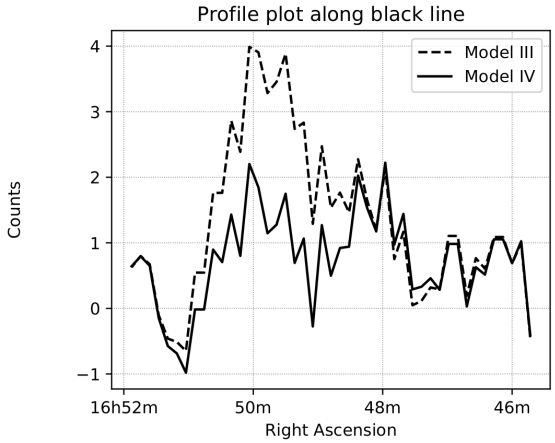

(b) Profile plot extracted along the black line.

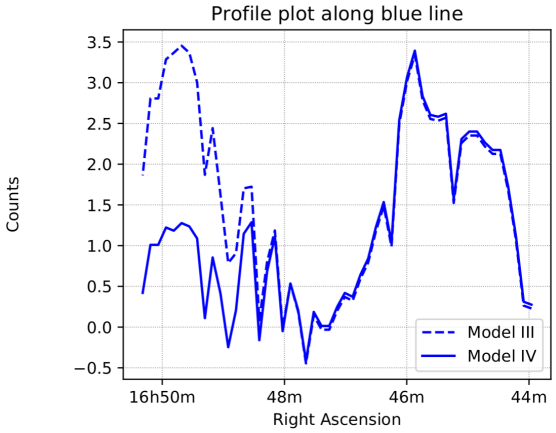

(c) Profile plot extracted along the blue line.

Figure 29: Residual map for Model IV and the corresponding profile plots in comparison of Model IIIb

Unfortnuately, the improvement from Model IIIb to IV was not that much as the ones before with $\sigma = 4.73$ calculated from the $-\log L$ values of the fits.

Modelling of Region A Because just adding the emission region A with an `RadialGaussian` and a PL was not successful another approach for modelling this region had to be found. There were several attempts getting the fit converging without running into limits in which

the emission region positioned correctly, including, the spatial model being a `RadialDisk` and an `EllipticalGaussian` and/or with fixing positions either of A, B or C. The model, further referred as Model V, in which A, B and C have almost the same start parameters converged resonable. In this model a PL as spectral model for each emission region was used and as spatial models: a RG for B and C and a RD for A. But unfortunately the position of A was wrongly fitted as it was free (see Figure 30 (a)) and therefore the position was fixed again (see Figure 30 (b)). The resulting residual map is shown in Figure 30 (a) with the corresponding profile plots extracted along the blue and green line in comparison to Model IV, the profile plot extracted along the black line can be again found in the appendix (see Figure 59).

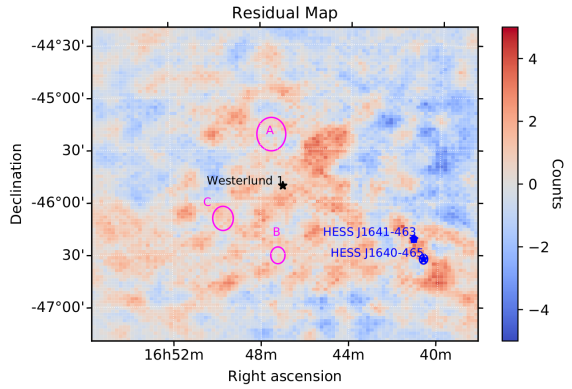

(a) Residual map of Model Va for all parameters set free.

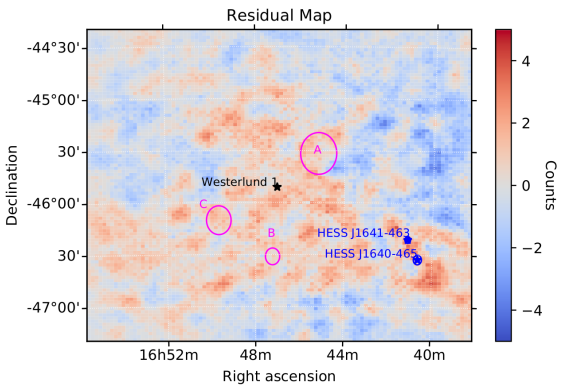

(b) Residual map of Model Vb for a fixed position of A.

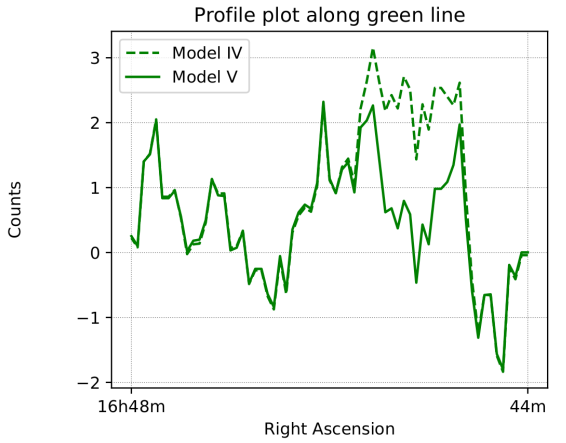

(c) Profile extracted along the green line for Model Vb.

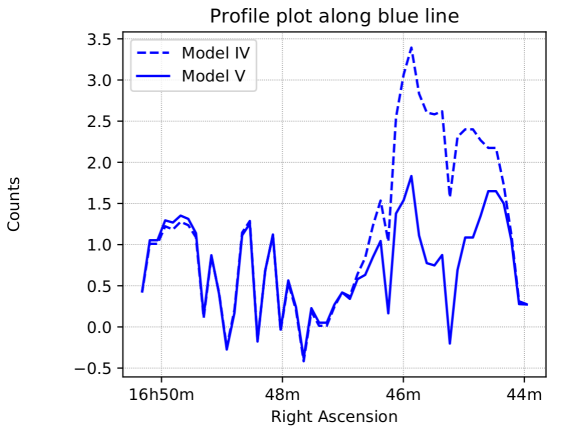

(d) Profile extracted along the blue line for Model Vb.

Figure 30: Residual map of Model V for a free (a) and fixed (b) postion of A and profile plots extracted along the green (c) and blue (d) line shown in Figure 26 (b).

The residual map in Figure 30 (a) shows that the emission regions A, B and C could be described in the way that there is in general less emission. But there are still some

concentrated positive residuals around Westerlund 1. The fitted values for both approaches are given in Table 5 for the emission region A only as the parameters for the background, HESS J1640-465, HESS J1641-463, B and C didn't change that much. These are given for the final model Model Vb in the appendix (see Table 20).

Model	Component	Start	Fit
Va	$\text{R.A.}_{\text{free}}$ (°)	251.290	251.879 ± 0.075
	Dec_{free} (°)	-45.528	-45.359 ± 0.052
	$\text{Radius}_{\text{free}}$ (°)	0.35	0.16 ± 0.053
	$\phi_{0,\text{free}}$ ($\text{cm}^{-2}\text{s}^{-1}\text{TeV}^{-1}$)	$2.0 \cdot 10^{-13}$	$2.032 \cdot 10^{-13} \pm 1.1 \cdot 10^{-13}$
	γ_{free}	-2.0	-2.055 ± 0.305
Vb	R.A._{fix} (°)	251.290	-
	Dec_{fix} (°)	-45.528	-
	$\text{Radius}_{\text{fix}}$ (°)	0.35	0.201 ± 0.033
	$\phi_{0,\text{fix}}$ ($\text{cm}^{-2}\text{s}^{-1}\text{TeV}^{-1}$)	$2.0 \cdot 10^{-13}$	$3.536 \cdot 10^{-13} \pm 1.19 \cdot 10^{-13}$
	γ_{fix}	-2.0	-1.999 ± 0.176

Table 5: Start and fitted parameters for including the emission region A in the model (Model Va) with a free position as well as for fixed positional parameters (Model Vb).

As this model (Model Vb) is declared as the final model a comparision of Model 0 and Model Vb can be found in the appendix in Figure 60 to see how good the describtion of the FoV really is.

For investigating the residual map in more detail it is sliced into three energy bands ($0.1-1$ TeV, $1-10$ TeV, $10-100$ TeV), the slices are given in Figure 31. Recognizable is that most of the residual emission is the lowest energy band ranging form $0.1-1$ TeV because in this energy bin there is the most statistics. Especially in the first energy bin between HESS J1640-465 and HESS J1641-463 there is a bright positive residual left, also in the lower left corner there are some exteneded diffuse residuals which get compensated when stacked because in the other energy bands there is a little bit less emission in this region.

Figure 32 illustrates a significance map of Model Vb showing that there are no significant sources within the field of view. Additionally given is a comparison between the significance distributions from Model 0 and Model V. This is another more quantitive prove that there is no significant source anymore because the shoulder right to the Gaussian disappeared.

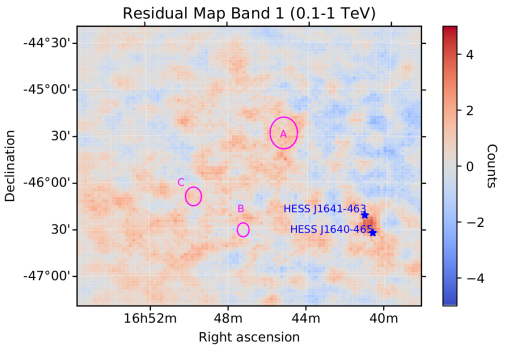

(a) Residual map in the energy bin 0.1 – 1 TeV.

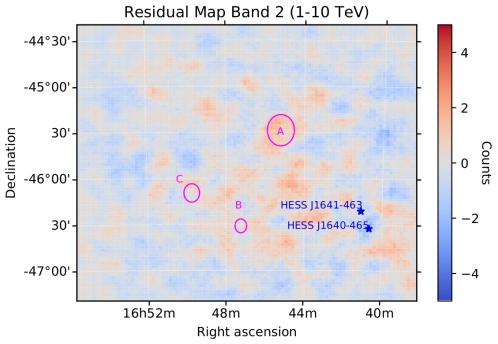

(b) Residual map in the energy bin 1 – 10 TeV.

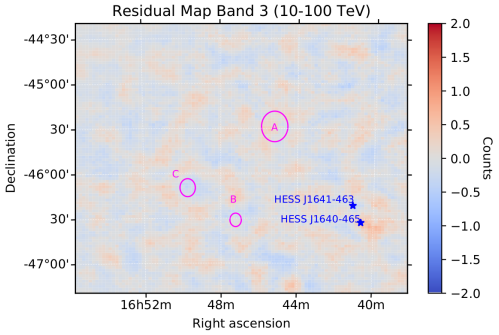

(c) Residual map in the energy bin 10 – 100 TeV.

Figure 31: Residual map slices in three different energy bands for Model Vb.

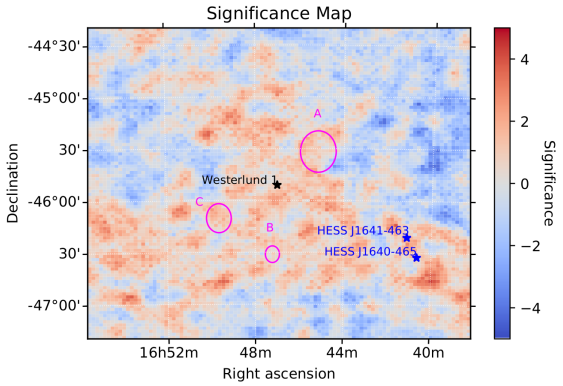

(a) Significance map of the final model Vb.

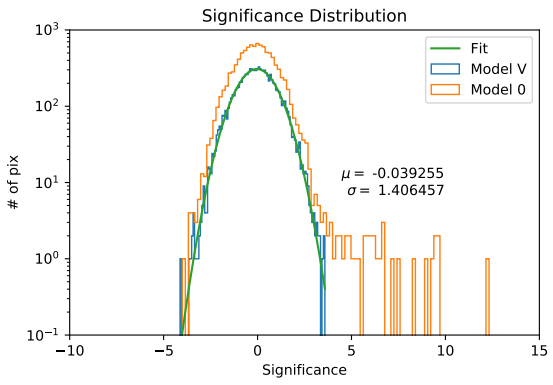

(b) Significance distribution shown for Model 0 and Model Vb.

Figure 32: Significance map (a) and distribution (b) shown for the final model.

For the final model Model Vb the given TS value is 64711.901 (Model Va: 64718.168s) corresponding to an improvement with respect to the former model (Model IV) of 4.43σ. Additionally, the single significances (in comparison as there would be no source) of the emission regions A, B and C are given as $\sigma_{\mathrm{A}} = 4.43, \sigma_{\mathrm{B}} = 5.69, \sigma_{\mathrm{C}} = 4.84$ indicating that

only B is a significant source. Comparing this model (Model Vb) with the one were only the background was subtracted one finds a significance of 44.8.
Also created was a composite model describing the emission regions A, B and C with a single spectrum. This is motivated by the fact that the spectral parameters of these are in agreement within the statistical errors. As usal the output of Model Vb was used as the input for the composite model, but the normalization and index of source B for describing the common spectrum was taken. Here, also a residual map, profile plots and radial profile plots were created and can be found in Figure 33 in comparison with Model Vb in which all the sources have individual spectra. The fitted spectrum of the composite model has a normalization of $1.245 \cdot 10^{-1} \pm 0.217 \cdot 10^{-18} \frac{\text{ph}}{\text{cm}^2\,\text{s}\,\text{MeV}}$and a spectral index of 2.130 ± 0.105. Additionally, all the other fitted values for Model VI can be found in the appendix. It seems that there is no or small differences between Model Vb and Model VI to quantifiy this Figure 34 is created. There is indeed a difference between Model Vb and Model VI as seen in Figure 34 mostly visible around the position of A and a little bit around emission region C. Whereas, emission region A is experiencing a bigger fitted normalization for Model Vb then for Model VI (Model VI is subtracted from Model Vb). Also one has to keep in mind that the position of A were free parameters in this approach. The optimized function value of Model VI is 64712.050 resulting in an improvement compared to Model IV of 4.39, not as high as for Model Vb. Moreover, the significance of the composite model in comparision as there won't be one can be given with 8.46σ. In the following table (Table 6) a summary of all applied models is given regarding the included sources and significances to each other and referred to Model 0 (σ_0). Here, abbreviations for HESS J1640-465 (1640) and HESS J1641-463 (1641) as well as for the composite model (1646) were introduced. The column 'Add. sources' gives the sources that are added for this particular model which means that the former sources are also included. One exception is for Model VI (composite, 1646) only the background, HESS J1640-465 and HESS J1641-463 are additionally included.

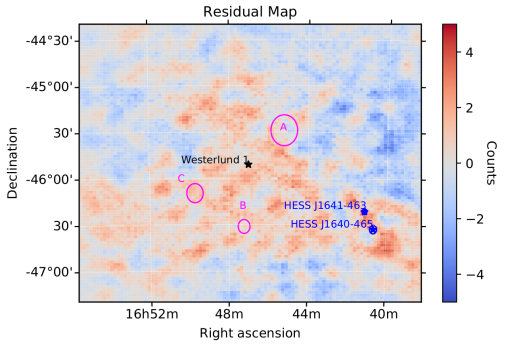

(a) Residual map of Model VI in which HESS J1640-465, HESS J1641-463 were modelled with A, B and C having the same spectrum.

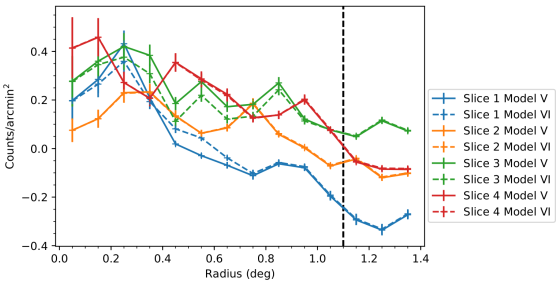

(b) Radial profile plots for Model VI in comparison to Model Vb.

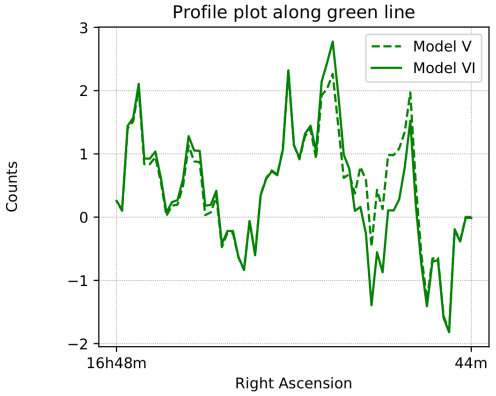

(c) Profile extracted along the green line for Model VI in comparison to Model Vb.

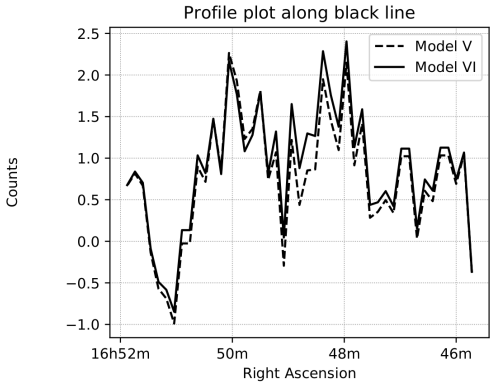

(d) Profile extracted along the black line for Model VI in comparision to Model Vb.

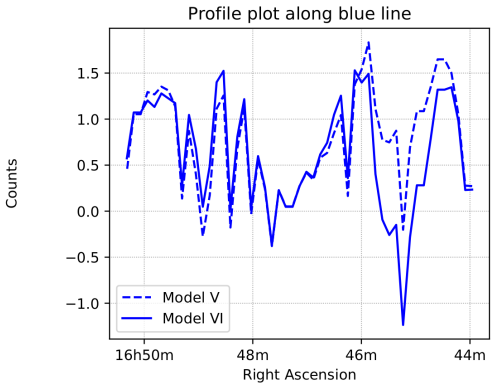

(e) Profile extracted along the blue line for Model VI in comparision to Model Vb.

Figure 33: Residual map, profile and radial profile plots of the composite model in comparison to Model Vb.

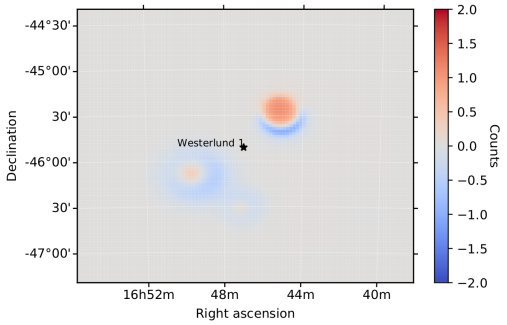

Figure 34: Map of the differences between Model Vb and VI there is only a little difference visible around the emission regions A and C.

Model	Incl. source	$-\log L$	σ	σ_0
0	BKG	65714.535	-	-
I	1640	64761.511	43.66	43.66
II	1641	64748.071	5.18	43.97
IIIb	B (fix)	64732.877	5.51	44.31
IV	C (B free)	64721.701	4.73	44.56
Vb	A (fix)	64711.901	4.43	44.78
VI	1646 (A free)	64712.050	-	44.77

Table 6: Comparison between all models to each other and to Model 0.

When calculating the TS value of Model Vb to VI it can be observed that it is negative which means that the the composite description of the emission regions is worse than consider them with own spectra and so no significance can be calculated.
Overall it can be concluded that both models, Model Vb and Model VI, describe the FoV of Westerlund 1 quite good as all obvious emission regions are modeled but leaving still some concentrated posivite residuals. The improvement of Model VI with respect to model Model IV is maybe not at a 5σ level but high (4.39σ).

4.2.2 Spectral Analysis of Model Vb and VI

The number of energy bins for the extraction of spectra was lowered from 8 to 4 bin per decade to get more statistics within one single bin. Whereas, the spectral flux points are determined in the way that all model components will be fixed except for the normalization of the source of interest and then the flux normalization is computed via re-fitting the model in each energy bin. In addition, the TS value for each spectral point will be calculated. Spectra for the individual sources of Model Vb can be found in Figure 35. Here, so-called butterfly diagrams show the best fit spectrum indicated as a black line as well as the 68% confidence interval of all spectral models in green. It should be noted that the spectral flux is

multiplied by E^2 to reveal spectral features especially for the spectra of the emission regions A, B and C because they have almost the same spectral index. So a horizontal line in this loglog-spectrum refers to a spectrum with an index of 2, if the index is higher or lower 2 it is visible as a slight tilt.

The majority of all spectral points from each source are upper limits of a confidence interval of 95%, these are used if the TS value of a particular flux point is smaller than 4.0 or $\sigma \leq 2$. Additionally, it can be seen that the second point in each spectrum (except for HESS J1640-465) is an upper limit located beneath the best fit spectrum and even located outside the confidence interval. This feature is not understood in detail and appears in 90% of all limits. That seems to be unphysical because an upper limit should be located above the best fit not below. The fitted parameters of the spectra can be found in the tables of the models described above. In general, the assumed spectral shapes (PL, ECPL) for the sources seem to describe the data correctly. Overplotting the spectra of A, B and C (see Figure 36 (a)) proves again that the spectra of those are quite similiar and strengthens the suggestion to describe those with one single common spectrum. Figure 36 (b) shows also a butterfly diagram but here for the composite source 1646 (the others are basically the same and can be found in the appendix).
By integrating[30] the flux over the whole energy range (100 GeV - 100 TeV) the energy flux ϕ_{E} of the source can be determined. When multiplying this with the area in which the flux is distributed the energy emitted, also referred as luminosity, can be derived. Here, the assumption was made that the energy is emitted from the source in a radial symmetic manner leading to an area of $A = 4\pi r^2$ where r is the distance to the source. The distance used to calculate the luminosity is the same as used by HESS Collabortion (2011) and has a value of 4.3 kpc. Table 7 shows the calculated energy content of emission regions A, B and C of Model Vb as well as 1646 of Model VI.
The errors were calculated with an Gaussian error propagation of the integrated energy flux, the derviation can be found in the appendix.

Model	Source	ϕ_{E} 10^{-11}erg cm^{-2} s^{-1}	E 10^{34}erg s^{-1}
Vb	A	0.39	0.87 ± 0.18
	B	0.45	0.99 ± 0.16
	C	0.59	1.30 ± 0.23
VI	1646	1.23	2.72 ± 0.28

Table 7: Calculation of the energy content for the different sources of Model Vb and VI.

[30]For this the method `eflux` was used which integrates the function (PL) with the best fit values from E_{min} to E_{max}.

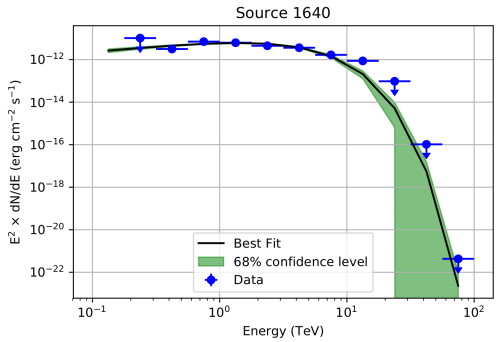

(a) Butterfly spectrum of source HESS J1640-465 for the Model Vb.

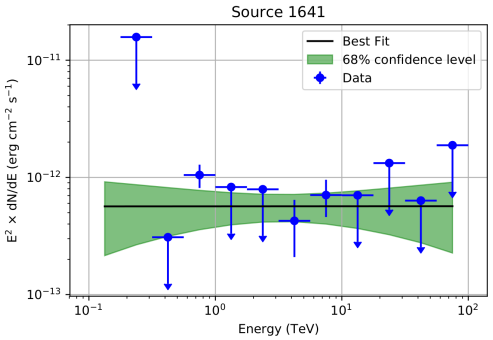

(b) Butterfly spectrum of source HESS J1641-463 for the Model Vb.

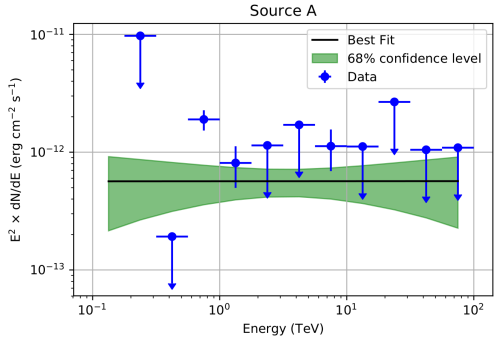

(c) Butterfly spectrum of source A for the Model Vb.

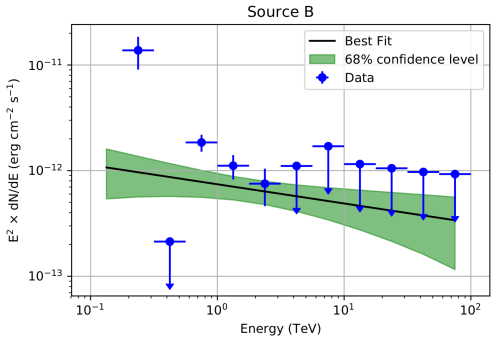

(d) Butterfly spectrum of source B for the Model Vb.

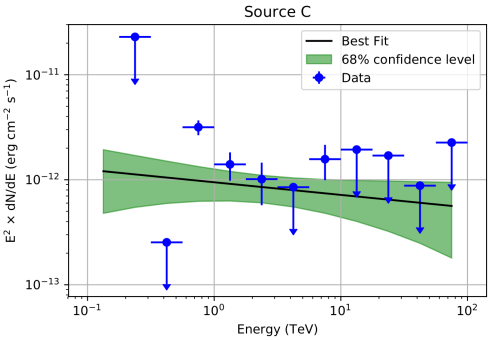

(e) Butterfly spectrum of source C for the Model Vb.

Figure 35: Butterfly spectra for the individual sources of Model Vb.

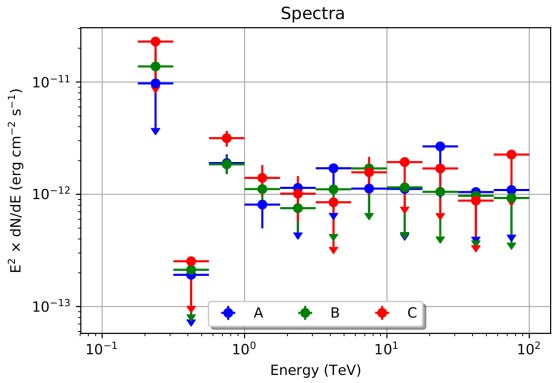

(a) Overplotted spectra of the emission regions A, B and C of Model Vb.

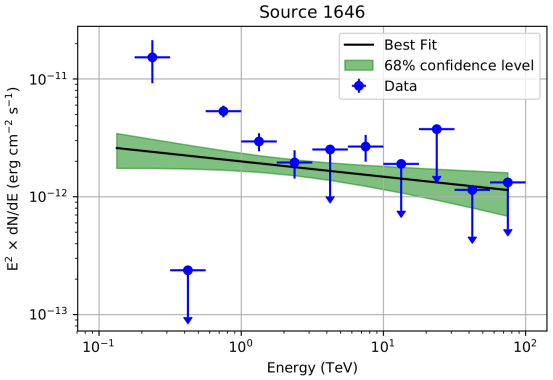

(b) Butterfly spectrum of source 1646 for the Model VI.

Figure 36: Spectra of A, B and C for Model Vb (a) and a butterfly diagram for 1646 of Model VI (b).

4.2.3 Modelling of the Spectra

After the derviation of a field of view model for describing the morphologies and the spectra of the emission regions of Westerlund 1 , a natural question that arises is from which particle population these diffuse γ-rays could originate. Therefore, a modelling of the non-thermal spectra was applied by using `naima`.

`naima` is a open source Python package providing models for computation of non-thermal radiation based on given particle distributions of relativistic protons and electrons. This is done by a MCMC[31] fitting of X-ray and γ-ray spectra. Therefore, several particle distributions (PL, ECPL, etc.) and non-thermal radiative models (IC, π^0 decay, etc.) are given by `naima` (Zabalza, 2015). For the fitting of the spectra the first spectral points were excluded because it seems that the background model doesn't describe the data correctly in the lowest energies. Because the γ-ray spectra of the emission regions/composite model are power laws this was also assumed for electrons/protons creating those. Furthermore, it was assumed that the measured photons arise from inverse Compton scattering or from pion decays.

First, an inverse Compton (IC) radiative model was used to describe the spectra which can be found in Figure 37 for the emission regions A, B and C as well as for the composite model 1646. For this the further assumptions are made: the used power law has also a pivot energy of 1 TeV, the photons which get up scattered by the relativistic electrons are CMB (Cosmic Mikrowave Background[32] (Yardley, 2019).) photons and the distance at which the photons arise is 4.3 kpc.

[31] Markov Chain Monte Carlo is a sampling algorithim used to solve high-dimentional problems (Andrieu et al., 2003).

[32] The cosmic microwave background is a radiation which got emitted 400,000 years after the Big Bang and has now a temperature of about 3°

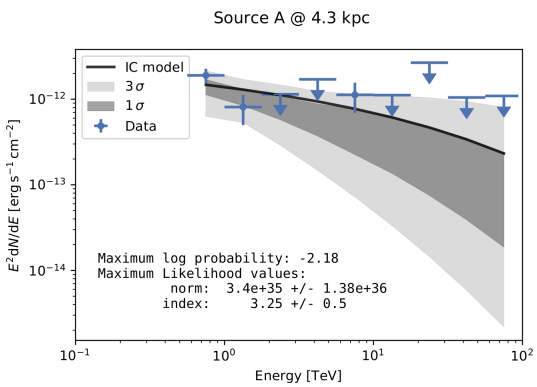

(a) Modeled spectrum of emission region A with an IC approach.

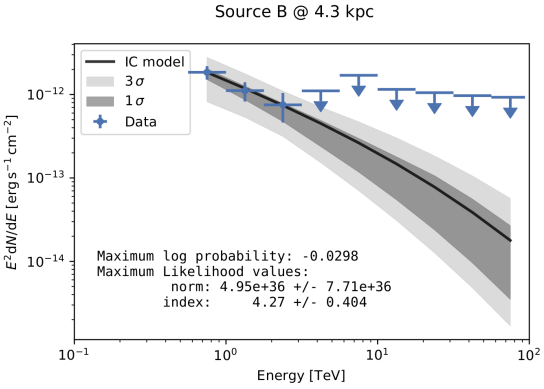

(b) Modeled spectrum of emission region B with an IC approach.

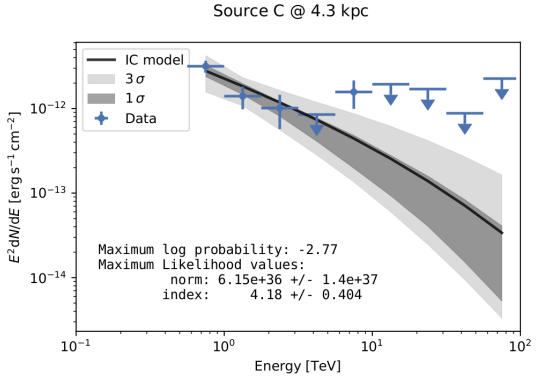

(c) Modeled spectrum of emission region B with an IC approach.

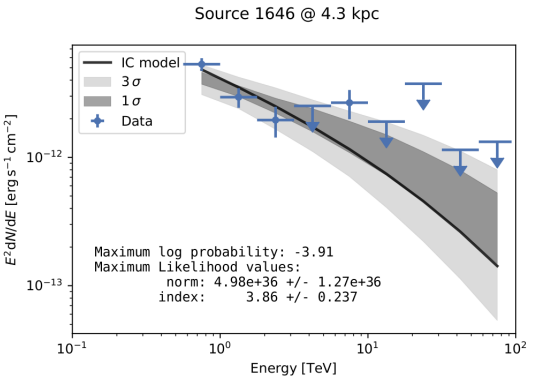

(d) Modeled spectrum of the composite model 1646 with an IC approach.

Figure 37: Modeled spectra of emission regions A, B and C as well as 1646 with an inverse Compton radiative model.

In this figure the black line indicates the best-fit model, and the grey bands the 1σ and 2σ confidence interval. The printed numbers are the parameter values of the underlying electron distribution with the given likelihood probability. Table 8 gives an overview over the fitted electron distribution parameters for emission region A, B and C and the composite model 1646.

Source	Normalizaion @ 1 TeV 10^{36}eV^{-1}	Spectral index	Max. Log L
A	0.34 ± 1.38	-3.25 ± 0.5	-2.18
B	4.95 ± 7.71	-4.27 ± 0.41	-0.03
C	6.15 ± 14	-4.18 ± 0.41	-2.77
1646	4.98 ± 1.27	-3.86 ± 0.24	-3.91

Table 8: Electron distribution parameters for the fitted spectrum of emission regions A, B and C as well as for th composite model 1646.

Also a hadronic model was used, plots referring to this are shown in Figure 38 again with the

underlying parameters for protons colliding with atomic hydrogen density ($n_{HI} = 0.24\,\mathrm{cm}^{-3}$ (HESS Collaboration, 2011)), creating neutral pions which in turn decay into photons, are printed in the graph.

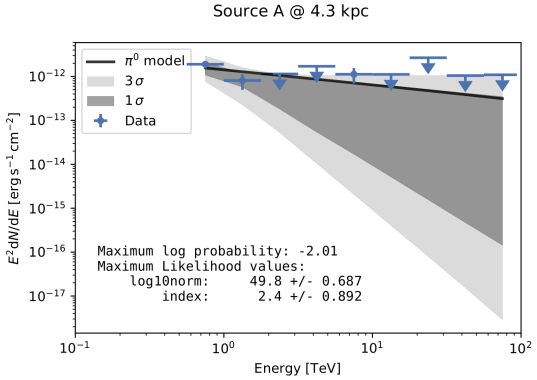

(a) Modeled spectrum of emission region A with a π^0 approach.

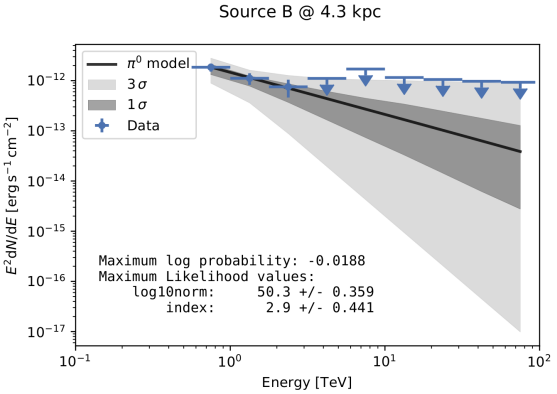

(b) Modeled spectrum of emission region B with a π^0 approach.

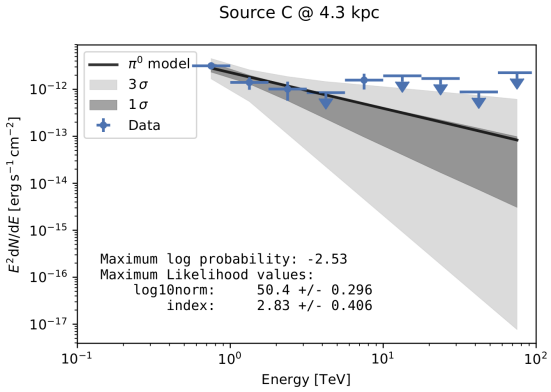

(c) Modeled spectrum of emission region C with a π^0 approach.

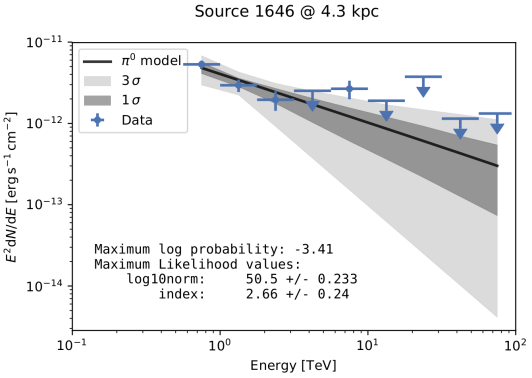

(d) Modeled spectrum of the composite model 1646 with a π^0 approach.

Figure 38: Modeled spectra of emission regions A, B and C as well as 1646 with a π^0 radiative model.

A collection of the parameters of an assumed proton population can be found in Table 9.

Source	log10norm @ 1 TeV	Spectral index	Max. Log L
A	49.80 ± 0.69	-2.40 ± 0.90	-2.01
B	50.30 ± 0.36	-2.90 ± 0.44	-0.02
C	50.40 ± 0.30	-2.83 ± 0.41	-2.53
1646	50.5 ± 0.24	-2.66 ± 0.24	-3.41

Table 9: Proton distribution parameters for the fitted spectrum of emission regions A, B and C as well as for th composite model 1646.

4.3 X-rays

The analysis of X-ray data works a little bit different than in γ-rays but uses the same approach in calling different methods one after another to process the data step-by-step. ESAS (Extended Source Analysis Software) of XMM SAS is used when observing diffuse X-ray emission. It was written for the data analysis of EPIC observations when measuring diffuse X-ray emission and extended objects. Furthermore, the software package is able to create quiescent particle background (QPB) spectra as well as background subtracted images that are also exposure corrected. Another implementation is the creation of mosaic images of multiple and not necessarily coaligned observations (Snowden and Kuntz, 2019). There are several data taken of Westerlund 1 used for this analysis. As the field of view of *XMM* (30') is way smaller than the H.E.S.S. FoV (5 by 5 degrees) the plan is to include data that lie in the region around Westerlund 1 to "extend" the field of view therefore the data in Table 10 were used.

Source	ID	Name	Position (RA, DEC)	Duration (s)
1a	0404340101	Westerlund 1	251.793°, −45.871°	47908
1b	0311792001	Westerlund 1 AXP	251.793°, −45.871°	33906
2a	0679810101	IGR J16418-4532	250.461°, −45.541°	20518
2b	0679810201	IGR J16418-4532	250.461°, −45.541°	14190
2c	0405180501	IGR J16418-4532	250.461°, −45.540°	39618
3	0206380301	IGR J16420-4530	250.423°, −45.501°	23225
4a	0679810301	IGR J16479-4514	252.027°, −45.202°	23918
4b	0206380701	IGR J16479-4514	251.975°, −45.233°	14413
4c	0512180101	IGR J16479-4514	251.975°, −45.236°	37366

Table 10: List of observations choosen for the analysis.

The listed data were provided from the data archive of the Dr. Karl Remeis Observatory. There are additional observations available, however they are unusable because of wrong observation modes. The CCDs of the EPIC on board of the *XMM-Newton* satellite can be operated in different modes: full frame, extended full frame (only for PN), partial window and timing. Measurements taken in the full frame or for the PN CCDs even in extended full frame mode include all pixels of all CCDs (7 for MOS, 12 for PN) read out so that the whole FoV is covered. Whereas in the partial window modes only parts and some pixels are read out in the following manner: for the MOS detectors only the middle CCD is operated in this mode as either an area of 100 by 100 pixels (small window mode) or 300 by 300 pixels (large window mode) are read out, for the PN detector the large window mode means reading out only half of the CCDs and in the small window mode only parts of one single CCD is read out. Furthermore, there is also the timing mode in which each row is contracted into an one dimensional row for reading out the data at a high speed (European Space Agency,

2019c). Unfortnuately, measurements of CXOU J164710.2-455216 (close to the position of Westerlund 1) were taken in the small window mode which is not usable for this analysis because all possible diffuse emission is not measured.

Before images of the 30' field of view or spectra for each observation can be created filtering the data of soft proton (SP) flares[33] must take place. Therefore, the tasks `pn-filter` and `mos-filter` are called one after another after pre-processing of the data with `epchain` (for PN) and `emchain` (for MOS) took place. Additionally, diagnostic files are stored which must be examinated to check if data are usable or not. Figure 39 shows an example of such a diagnostic plot with a useful data set in (a) and an example for data not used in this analysis in (b). The uppermost plot shows a count rate histogram which peaks at a count rate value with minimal if at all SP contamination, the middle and lowest graph display a FoV and Corner[34] light curve. These illustrate the count rate at a given time and if this rate is quite high (black colored areas of the graph) as in Figure 39 (b) the data are still strongly contaminated by SPs. Data affected by SP flares were excluded. As some of the observations in Table 10 showed diagnostic histograms similar to those shown in Figure 39 (b) two more observations were already excluded for further processing (2c, 4b). The corresponding histograms for MOS1 only (as all basically look the same) can be found in Figure 63 in the appendix.

After these first data checks, images of the measured data can be created and is described in the following.

[33]Soft proton flares arise from low energy protons in the Van Allen belt (confinement of charged particles caused by the Earth's magnetic field) (Fioretti et al., 2016).

[34]The corners are not exposed areas of MOS and PN CCDs not contributig to the FoV.

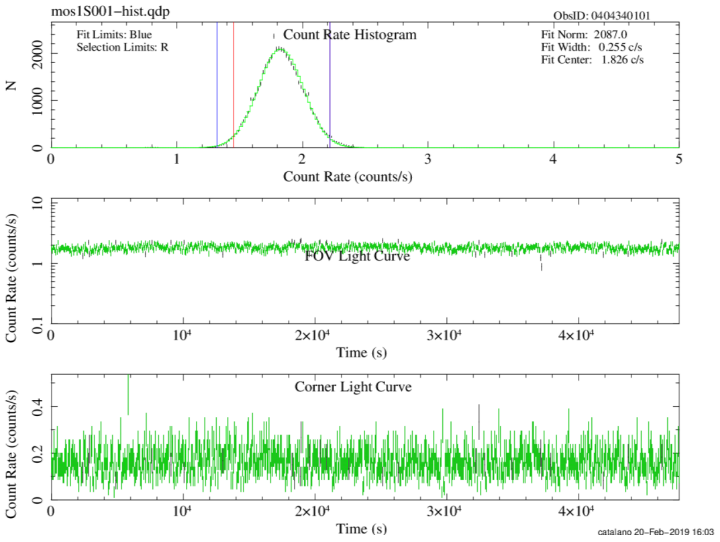

(a) Diagnostic plot of the Westerlund 1 observation 0404340101.

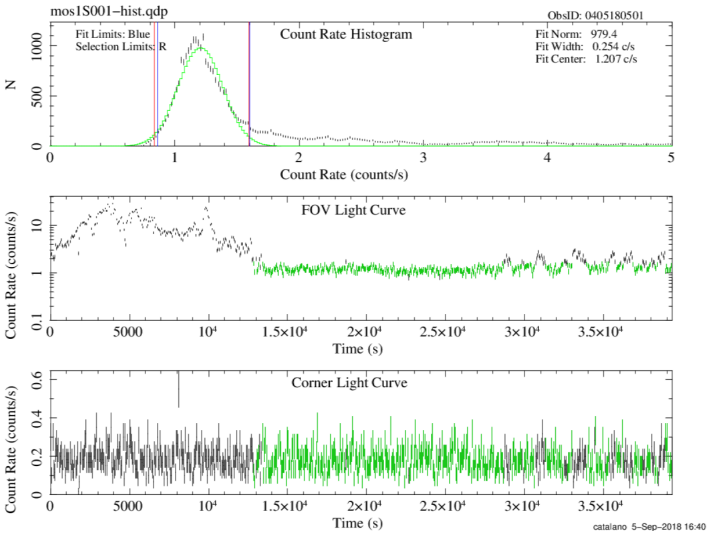

(b) Diagnostic plot of the observation 0405180501 excluded showing SP contamination.

Figure 39: Diagnostic plots for Westerlund 1 and another observation for illustrating good and bad data shown only for MOS1 as the plots for the other detectors look alike (see Figure 62 for Westerlund 1 in the appendix).

4.3.1 Imaging

`pn-` and `mos-filter` also create images of the SP filtered data, examples for that are given in Figure 40 for Westerlund 1.

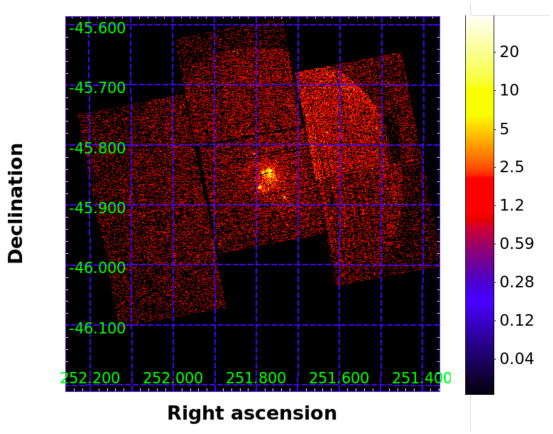

(a) Sky image of the filtered data of the Westerlund 1 observation 0404340101 measured in MOS1.

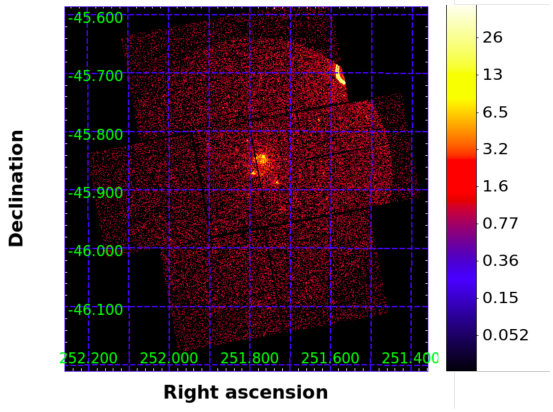

(b) Sky image of the filtered data of the Westerlund 1 observation 0404340101 measured in MOS2.

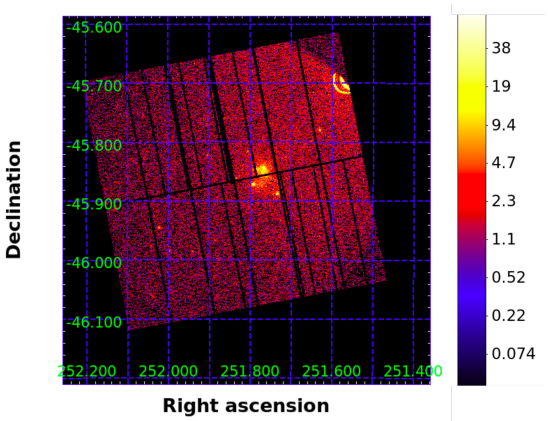

(c) Sky image of the filtered data of the Westerlund 1 observation 0404340101 measured in PN.

Figure 40: Sky image of filtered data of Westerlund 1 measured in each detector. MOS2 and PN show stray light most likely orginating from the LMXB in the vicinity.

Recognizable is that in the middle and around the pointing position of Westerlund 1 there is some diffuse emission as well as some bigger X-ray sources. MOS2 and PN have some small stray light in the upper right corner most likely orignating form the LMXB close by. This feature is also visible in the publication of Kavanagh et al. (2011). Other observations greatly affected by stray light were excluded for further processing, these include 2a, 2b, 3, 4a and 4c (see Figure 64 in the appendix). Single reflections from the individual mirror shells can be seen in those.

The black lines in Figure 40 (c) reveal broken columns of the PN CCDs. To avoid the bigger point sources as well as the stray light in the data, regions can be selected that will be included or excluded in the analysis. For getting rid of the stray light a region in which the stray light is not apparent was selected (see Figure 41 (a)). Additionally, regions defining the bigger point sources were choosen as seen in Figure 41 (b) and excluded. The selected

regions were applied to all detectors to be consistant.

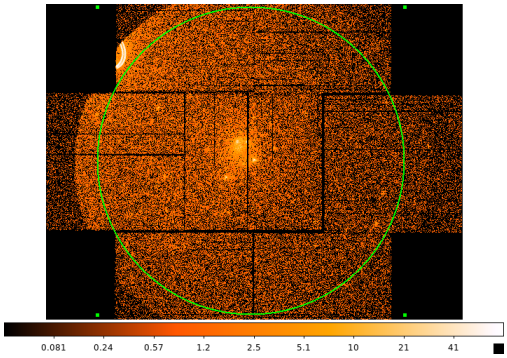

(a) Region indicated as a green cirlce selected for the analysis excluding stary light examplementary shown for MOS2 in detector coordinates.

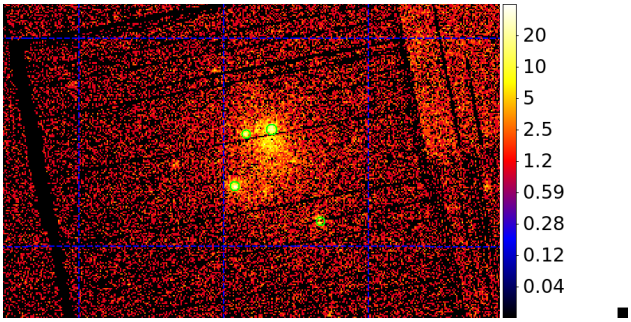

(b) Regions excluded for the analysis indicated by green cirlces.

Figure 41: Regions included and excluded for the analysis applied to all detectors.

In addition, to the diagnostic histogram there are other ways to check if the data of a particular observations are usable. This can be done by examining if the MOS CCDs were working in an anomalous state (see Figure 42) if this is the case there is the possibilty of excluding the affected CCD. The effect of an anomalous CCD is apparent if there are many more counts as in their normal state as shown in Figure 42 (a) for CCD 4. Also visible is that CCD 6 didn't measure any counts at all. But this is because that particular CCD got lost after a meteorite hit in 2005 (Snowden and Kuntz, 2019).
In this analysis extended diffuse emission is of interest and therefore the task *cheese* is used in which a source detection routine will be run, creating a source list and masks the detected point sources. When calling *cheese* a energy band in which the sources should be detected can be set as well as a minimal distance between point sources. Another parameter that can be set is `scale`, e.g. to 0.25, it removes point sources down to 'a level where the surface brightness of the point source is one quarter of the surrounding background' (Snowden and Kuntz, 2019). Figure 43 shows masks created by *cheese* for the Westerlund 1 observation 0404340101 with the whole band ranging from $300 - 10000\,\mathrm{eV}$, a minimal distance between the point sources of $40''$ and a `scale` parameter of 0.25.

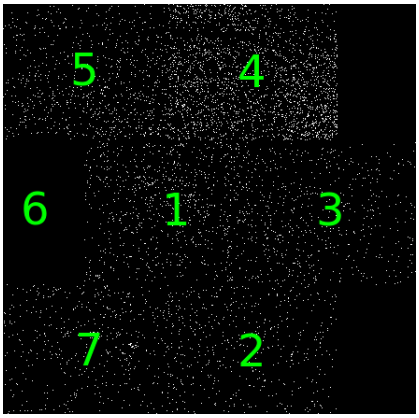

(a) Event image of MOS1 of the Westerlund 1 observation 0404340101 showing a bad CCD 4.

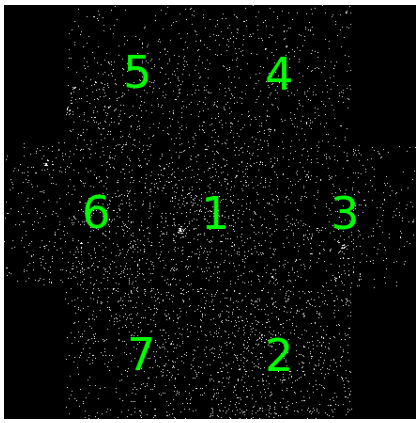

(b) Event image of MOS2 of the Westerlund 1 observation 0404340101.

Figure 42: Event image plots for MOS1 and MOS2 of the Westerlund 1 observation 0404340101.

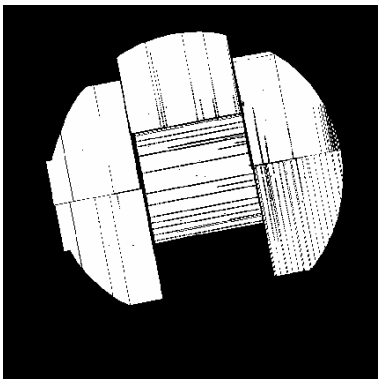

(a) 'Cheese' mask for MOS1.

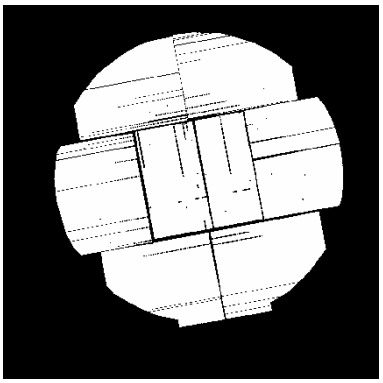

(b) 'Cheese' mask for MOS2.

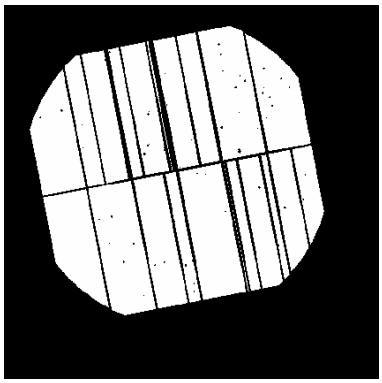

(c) 'Cheese' mask for PN.

Figure 43: 'Cheese' masks created by the tool *cheese* for the Westerlund 1 observation 0404340101. The black lines between the CCDs indicate the gaps between them and the ones on the CCDs broken columns.

By running `mos-` and `pn-spectra` intermediate files for further processing and creation of model background spectra and images are build. The parameter `ccdX` for each CCD can be set (X being numbers ranging fom 1 to 7 corresponding to the CCDs) denoting if it should be used or not for this task and again an energy range is select. Additionally, all tools described from here on are also taking calibration data which contain measurements when the filter wheel[35] is closed meaning that only CR enter the detector and therefore provide a clean measure for the particle background spectra and images which are created by calling the methods `mos-` and `pn-back`. These have to be run for different energy bands and regions (see later) seperately where the CCD parameter is set again. All parameters should be the

[35] A wheel with different filters to block radiation (IR, visible and UV) might contaminating the X-ray measurements (ESA, 2018b).

same as the ones used for `mos-spectra` and `pn-spectra`. The mentioned tasks create also diagnostic files that should be checked before proceeding further, e.g. rate hardness[36] plots for each CCD (see Figure 44).

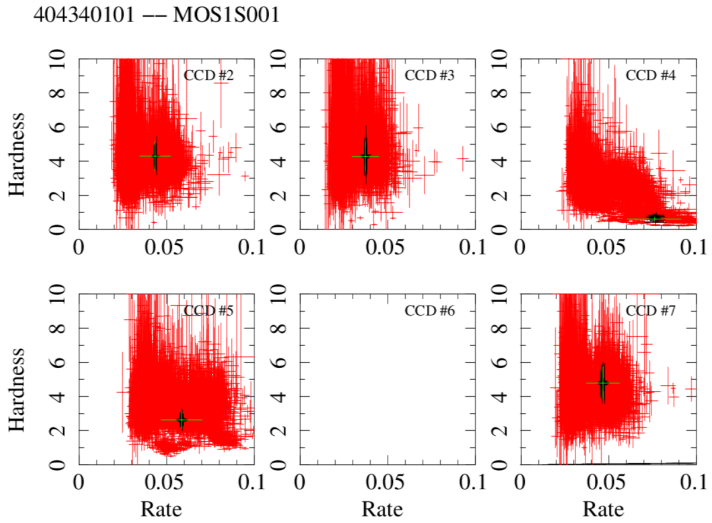

Figure 44: Hardness ratio plot for MOS1 of the Westerlund 1 observation (1a) showing that CCD 4 is not working properly. Red points indicate the whole data set whereas the black points show the selected data. The hardness plots for the other detectors MOS2 and PN are given in the appendix.

Those rate hardness plots show the full data set in red points while the black points are the selected data. The green cross shouldn't be located in the 'anomalous state tail' in the right lower corner/tail (low hardness but high rate). If this is the case as illustrated in Figure 44 the tasks `mos-spectra`/`pn-spectra` and `mos_back`/`pn_back` have to be run again. To take a not properly working CCD into account the parameter for the corrsponding CCD is set to '0' instead to '1' to exclude it.

The tasks `mos-filter` and `pn-filter` might not remove all the SP contamination, therefore the tool `proton` is called, after the data are binned, taking into account the residual SPs with a power law with a corresponding index and normalization. These values are given by fitting the spectrum which is described later on. `proton` takes the binned data of the measurement for each detector seperately, the parameters set for in- or excluding individual CCDs, the energy band ($300 - 10000\,\mathrm{eV}$) and the soft proton indices as well as the corresponding normalization from the spectral fit. `proton` output files contain soft proton images in detector coordinates but can be transformed into sky coordinates with `rot-im-det-sky`. Images of each detector for the model particle and soft proton background can be found in the appendix. Another image that could be created is the one of the solar wind charge exchange (SWCE), but as

[36]The hardness is defined as HR=$\frac{H-S}{H+S}$ with H a hard band ranging from $1.0 - 10.0\,\mathrm{keV}$ and S a soft band ranging from $0.2 - 1.0\,\mathrm{keV}$ (Robrade and Schmitt, 2006).

the interest is more on the higher energies and SWCE is dominating betwenn $0.3 - 1.0$ keV it is neglected here. The task *comb* combines all images of the different detectors, so that there is a combined count image, exposure image, model particle background image and a model soft proton background image for the selected energy band as well as the selected region in sky coordinates (see Figure 45 (a)). By running the task *adapt* a background subtracted and exposure corrected image is created and corresponds to the final image of this observation and is shown in Figure 45 (b).

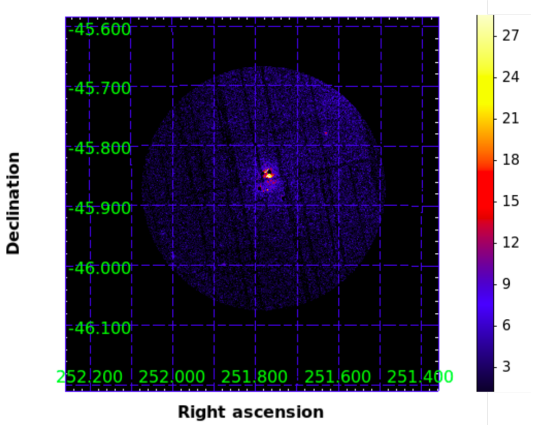

(a) Combined image all detectors included for the set energy band and region.

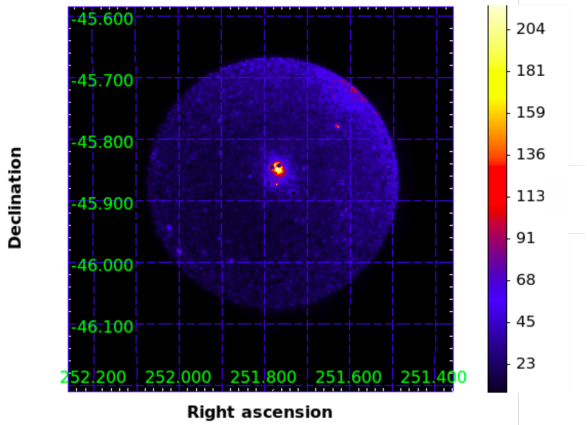

(b) Background subtracted and exposure corrected image of the combined detectors.

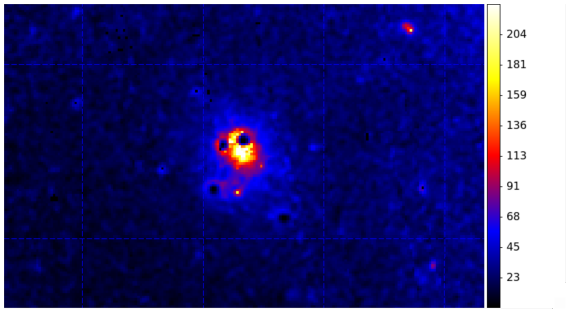

(c) Zoomed view of the background subtracted and exposure corrected image of the combined detectors.

Figure 45: Combines image of all detectors (a) as well as a background subtracted and exposure corrected image (b). (c) shows a zoomed view of (b).

Figure 45 (b) shows in the right upper corner a higher excess emission, this might me due to the close by LMXB and in the zoomed view (see Figure 45 (c)) the extended diffuse X-ray emission is clealy visible. As non-thermal emission would be seen in the higher energies there were two bands defined for creating images, a soft band ranging from 0.3 to 3 keV and a hard band ranging from 3 to 10 keV, respectively (see Figure 46).

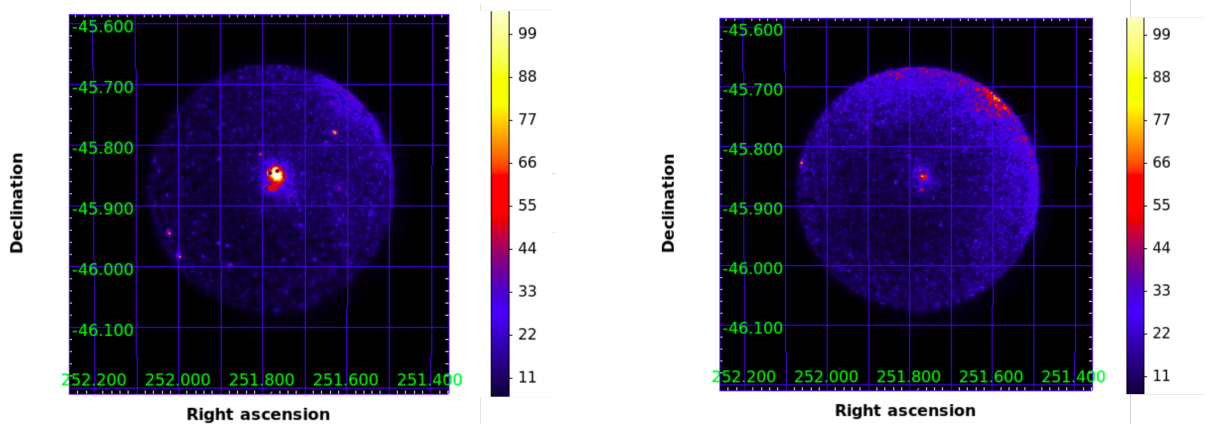

(a) Background subtracted and exposure corrected image of Westerlund 1 in the soft band.

(b) Background subtracted and exposure corrected image of Westerlund 1 in the hard band.

Figure 46: Background subtracted and exposure corrected image of Westerlund 1 in two bands.

Clearly visible is that most of the diffuse emission is appearing in the soft band but also some little emission is seen in the hard band, maybe of non-thermal origin. Also the emission in the right upper corner originating from the LMXB, is mostly occuring in the hard band. For getting better statistics of the Westerlund 1 emission the other observation (1b) was pre-processed and checked. But at the point of taking a look at the first sky image it was recognized that the magnetar CXOU J164710.2-455216 was in an active state (see Figure 47). It was tried to cut that region out to get at least some diffuse emission.

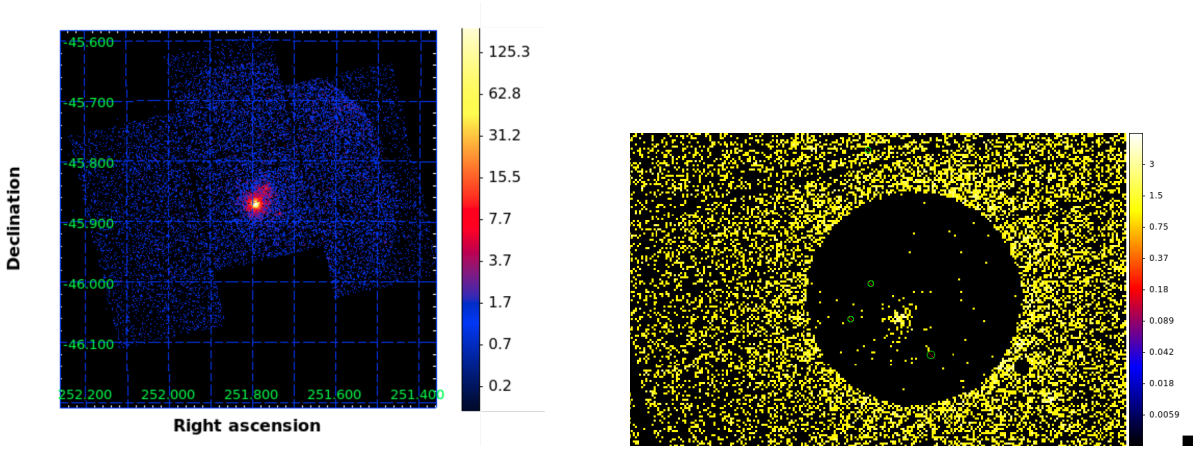

(a) Sky image of the other Westerlund 1 observation in which the magnetar is in flaring state shown for MOS1 (for the other detectors see appendix).

(b) Image of the observation 1b with the cutted region with some counts left.

Figure 47: Sky image of the other Westerlund 1 observation in which CXOU J164710.2-455216 is active as well as the attempt to cut the region.

But when cutting out the region and further process the data there are still some counts left in the cut region which shouldn't happen. Based on that there were some attempts made to

get rid of the counts in that region like further limitation of the energy range, cutting out the region in another way by running a skript provided by Jonathan Knies (Knies, 2019) and the same selected region was applied to another observation to check if this is somehow the mistake. Unfortnuately, all the different approaches were unsuccessful which is not fully understood yet. One idea to explain that behavior is that pile-up[37] is an issue. When pile-up appears several events measured in one pixel during one read out cysle will be interpreted as one single photon with an energy which is actually the sum of the incoming photons and is therefore wrong. This leads to a hardening of the spectrum. If there is indeed pile-up can be checked with the task `epatplot`. It takes the event files of the detectors and plots the event pattern statistics showing model distributions of single, double, etc. events and when these significantly diverge from the measured ones there is a strong indication for pile-up. Figure 48 shows the plots for checking the data if pile-up occurs. The different colors indicate different multipicities for the events. The important parameters to look at are `s` and `d`, those values should be around 1 when no pile-up is occuring as these give the ratio of observed-to-model events (SOC/SSC, 2019).

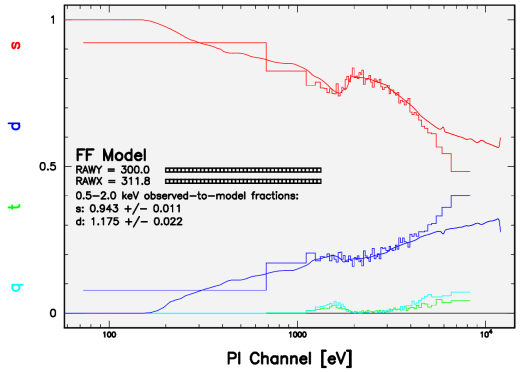

(a) Pile-up plot for MOS 1.

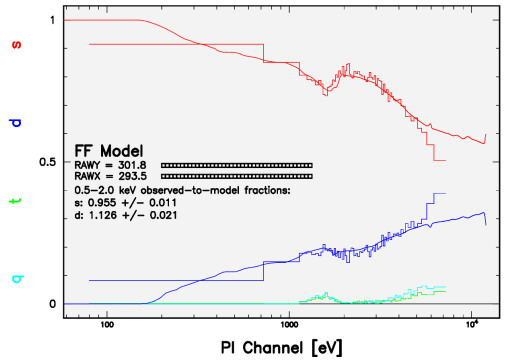

(b) Pile-up plot for MOS 2.

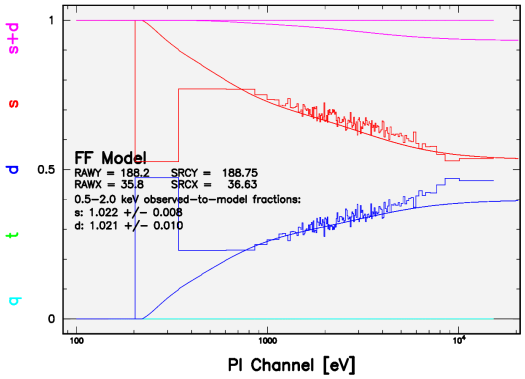

(c) Pile-up plot for PN.

Figure 48: Plot for checking if pile-up occurs for the different detectors.

[37]Pile-up is the phenomenon when more than one X-ray photon hits a camera pixel or neigboring pixels during one read out cycle. (European Space Agency, 2019c).

When checking these one recognizes that the vales are not 1 except for the PN detector, indicating that pile-up is indeed an issue here. As the correction for that would have been too time consuming this was not applied and the data were excluded for this analysis.

4.3.2 Spectral Analysis

The X-ray data were modeled with the help of XSPEC[38]. XSPEC takes the data of all three detectors, response matrices[39], a model describing the data and background and a model describing the soft proton contamination. There are lots of model components that can be used to describe the data as well as the background correctly therefore only the used ones are described. `apec`, `nei`, `vnei`, `gauss`, `pow` and `phabs` are the used components for modeling the source and the background spectrum. The thermal component `apec` describes an emission spectrum arising from collisionally-ionized diffuse gas with a particular temperature. Whereas, `nei` and `vnei` represent a collisional plasma model in non-equilibrium ionization with a constant temperature. `vnei` takes also abundences of elements as parameters and also an ionization timescale after which the plasma is in equilibrium again. `gauss` as the name already tells is a gaussian line profile for the describtion of lines with a specific energy and width. Moreover, `pow` is a simple photon power law with nomalization and photon index. `phabs` describes a photoelectric absorption with just taking a hydrogen column density equivalent n_H (Arnaud et al., 2018).

Background Emission

There are five components that describe the background: `apec + phabs*(apec + apec +pow)` whereas the unabsorbed `apec` demonstrates a cool ($E \sim 0.1\,\mathrm{keV}$) thermal component originating from the Local Hot Bubble. The absorped emission of the cooler and hotter halo is taken into account with the other `apec`s. One apec is fixed at a temperature of 0.1 keV whereas the other one is fitted between 0.25 and 0.7 keV. Lastly, the `pow` represents the unresolved cosmic X-ray background. Also some of the parameters for all of these backgrounds can be linked between the detectors and frozen to lower the number of free parameters (Snowden and Kuntz, 2019). Additionally, there are two prominent detector lines, one at 1.49 keV and another one at 1.75 keV. Soft proton residuals are modeled with a power law particle distribution with separate diagonal response matrices. For keeping the number of free parameters low as there will be lots of them, some of them can be linked, e.g. the index of the particle background for the MOS detectors. For getting a better background

[38] XSPEC is a command-driven X-ray spectral fitting program (Arnaud et al., 2018).

[39] These matrices give the response of the detector to an incident photon, so to say the probability that a photon of energy E will be detected European Space Agency (2019b).

estimation, there were two regions selected to be fitted. One in which the source is contained and the other one in which there is no source within the field of view (see Figure 49).

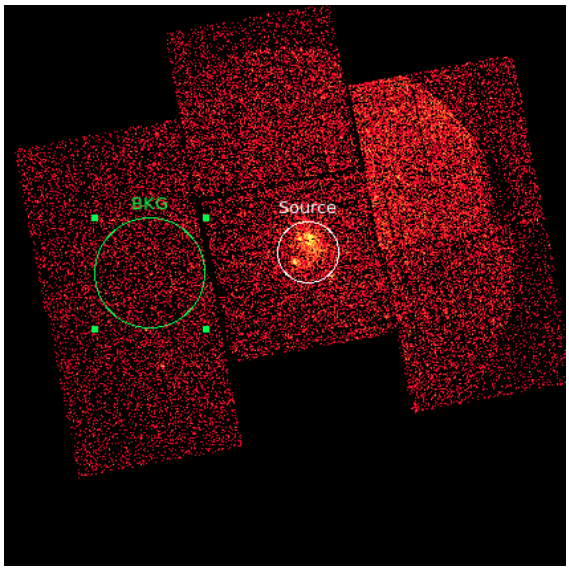

Figure 49: Sky image of Westerlund 1 showing the source and choosen background region for modelling the spectrum.

Source Emission

The hard X-ray emission in Westerlund 1 is expected to be mostly thermal due to thermalized cluster winds originating from collective stellar winds (Kavanagh et al., 2011). But also non-thermal X-ray emission could arise from relativistic electrons being deflected by magnetic fields leading to synchrotron radiation (see 2.2.2). If there is indeed a non-thermal component it could be also seen in the spectrum of the background region. To find out if there is really a non-thermal component in the X-ray data the source spectrum within a circle of $2'$ radius (Kavanagh et al., 2011) was modeled. There were several source models with different components tested to describe the spectrum best: `apec`, `apec+apec`, `nei`, `nei+nei` and for taking a possible non-thermal component into account: `apec+pow`, `apec+apec+pow`, `nei+pow`, `nei+nei+pow`, `nei+apec+pow`, `vnei+apec+pow`, `vnei+nei+pow` and `vnei+vnei+pow`. The choice of starting with an `apec` model was motivated by the work of Kavanagh et al. (2011). The fit is describing the data well when the reduced χ^2 value[40] is around 1, it is given by XSPEC at the end of the fitting routine. It was started with a simple thermal plasma of temperature T, but as the reduced χ^2 (χ^2/ndf) value was 2.35 for 825 number of degrees of freedom a second thermal plasma model was added. The fitted values for the pure `apec` model as well as the spectrum can be found in the appendix. When fitting two thermal plasmas of

[40]The reduced χ^2 value is the χ^2 divided by the number of free parameters (ndf) whereas the χ^2 gives the deviation of the measurement to the expectation: $\chi^2 = \sum \frac{(C_o - C_p)^2}{\sigma^2}$, where C_o and C_p are the observed and predicted counts and σ the error ($\sqrt{C_o}$) (Arnaud et al., 2018)

temperature T_1 and T_2 the reduced χ^2 is way better with 1.90, again the parameters and the spectrum can be found in the appendix. The improvement can also be seen when comparing the spectra of the different models in the appendix. Because a possible non-thermal part is of great interest a power law component was added to the model to account for that. A `apec+pow` model gave a reduced χ^2 of 2.06, a little bit better than only having a thermal plasma model, the fitted parameters and a spectrum can be found in the appendix. Adding a second thermal plasma to the `apec` model gives an even better reduced χ^2 (1.62), the correspondig fit to the spectrum can be found in Figure 50 (a) showing the source and background spectrum. The blue, cyan and magenta colored lines indicate the source spectra of the MOS1/2 and PN detectors, respectively, whereas the black, red and green lines show the spectra of the background region. Straight lines show the soft proton particle background. Taking a closer look at the spectra one might recognize that there are always two lines describing the source model spectra. The lower one describes just the source model and the upper line the source model convolved with the soft proton model. Clealy visible is that the spectral points of the background region aren't described in a good way by the model (solid lines). In the lower energies of the spectrum the model does not describe the spectral points excactly. This might be due to solar wind charge exchange which couldn't be modeled because the statistics were too low.
However, in the higher energies the descrepancy between background data points and model could be solved by adding a non-thermal component with the same spectral index as in the source region to the background spectra (see Figure 50 (b)). This results in an even better reduced χ^2 value of 1.30, compared to the model without a non-thermal component being apparent in the background.

Model	Parameter	Value	red. χ^2
`apec+apec+pow`	N_H (10^{22}cm^{-2})	$2.10^{-0.04}_{+0.04}$	
	kT_1 (keV)	$2.28^{-0.13}_{+0.20}$	
	A_1 (10^{-4} arcmin^{-2})	$1.68^{-0.21}_{+0.21}$	
	kT_2 (keV)	$0.74^{-0.04}_{+0.05}$	
	A_2 (10^{-4} arcmin^{-2})	$4.06^{-0.33}_{+0.34}$	
	Γ	$1.43^{-0.08}_{+0.08}$	
	A_{PL} (10^{-5} erg s^{-1} cm^{-2})	$2.17^{-0.30}_{+0.33}$	
	A_{BKG} (10^{-6} erg s^{-1} cm^{-2})	$9.06^{-0.95}_{+0.97}$	1.30

Table 11: Fitted parameters of the `apec+apec+pow` model.

The errors given here for the best models are determined with the *error* command in the way that the parameter of interest will be variied until the reduced χ^2 value is worse than χ^2/ndf= 2.706 in each direction which corresponds to a 90% confidence interval in comparison to the errors given for the other models in the appendix. Their errors are estimated 1σ errors

which only give an indication to the actual errors. Only these were used because determining the "real" errors for each model would have been too time consuming. Models including thermal plasmas in non-equilibrium even with free metal abundances and temperature parameters kT are used for further improving the model. Different combinations of `nei`, `vnei` and `apec` with an additional power law component also apparent in the background were tested, the important fitted parameters and spectra are given in the appendix. The `vnei+vnei+pow` model has the best fit statistics with a reduced χ^2 of 1.09. A spectrum as well as the fitted parameters are given in Figure 51 and Table 12.

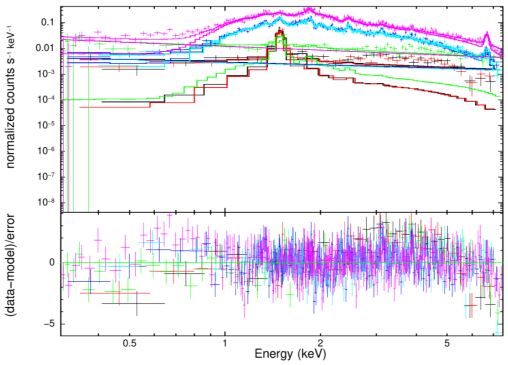

(a) Spectrum modeled with two thermal plasmas of temperature kT_1 and kT_2 and an additional power law component. The red, black and green lines indicate the MOS1/2 and PN detector for the background region and the blue, cyan and magenta lines display the MOS1/2 and PN detector of the source region. The lower plot shows the deviations from the data.

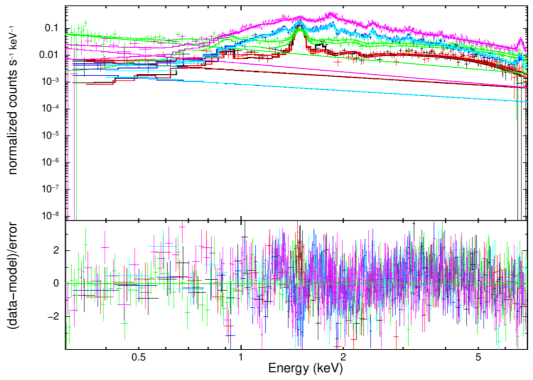

(b) Same spectrum as in (a) but with an power law component added in the background model.

Figure 50: Spectra modeled with a two temperature thermal plasma model and an additional power law component (a) and taking also a power law component in the background into account (b).

Model	Parameter	Value	red. χ^2
`vnei+vnei+pow`	N_H (10^{22}cm^{-2})	$2.29^{-0.15}_{+0.12}$	
	kT_1 (keV)	$2.20^{-0.16}_{+0.26}$	
	Ca ($Ca_\odot$)	$2.77^{-0.89}_{+0.98}$	
	τ_1 (10^{10} s cm^{-3})	$(3.35 \cdot 10^3)^{41}$	
	A_1 (10^{-4} arcmin^{-2})	$1.55^{-0.27}_{+0.25}$	
	kT_2 (keV)	$1.17^{-0.21}_{+0.31}$	
	Mg ($Mg_\odot$)	$0.36^{-0.08}_{+0.10}$	
	Si ($Si_\odot$)	$0.41^{-0.07}_{+0.08}$	
	S ($S_\odot$)	$0.46^{-0.09}_{+0.11}$	
	Fe ($Fe_\odot$)	$0.48^{-0.23}_{+0.27}$	
	τ_2 (10^{10} s cm^{-3})	$4.99^{-1.61}_{+2.90}$	
	A_2 (10^{-4} arcmin^{-2})	$4.26^{-1.15}_{+1.40}$	
	Γ	$1.20^{-0.10}_{+0.09}$	
	A_{PL} (10^{-5} erg s^{-1} cm^{-2})	$1.30^{-0.31}_{+0.33}$	
	A_{BKG} (10^{-6} erg s^{-1} cm^{-2})	$7.78^{-1.05}_{+1.07}$	1.09

Table 12: Fitted parameters of the `vnei+vnei+pow` model.

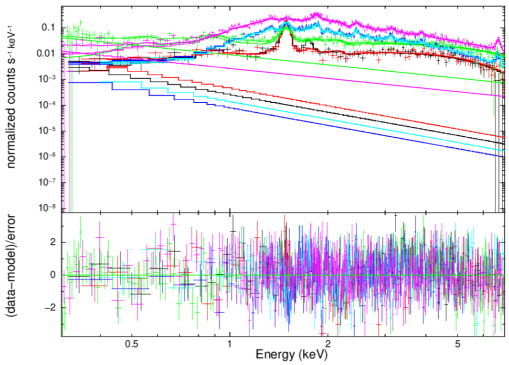

(a) Spectrum modeled with two thermal plasmas in non-equilibrium and an additional power law component also apparent in the background. The red, black and green lines indicate the MOS1/2 and PN detector for the background region and the blue, cyan and magenta lines display the MOS1/2 and PN detector of the source region. The lower plot shows the deviations from the data.

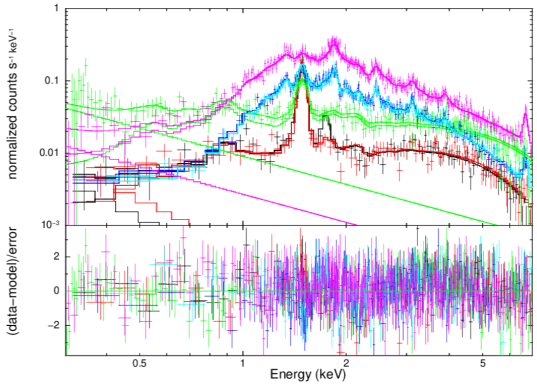

(b) Same spectrum as in (a) in a zoomed view.

Figure 51: Spectrum fitted with a `vnei+vnei+pow` model.

Table 13 shows a summary of all models used in this analysis with their reduced χ^2 values.

Model	χ^2/ndf
`apec`	2.35
`apec+apec`	1.90
`apec+pow`	1.45
`apec+apec+pow`	1.30
`nei`	2.51
`nei+nei`	1.81
`nei+pow`	1.52
`nei+nei+pow`	1.15
`nei+apec+pow`	1.35
`vnei+apec+pow`	1.13
`vnei+nei+pow`	1.14
`vnei+vnei+pow`	1.09

Table 13: Summary of all models applied to the data with their corrsponding reduced χ^2 value.

Determing the total X-ray luminosity between $0.3 - 7\,\mathrm{keV}$ for the source region (2' radius around Westerlund 1) with an assumed distance of $4.3\,\mathrm{kpc}$ gives $2.50 \cdot 10^{32}\,\mathrm{erg\ s^{-1}}$. For comparing the non-thermal flux of the source and background region the given fluxes in Table 12 were normalized to their corresponding areas as they don't have the same size. From that the fluxes give $1.03 \cdot 10^{-6}\,\mathrm{erg\ s^{-1}\ cm^{-2}\ arcmin^{-2}}$ and $1.91 \cdot 10^{-7}\,\mathrm{erg\ s^{-1}\ cm^{-2}\ arcmin^{-2}}$ for the source and background region, respectively. Hence, the flux decreases from the source region to the background region (14.4' distance of the region centers) around one order of magnitude.

4.3.3 Modelling of the Spectrum

`naima` was used to model of the non-thermal X-ray emission by a synchotron radiation model with a underlying power law electron distribution. Therefore, spectral flux points were extracted in four energy bins per decade resulting in a covered energy band of $0.25 - 7.5\,\mathrm{keV}$. Figure 52 shows the modeled spectrum with the fitted parameters of the electron power law and the magnetic field strength necessary.

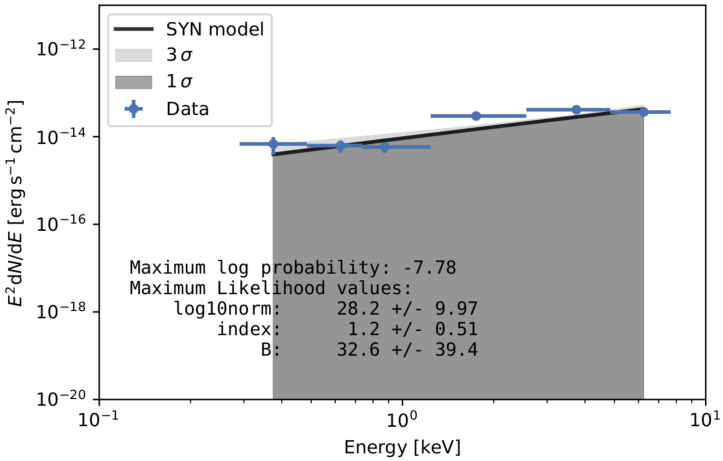

Figure 52: X-ray spectrum modeled with a synchroton radiation model by `naima`.

As one recognizes the 1 and 2σ confidence intervals are covering several orders of magnitude which is not understood yet. The fitted magnetic field strength has a value of $32.6\,\mu$G which is a quite high magentic field even for stellar associations (see 2.2.4).

4.4 Combination

4.4.1 Morphology

Due to missing X-ray observations at the emission regions seen in γ-rays or beyond a search for rims or filaments of a potential superbubble or overlapping regions was not possible.

4.4.2 Spectrum

Non-thermal high energy photons in the X-ray regime are created when (relativistic) electrons gyrotate around magetic field lines and therefore emit synchroton radiation. These high energy electrons could upscatter low energy photons (inverse Compton (IC)) to γ-ray energies. To test if this scenario could happen in and around Westerlund 1, the X-ray and γ-ray spectra were combined and fitted together in `naima` with synchrotron (X-ray) and IC radiation (γ-ray) mechanisms. For that spectral flux points in the X-ray regime were extracted with XSPEC from the spectrum but only from the non-thermal component. The γ-ray flux points are taken from the composite spectrum by excluding the first spectral points. As the spectra are extracted in different regions, quite far away from each other, the X-ray regime is not fitted properly (see Figure 53).

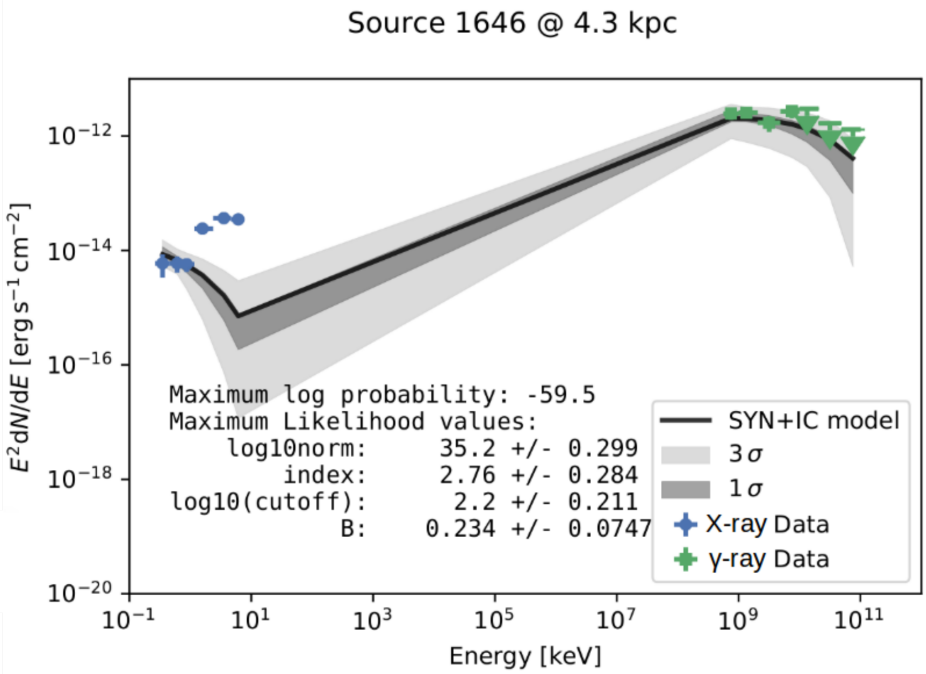

Figure 53: Combined fit of X-ray and γ-ray spectra with a synchrotron and IC model.

5 Discussion

5.1 Morphology

To see if the morphopgy in γ-rays is described in the right way with the new approach of a template based description of the field of view, Figure 54 shows the excess regions around Westerlund 1 from this analysis and from the publication by HESS Collaboration (2011).

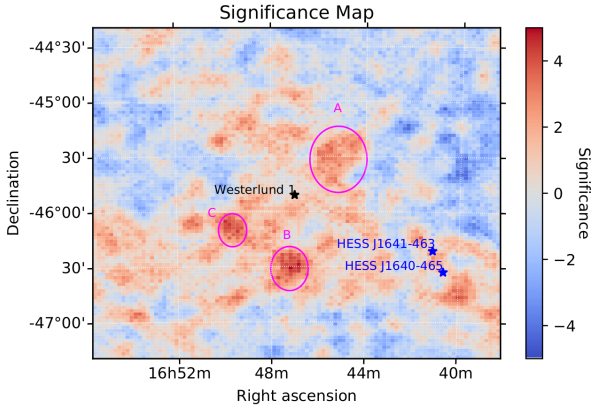

(a) Residual map of Model II with the labeled regions A, B and C.

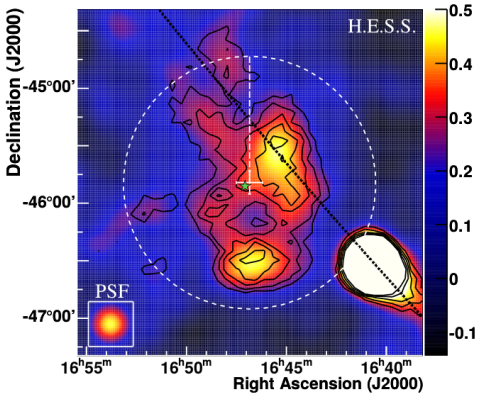

(b) Map showing the excess around Westerlund 1 of the HESS Collaboration (2011) publication.

Figure 54: Residual map of Model II (a) and the excess map (b) of the region around Westerlund 1 from the publication by HESS Collaboration (2011) showing also emission in region A and B but almost no in C.

One should be careful when comparing the two sky maps in Figure 54 of the Westerlund 1 region because the residual map shown from this analysis indicates residual counts whereas the map of the publication shows counts per arcmin^2. Also the residual map of Model II was used in which HESS J1640-465 and HESS J1641-463 are already modeled because here the emission regions A, B and C as well as other diffuse emission is better visible. The emission regions A and B seem to be quite good reproduced although the regions in this analysis seem to be shifted when comparing the relative positions of the regions. This might be explained by different coordinate projections. Additionally, the map taken from HESS Collaboration (2011) does not show any or only small excess around region C which is most likely visible in this analysis due to a larger data set. Also, it should be noted that other substructures as the smaller diffuse emission left next to A or the connections of regions C and B to A are visible. The enhanced excess left next to A might be connected to the CO source C given in Figure 12 as this has roughly the position and around the same distance to Earth (3.5 kpc (Kothes and Dougherty, 2007)) as Westerlund 1 (newly measured distance 3.2 kpc (Aghakhanloo et al., 2019)). This region has a hydrogen density of 35 cm^{-3} (Ohm et al., 2013) and could therefore be target material for accelerated hadrons.

Another difference between the publication and this analysis besides the other analysis software and the larger data set is that for the emission region A a `RadialDisk` model was applied but in the publication a Gaussian shape was used to describe A. Additionally, there was the issue that the fit didn't converge when fitting the emission region A in the beginning of modelling 1646. This might be due to the fact that in this region there is an additional component and was therefore not described correctly. Table 14 gives the start and fitted spatial parameters for emission regions A, B and C for Model Vb and Model VI in comparison with parameters from HESS Collaboration (2011).

Model	Component	Start	Fit	Publication
Vb	$\mathrm{R.A._{A,\,fix}}$ (°)	251.290	-	251.370
	$\mathrm{Dec_{A,\,fix}}$ (°)	-465.528	-	-46.585
	$\sigma_{\mathrm{A,\,fix}}$ (°)	0.35	0.201 ± 0.033	0.35
	$\mathrm{R.A._B}$ (°)	251.819	251.805 ± 0.037	251.682
	$\mathrm{Dec_B}$ (°)	-46.513	-46.519 ± 0.027	-46.513
	σ_{B} (°)	0.25	0.080 ± 0.021	0.25
	$\mathrm{R.A._C}$ (°)	252.443	252.410 ± 0.065	-
	$\mathrm{Dec_C}$ (°)	-46.155	-46.169 ± 0.045	-
	σ_{C} (°)	0.2	0.139 ± 0.035	-
VI	$\mathrm{R.A._{A,\,free}}$ (°)	251.290	251.302 ± 0.042	251.370
	$\mathrm{Dec_{A,\,free}}$ (°)	-45.528	-45.481 ± 0.029	-45.585
	$\sigma_{\mathrm{A,\,free}}$ (°)	0.201	0.167 ± 0.027	0.35
	$\mathrm{R.A._B}$ (°)	251.805	251.806 ± 0.036	251.682
	$\mathrm{Dec_B}$ (°)	-46.519	-46.520 ± 0.025	-46.513
	σ_{B} (°)	0.080	0.075 ± 0.018	0.25
	$\mathrm{R.A._C}$ (°)	252.410	252.410 ± 0.065	-
	$\mathrm{Dec_C}$ (°)	-46.169	-46.169 ± 0.045	-
	σ_{C} (°)	0.139	0.139 ± 0.035	-

Table 14: Start and fitted parameters for emission regions A, B and C of Model Vb and Model VI.

In HESS Collaboration (2011) there was no description of region C. The lowest energy bin ($0.1 - 1\,\mathrm{TeV}$) of the residual map in Figure 31 (a) shows some concentrated positive residuals between HESS J1640-465 and HESS J1641-463 which could arise from leaking CR either from HESS J1640-465 or HESS J1641-463 or both interacting with dense material creating a bridge between those two sources. A comparision of the optimized function values of Model Va (64718.168) and Vb (64711.901) gives that the one for the fixed positional parameters of A is smaller and therefore better which might not be expected because one might think that the global minimum is found at the end of the fitting routine. Unfortunately, it seems that in Model Va only a local minimum was found. As the attempt to fit one single Gaussian of size $\sim 1.1°$ to the data with a best-fit position of Westerlund 1 as carried out in the publication failed a multi-source hypothesis might be even more supported.

Comparing images in the X-ray regime of this analysis with the ones from Kavanagh et al. (2011) (see Figure 55) one recognized that the overall structure is matching which is expected the same data set was used. The only differences are that in this analysis ESAS was used and the PN data were included in contrast to the publication.

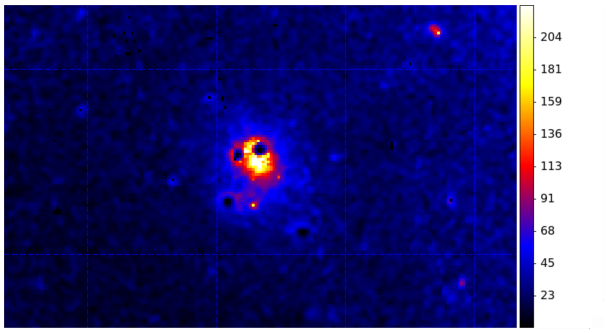

(a) Zoomed view of the background subtracted and exposure corrected image of all detectors combined.

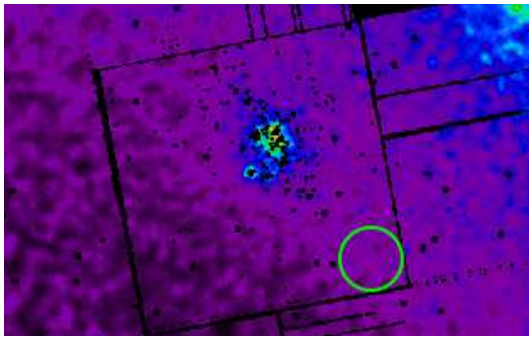

(b) Zoomed view of a smoothed, non-background subtracted combined image of the MOS detectors (Kavanagh et al., 2011).

Figure 55: Zoomed views of images adapted from this analysis and from the publication.

Besides the same structure a small gradient from the lower left to the upper right corner is visible in both image. This is most likely caused by the LMXB close by. Also seen is there are way more point sources excluded by Kavanagh et al. (2011) as in this analysis. A coverage of the region around Westerlund 1 was unfortunately not possible because of missing observations.

5.2 Spectrum

A comparison of the fitted γ-ray spectra of the individual sources of Model Vb as well as at the spectrum of the composite model (Model VI) to the publication (HESS Collaboration (2011)) can be found in Table 15.

A comparision of the fitted indices and the ones from HESS Collaboration (2011) gives that they agree within the statistical errors but the normalizations are fitted $\sim$ one order of magnitude too low which also explains the concentrated positive residuals in Figure 30 (b). The similar behavior of the spectral indices being in agreement within the statistical errors supports the assumption of a missing energy-dependent morphology of HESS Collaboration (2011) but is therefore disfavors to a multi-source hypothesis.

Model	Component	Start	Fit	Publication
Vb	$\phi_{0,\mathrm{A,\ fix}}$ ($\mathrm{cm^{-2}s^{-1}TeV^{-1}}$)	$2.0 \cdot 10^{-13}$	$3.536 \cdot 10^{-13} \pm 1.19 \cdot 10^{-13}$	$2.1 \cdot 10^{-12}$
	$\gamma_{\mathrm{A,\ fix}}$	2.0	1.999 ± 0.176	2.11
	$\phi_{0,\mathrm{B}}$ ($\mathrm{cm^{-2}s^{-1}TeV^{-1}}$)	$2.0 \cdot 10^{-12}$	$4.638 \cdot 10^{-13} \pm 1.236 \cdot 10^{-13}$	$1.4 \cdot 10^{-12}$
	γ_{B}	2.0	2.182 ± 0.166	2.29
	$\phi_{0,\mathrm{C}}$ ($\mathrm{cm^{-2}s^{-1}TeV^{-1}}$)	$2.0 \cdot 10^{-12}$	$5.906 \cdot 10^{-13} \pm 1.992 \cdot 10^{-13}$	-
	γ_{C}	2.0	2.120 ± 0.182	-
VI	$\phi_{0,\mathrm{A,\ free}}$ ($\mathrm{cm^{-2}s^{-1}TeV^{-1}}$)	$4.634 \cdot 10^{-13}$	$1.245 \cdot 10^{-12} \pm 0.217 \cdot 10^{-12}$	$9.0 \cdot 10^{-12}$
	$\gamma_{\mathrm{A,\ free}}$	2.182	2.130 ± 0.105	2.19
	$\phi_{0,\mathrm{B}}$ ($\mathrm{cm^{-2}s^{-1}TeV^{-1}}$)	$4.634 \cdot 10^{-13}$	$1.245 \cdot 10^{-12} \pm 0.217 \cdot 10^{-12}$	$9.0 \cdot 10^{-12}$
	γ_{B}	2.182	2.130 ± 0.105	2.19
	$\phi_{0,\mathrm{C}}$ ($\mathrm{cm^{-2}s^{-1}TeV^{-1}}$)	$4.634 \cdot 10^{-13}$	$1.245 \cdot 10^{-12} \pm 0.217 \cdot 10^{-12}$	-
	γ_{C}	2.182	2.130 ± 0.105	-

Table 15: Start and fitted spectral parameters for the emission regions A, B and C of Model Vb and Model VI compared to the published values.

As mentioned in 4.2.2 the second flux point in almost every spectrum is beneath the best-fit and even beneath the confidence interval. This might be explained by the assumption that the background model is not described correctly in the lower energy bins leading to a wrong determined flux. The energy content of 1646 was determined to $2.72 \cdot 10^{34}\,\mathrm{erg\ s^{-1}}$ which is one order of magnitude lower than the value given in HESS Collaboration (2011): $1.9 \cdot 10^{35}\,\mathrm{erg\ s^{-1}}$ at an assumed distance of 4.3 kpc. This is resonable because the fitted normalization in this analysis is also about one order of magnitude less. Recently there has been a publication on a more precise measurement on the distance to Westerlund 1 (Aghakhanloo et al., 2019) which results in a modification of the energy content in the follwing way:

$$E_{3.2\,\mathrm{kpc}} = E_{4.3\,\mathrm{kpc}} \cdot \left(\frac{3.2}{4.3}\right)^2 = 1.51 \cdot 10^{34}\mathrm{erg\ s^{-1}} \tag{6}$$

(HESS Collaboration, 2011). Applying Equation 6 to the values of this analysis for the composite model as well as for the publication one obtains $1.51 \cdot 10^{34}\,\mathrm{erg\ s^{-1}}$ and $1.05 \cdot 10^{35}\,\mathrm{erg\ s^{-1}}$, respectively. Underlying particle distributions (electrons, protons) with different radiation mechanisms (IC, π^0 decay) were fitted with `naima` to the γ-ray data. When comparing the log-likelihood probabilty one recognizes that the one for IC is a little bit higher. Therefore, a scenario in which relativistic electrons scatter up CMB photons is more likely than a hadronic scenario. This is in contradiction to the assumption of a hadronic scenario of HESS Collaboration (2011). However, one should keep in mind that the distance which was used in `naima` is 4.3 kpc, not the newly determined 3.2 kpc.

The X-ray spectrum was fitted with several different models but for a comparison to the publication by Kavanagh et al. (2011) here only the two temperature thermal plasma, the

thermal plasma with a non-thermal component as well as the best model of this analysis (`vnei+vnei+pow`) are discussed. A table with all the important parameters is shown below (see Table 16).

Model	Parameter	Value	Value pub	χ^2/ndf	χ^2/ndf pub
`apec+apec`	N_H (10^{22}cm^{-2})	$2.04 \pm 2.51 \cdot 10^{-2}$	2.03		
	kT_1 (keV)	$2.87 \pm 9.02 \cdot 10^{-2}$	3.07		
	kT_2 (keV)	$0.79 \pm 2.78 \cdot 10^{-2}$	0.68	1.90	0.971
`apec+pow`	N_H (10^{22}cm^{-2})	$2.11 \pm 2.42 \cdot 10^{-2}$	2.07		
	kT (keV)	$0.84 \pm 2.23 \cdot 10^{-2}$	0.81		
	Γ	$1.93 \pm 7.76 \cdot 10^{-2}$	2.43	2.45	1.14
`vnei+vnei+pow`	N_H (10^{22}cm^{-2})	$2.29^{-0.15}_{+0.012}$	-		
	kT_1 (keV)	$2.20^{-0.16}_{+0.26}$	-		
	kT_2 (keV)	$1.17^{-0.21}_{+0.31}$	-		
	Γ	$1.20^{-0.10}_{+0.09}$	1.09	-	-

Table 16: Parameter comparison of this analysis with the publication by Kavanagh et al. (2011).

The parameters from this analysis and the publication by Kavanagh et al. (2011) of model `apec+apec` and `apec+pow` are similar but the reduced χ^2 value differs a lot which might me explained by the fact that Kavanagh et al. (2011) excluded the PN detector for their analysis. Also they fit their spectrum in the energy range from $2 - 8$ keV in contrast to this analysis ($0.3 - 7$ keV).

The spectrum of this analysis was modeled best with two thermal plasma models in non-equilibrium and an additional power law component. To model this spectrum properly the power law component had to be added to the background region, otherwise the spectrum is not fitted well. This is a strong indicator that there is indeed a non-thermal component apparent in and around Westerlund 1 and therefore hosts relativistic electrons which is in contradiction to Kavanagh et al. (2011). The X-ray luminosity was determined to $2.50 \cdot 10^{32}$erg s^{-1} which is one order of magnitude less than the value Kavanagh et al. (2011) measured ($1.7 \cdot 10^{33}$ erg s^{-1}).

Due to the lack of X-ray observations around the γ-ray emission regions a combination of the spectrum was not applied.

6 Summary and Outlook

This thesis demonstrated a new approach to analyze VHE γ-ray data with a template based analysis approach of the H.E.S.S. field of view of the stellar cluster Westerlund 1. After an introduction to the physics in such a stellar cluster the analysis software *ctools* was shortly presented. Based on that a derivation of a field of view model describing the region around Westerlund 1 (HESS J1646-458) was carried out. These models contain the TeV sources HESS J1640-465, HESS J1641-463 as well as emission regions A, B and C. First (Model Vb), the emission regions were treated as individual sources having their own spectra and in the second approach having the same spectrum, motivated by the fact that the spectral parameters of Model Vb were in agreement within statistical fluctuations (see paragraph 'Modelling of Region A' in 4.2). Both models lead to a good description of the FoV of Westerlund 1 besides some concentrated positive residuals. Residual maps were created as well as profile plots extracted along various lines for a quantitive comparison between models. Additionally, radial profiles were plotted showing the emission in particular sections within the field of view. In the end, no significant sources were found anymore. Also spectra for all sources were extracted based on the models but unfortunately it seems that in the lower energies the background is not described properly by the field of view background model because the flux points appear to be wrong. From those spectra the energy content could be calculated at a distance of 4.3 kpc. A comparison to the publication by HESS Collaboration (2011) lead to the conclusion that this new approach is able to reproduce the measured emission seen around Westerlund 1 in terms of morphology as well as regarding the overall spectral behavior. However, the energy contents differ about one order of magnitude between this analysis and HESS Collaboration (2011). Drawing a conclusion gives that *ctools* is indeed a good tool for analyzing extended diffuse emission as in this case, but it seems that there are still problems, e.g. with finding a global minimum. Also there might be problems regarding the background model especially in the lower energies.

The description of the field of view can likely be improved by removing the excess around HESS J1640-465 and HESS J1641-463. One idea is to apply other model components or again a radial gaussian/disk model after all obvious emission is modeled or try to add another component next to A to describe the region better. Moreover, data from other phases of the H.E.S.S. telescope, e.g. after the camera update of the four small telescopes (Bonnefoy et al., 2017) or even from H.E.S.S. II (all five telescopes including the big one in operation (Hofmann, 2019)), can be used or data with better gamma-hadron seperation can be analyzed. Additionally, there was also an update of the background model in which for example the atmospheric transperancy coefficient is now taken into account. A first attempt to model the data with the updated background model with Model Vb failed. Moreover, one should take

a look at the issue of just finding a local minimum instead a global one. The modelling of the spectrum with `naima` can be improved in the way that the distance should be adjusted or that other radiation fields providing photons for IC scattering are considered as well.

In the X-ray regime the selection of usable data was the first challenge as several important steps have to be taken before starting the creation of the images or modelling the spectrum. Some observations were excluded from the beginning on as the data were measured in a detector mode not usable to this analysis, including data of CXOU J164710.2-455216 a magnetar next to the Westerlund 1 position which could have revealed some diffuse emission. Other observations were excluded because they had still soft proton residuals left even after filtering. Furthermore, data with stray light partly appearing almost over the whole field of view were also excluded. Two data sets were left which were processed further but one of them captured a measurement in which the magnetar was in an active state and pile-up was an issue. Due to time constraints the data of this observation were not corrected for that phenomenon. In the end only one data set was usable from which a background subtracted and exposure corrected image was created revealing diffuse emission around the center of Westerlund 1 (see Figure 45 (c)).
The spectrum was modeled with several models including different combinations of various components. Whereas the best-fit model (red. $\chi^2 = 1.09$) is a two temperature thermal plasma in non-equilibrium and an additional non-thermal component represented by a power law. Moreover, this non-thermal component is also apparent in the spectrum of the background region. This is a strong hint that Westerlund 1 and close regions around (within 30') it hosts relativistic electrons able to radiate non-thermal high energy photons. Detailed investigations of regions further away from Westerlund 1 are necessary to see if there are still non-thermal components maybe even located around γ-ray emission regions.

A modelling of the X-ray and γ-ray spectra with electrons of the same population was not possible due to missing X-ray observations around the γ-ray emission regions.

More and deeper observations of the whole Westerlund 1 region (HESS J1646-458) in several wavelength bands including γ-rays, X-rays and radio might reveal more structures with higher statistics. New instruments like CTA in γ-ray energies and eROSITA in X-rays with better resolutions and including other experiments like *Fermi* or *Chandra* in the analysis might shed light on the origin of these diffuse emissions.

Appendix

Sliced counts cube

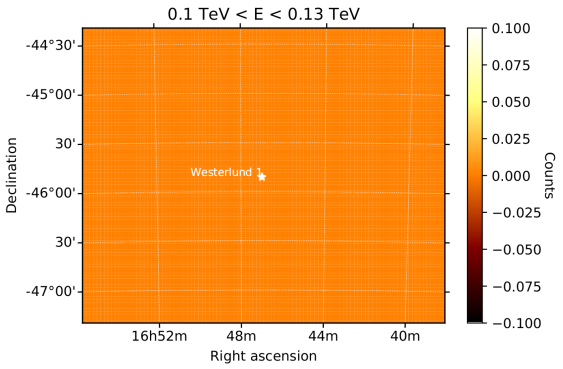

(a) Sky map in the energy bin $0.1 - 0.13$ TeV.

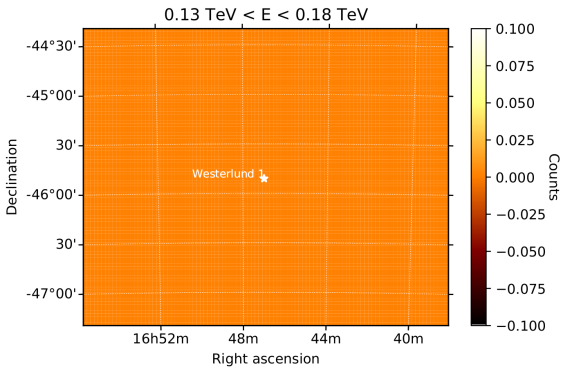

(b) Sky map in the energy bin $0.13 - 0.18$ TeV.

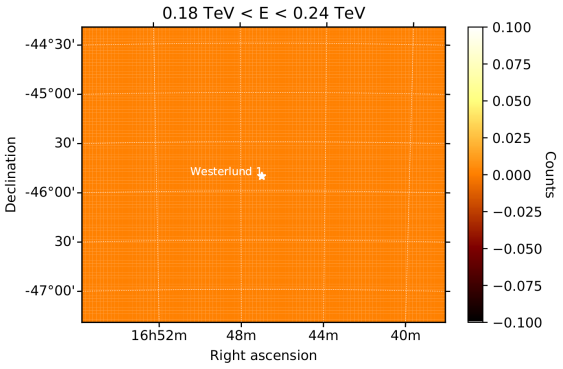

(c) Sky map in the energy bin $0.18 - 0.24$ TeV.

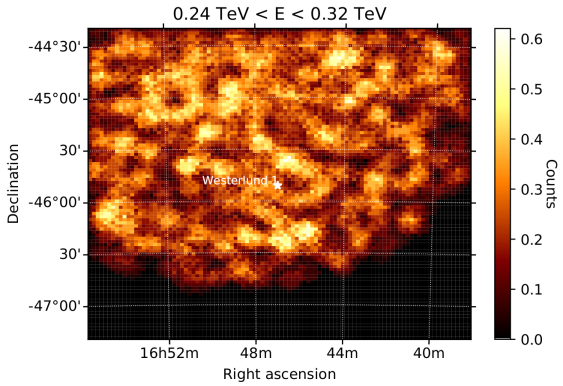

(d) Sky map in the energy bin $0.24 - 0.32$ TeV.

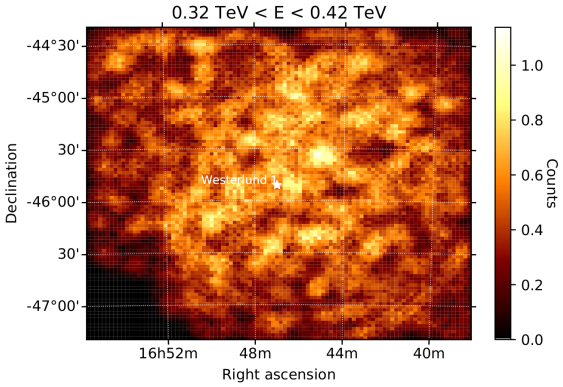

(e) Sky map in the energy bin $0.32 - 42$ TeV.

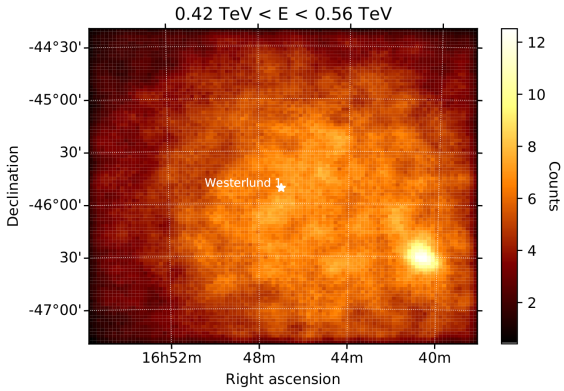

(f) Sky map in the energy bin $0.42 - 56$ TeV.

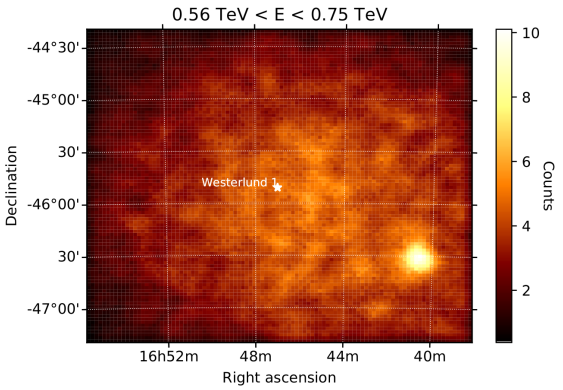

(g) Sky map in the energy bin $0.56 - 0.75$ TeV.

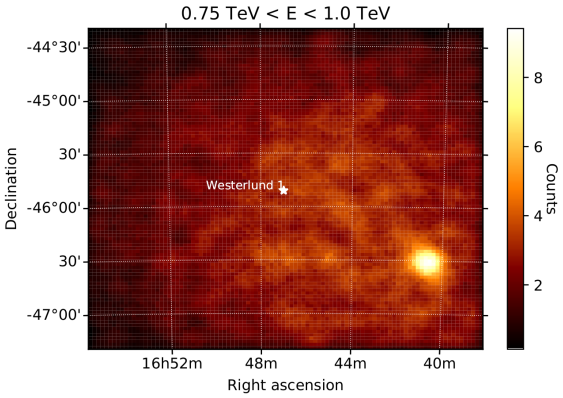

(h) Sky map in the energy bin $0.75 - 1$ TeV.

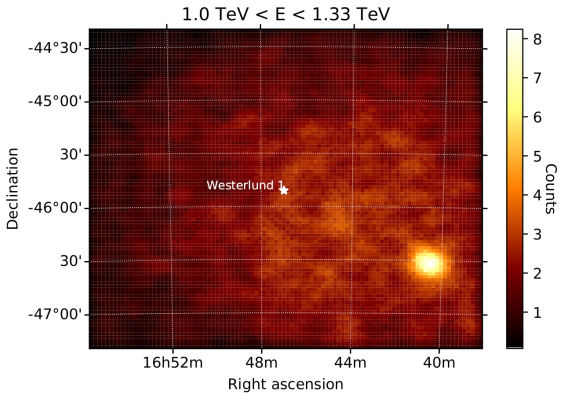

(i) Sky map in the energy bin $1 - 1.33$ TeV.

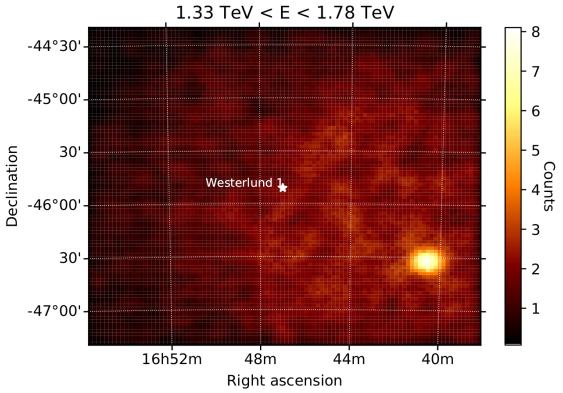

(j) Sky map in the energy bin $1.33 - 1.78$ TeV.

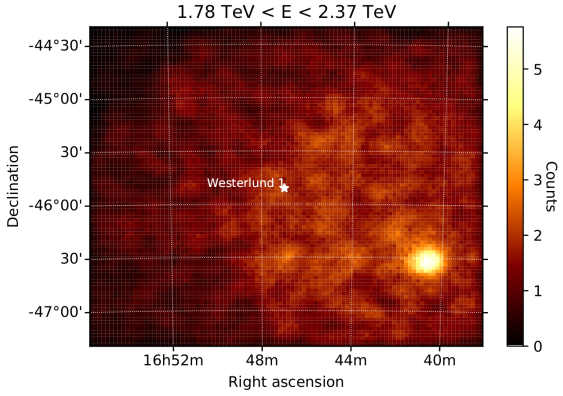

(k) Sky map in the energy bin $1.78 - 2.37$ TeV.

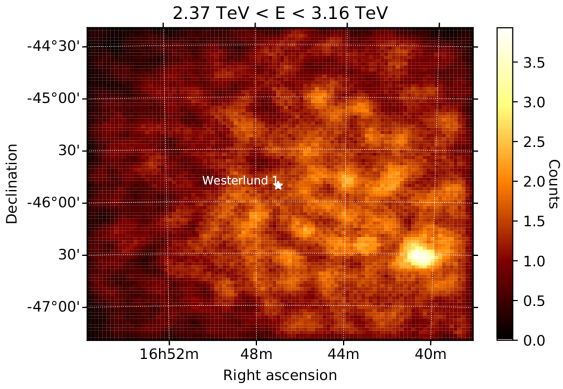

(l) Sky map in the energy bin $2.37 - 3.16$ TeV.

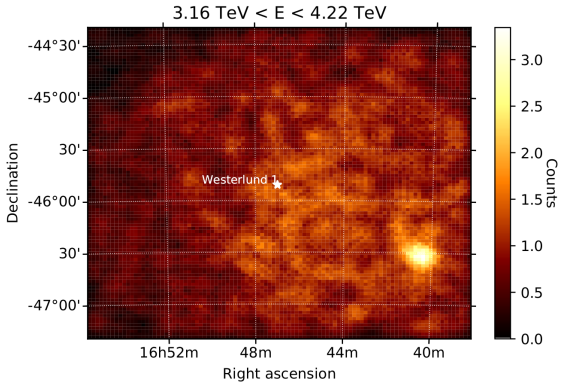

(m) Sky map in the energy bin $3.16 - 4.22$ TeV.

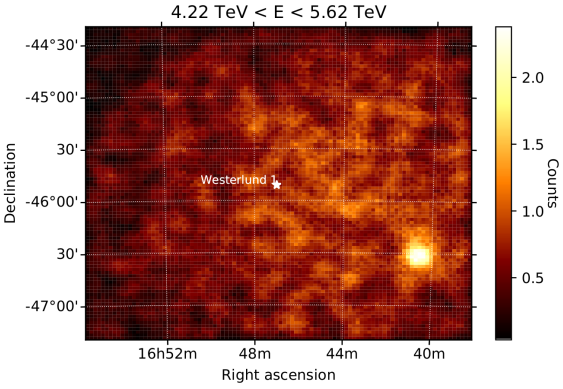

(n) Sky map in the energy bin $4.22 - 5.62$ TeV.

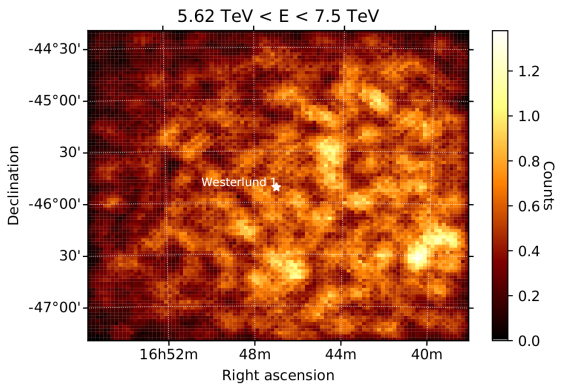

(o) Sky map in the energy bin $5.62 - 7.5\,\mathrm{TeV}$.

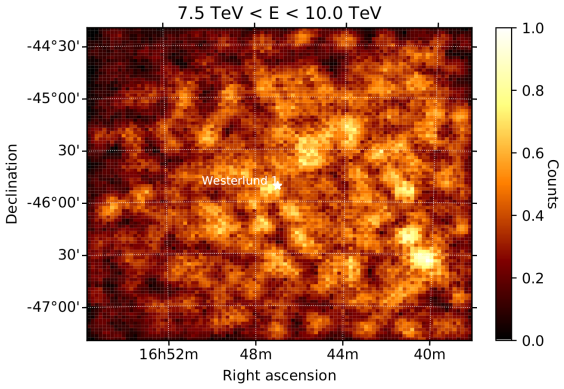

(p) Sky map in the energy bin $7.5 - 10\,\mathrm{TeV}$.

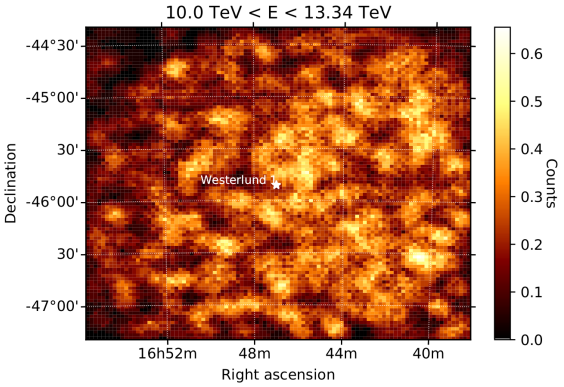

(q) Sky map in the energy bin $10 - 13.34\,\mathrm{TeV}$.

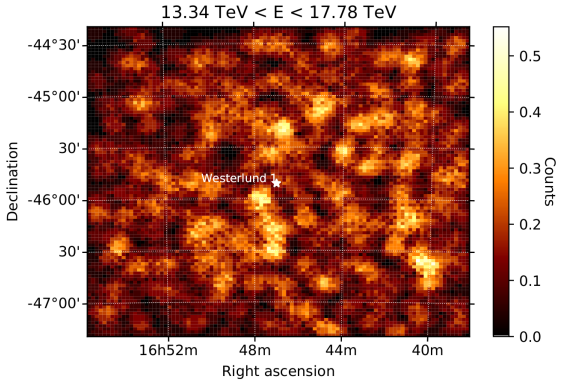

(r) Sky map in the energy bin $13.34 - 17.78\,\mathrm{TeV}$.

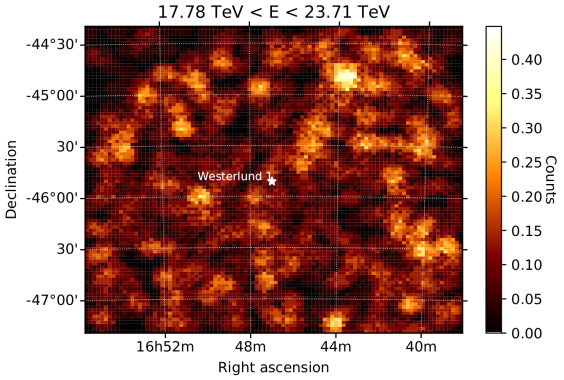

(s) Sky map in the energy bin $17.78 - 23.71\,\mathrm{TeV}$.

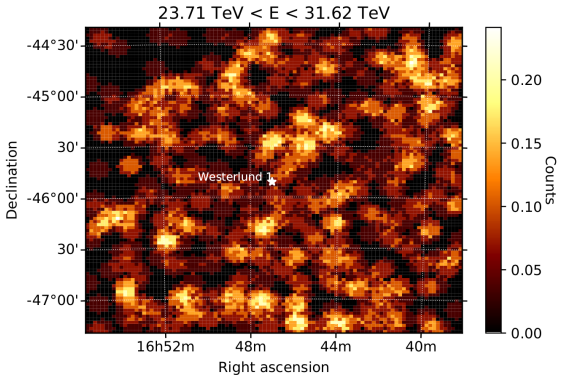

(t) Sky map in the energy bin $23.71 - 31.62\,\mathrm{TeV}$.

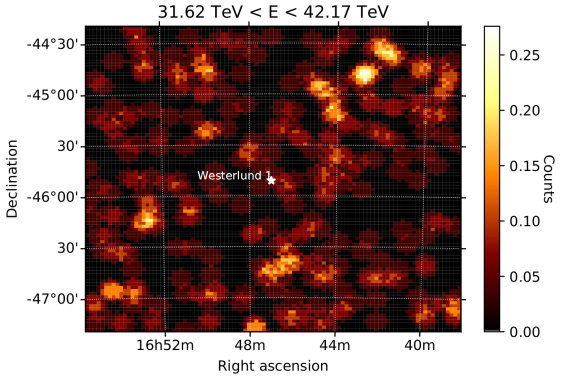

(u) Sky map in the energy bin $31.62 - 42.17\,\mathrm{TeV}$.

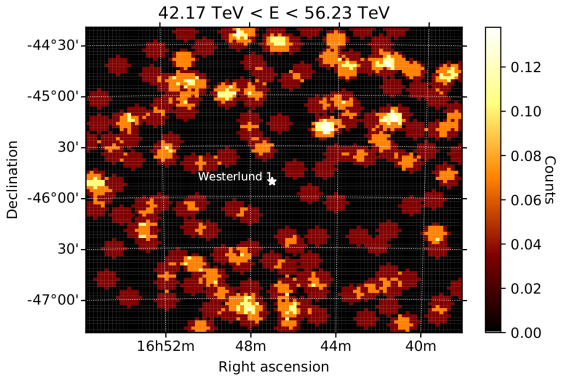

(v) Sky map in the energy bin $42.17 - 56.23\,\mathrm{TeV}$.

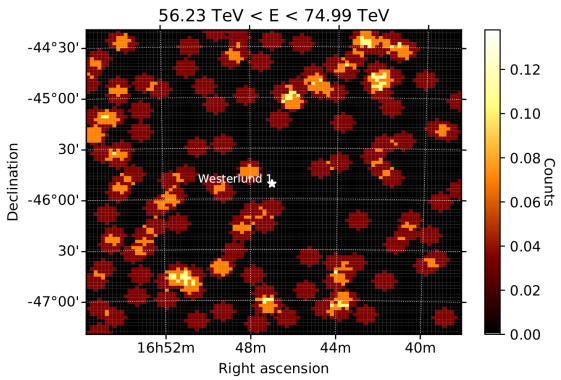

(w) Sky map in the energy bin $56.23 - 74.99\,\mathrm{TeV}$.

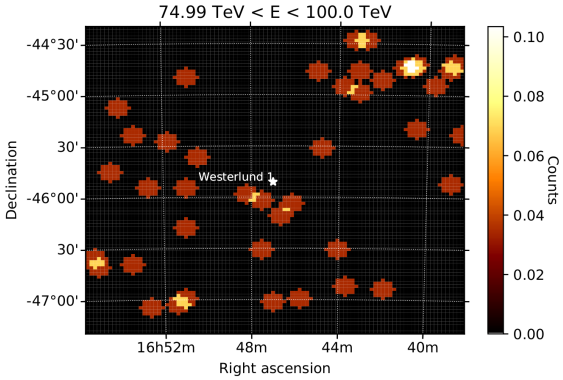

(x) Sky map in the energy bin $74.99 - 100.0\,\mathrm{TeV}$.

Figure 56: Sky map sliced in 24 energy bins.

Table for Model II

Model	Component	Start	Fit	Publication
II	R.A. (°)	250.165	$250.163 \pm 4.039 \cdot 10^{-3}$	250.171
	Dec (°)	−46.541	$-46.544 \pm 2.923 \cdot 10^{-3}$	−46.542
	σ (°)	0.049	$0.046 \pm 2.573 \cdot 10^{-3}$	0.072
	ϕ_0 ($\mathrm{cm^{-2}s^{-1}TeV^{-1}}$)	$5.542 \cdot 10^{-12}$	$5.389 \cdot 10^{-12} \pm 3.866 \cdot 10^{-13}$	$3.3 \cdot 10^{-12}$
	γ	−1.442	-1.430 ± 0.112	2.11
	$\phi_{0,\mathrm{BKG}}$ ($\mathrm{cm^{-2}s^{-1}TeV^{-1}}$)	1.029	$1.029 \pm 2.412 \cdot 10^{-3}$	
	γ_{BKG}	0.036	$0.035 \pm 2.489 \cdot 10^{-3}$	

Table 17: Start and fitted parameters for BKG and HESS J1640-465 of Model II.

Profile plot Model III

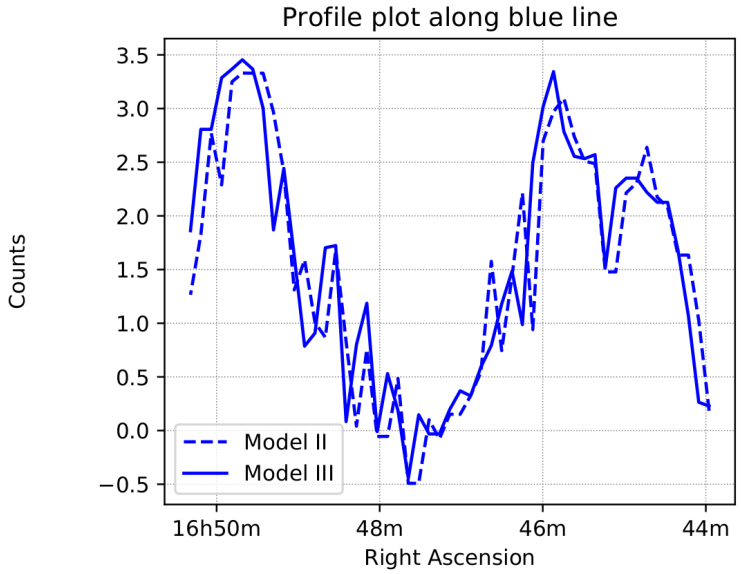

Figure 57: Profile plot extracted along the blue line for Model IIIb compared with Model II showing that there is almost no difference.

Table for Model III

Model	Component	Start	Fit	Publication
IIIa	R.A.$_{1640}$ (°)	250.163	$250.163 \pm 4.033 \cdot 10^{-3}$	250.171
	Dec$_{1640}$ (°)	−46.544	$-46.544 \pm 2.903 \cdot 10^{-3}$	−46.542
	σ_{1640} (°)	0.046	$0.046 \pm 2.568 \cdot 10^{-3}$	0.072
	$\phi_{0,1640}$ (cm^{-2}s^{-1}TeV^{-1})	$5.389 \cdot 10^{-12}$	$5.394 \cdot 10^{-12} \pm 3.814 \cdot 10^{-13}$	$3.3 \cdot 10^{-12}$
	γ_{1640}	−1.430	-1.439 ± 0.111	2.11
	E_{C} (TeV)	2.536	2.575 ± 0.348	6.0
	R.A.$_{1641}$ (°)	250.279	250.277 ± 0.021	250.259
	Dec$_{1641}$ (°)	−46.353	-46.353 ± 0.016	−46.304
	σ_{1641} (°)	0.036	0.031 ± 0.015	0.09
	$\phi_{0,1641}$ (cm^{-2}s^{-1}TeV^{-1})	$2.654 \cdot 10^{-13}$	$2.552 \cdot 10^{-13} \pm 8.131 \cdot 10^{-14}$	$3.91 \cdot 10^{-13}$
	γ_{1641}	−2.071	-2.049 ± 0.161	2.07
IIIb	R.A.$_{1640}$ (°)	250.163	$250.163 \pm 4.030 \cdot 10^{-3}$	250.171
	Dec$_{1640}$ (°)	−46.544	$-46.544 \pm 2.905 \cdot 10^{-3}$	−46.542
	σ_{1640} (°)	0.046	$0.046 \pm 2.569 \cdot 10^{-3}$	0.072
	$\phi_{0,1640}$ (cm^{-2}s^{-1}TeV^{-1})	$5.389 \cdot 10^{-12}$	$5.398 \cdot 10^{-12} \pm 3.845 \cdot 10^{-13}$	$3.3 \cdot 10^{-12}$
	γ_{1640}	−1.430	-1.436 ± 0.111	2.11
	E_{C} (TeV)	2.536	2.555 ± 0.347	6.0
	R.A.$_{1641}$ (°)	250.279	250.276 ± 0.022	250.259
	Dec$_{1641}$ (°)	−46.353	-46.352 ± 0.016	−46.304
	σ_{1641} (°)	0.036	0.031 ± 0.015	0.09
	$\phi_{0,1641}$ (cm^{-2}s^{-1}TeV^{-1})	$2.654 \cdot 10^{-13}$	$2.486 \cdot 10^{-13} \pm 8.051 \cdot 10^{-14}$	$3.91 \cdot 10^{-13}$
	γ_{1641}	−2.071	-2.049 ± 0.165	2.07
	$\phi_{0,\mathrm{BKG}}$ (cm^{-2}s^{-1}TeV^{-1})	1.029	$1.024 \pm 2.745 \cdot 10^{-3}$	
	γ_{BKG}	0.035	$0.033 \pm 2.637 \cdot 10^{-3}$	

Table 18: Start and fitted parameters for the background, HESS J1640-465 and HESS J1641-463 of Model IIIa and IIIb.

Profile plot Model III

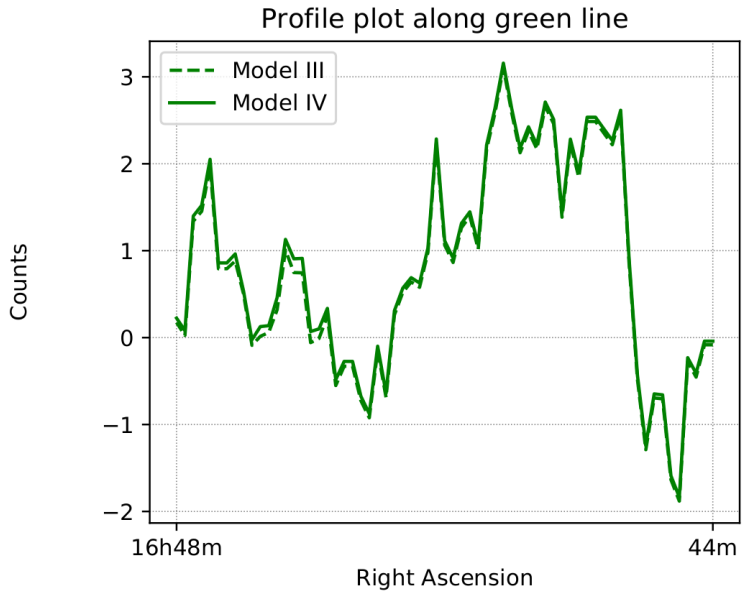

Figure 58: Profile plot extracted along the green line for Model IV compared with Model IIIb showing that there is almost no difference.

Table for Model IV

Model	Component	Start	Fit	Publication
IV	R.A.$_{1640}$ (°)	250.163	$250.163 \pm 4.025 \cdot 10^{-3}$	250.171
	Dec$_{1640}$ (°)	−46.544	$-46.544 \pm 2.910 \cdot 10^{-3}$	−46.542
	σ_{1640} (°)	0.046	$0.046 \pm 2.570 \cdot 10^{-3}$	0.072
	$\phi_{0,1640}$ (cm^{-2}s^{-1}TeV^{-1})	$5.389 \cdot 10^{-12}$	$5.396 \cdot 10^{-12} \pm 3.831 \cdot 10^{-13}$	$3.3 \cdot 10^{-12}$
	γ_{1640}	−1.436	-1.438 ± 0.111	2.11
	E_C (TeV)	2.555	2.565 ± 0.348	6.0
	R.A.$_{1641}$ (°)	250.276	250.277 ± 0.022	250.259
	Dec$_{1641}$ (°)	−46.352	-46.353 ± 0.016	−46.304
	σ_{1641} (°)	0.031	0.032 ± 0.014	0.09
	$\phi_{0,1641}$ (cm^{-2}s^{-1}TeV^{-1})	$2.486 \cdot 10^{-13}$	$2.566 \cdot 10^{-13} \pm 8.153 \cdot 10^{-14}$	$3.91 \cdot 10^{-13}$
	γ_{1641}	−2.049	-2.050 ± 0.162	2.07
	$\phi_{0,\mathrm{BKG}}$ (cm^{-2}s^{-1}TeV^{-1})	1.027	$1.025 \pm 2.527 \cdot 10^{-3}$	
	γ_{BKG}	0.035	$0.034 \pm 2.557 \cdot 10^{-3}$	

Table 19: Start and fitted parameters for the background, HESS J1640-465 and HESS J1641-463 of Model IV.

Profile plot Model V

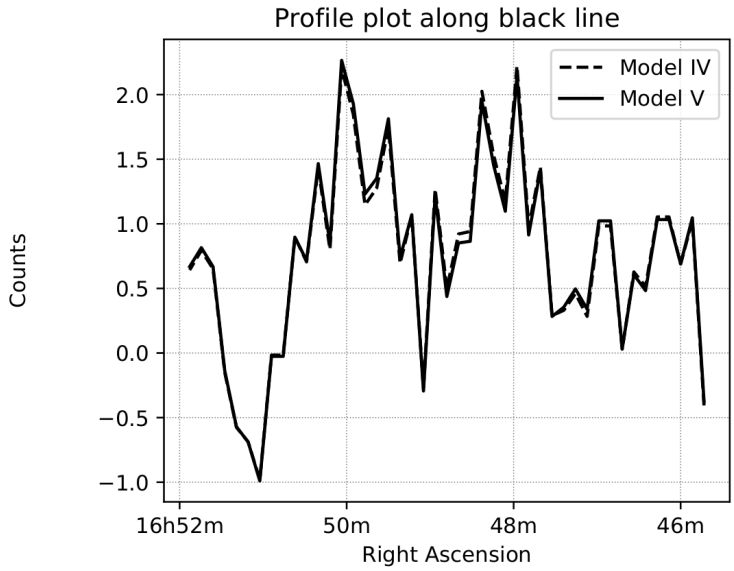

Figure 59: Profile plot extracted along the black line for Model V (b) compared with Model IV showing that there is almost no difference.

Table for Model V

Model	Component	Start	Fit	Publication
Vb	R.A.$_{1640}$ (°)	250.163	$250.163 \pm 4.018 \cdot 10^{-3}$	250.171
	Dec$_{1640}$ (°)	-46.544	$-46.544 \pm 2.903 \cdot 10^{-3}$	-46.542
	σ_{1640} (°)	0.046	$0.046 \pm 2.557 \cdot 10^{-3}$	0.072
	$\phi_{0,1640}$ (cm^{-2}s^{-1}TeV^{-1})	$5.396 \cdot 10^{-12}$	$5.395 \cdot 10^{-12} \pm 3.809 \cdot 10^{-13}$	$3.3 \cdot 10^{-12}$
	γ_{1640}	-1.438	-1.441 ± 0.111	2.11
	E_{C} (TeV)	2.565	2.581 ± 0.350	6.0
	R.A.$_{1641}$ (°)	250.277	250.277 ± 0.022	250.259
	Dec$_{1641}$ (°)	-46.353	-46.353 ± 0.016	-46.304
	σ_{1641} (°)	0.032	0.032 ± 0.014	0.09
	$\phi_{0,1641}$ (cm^{-2}s^{-1}TeV^{-1})	$2.566 \cdot 10^{-13}$	$2.595 \cdot 10^{-13} \pm 8.163 \cdot 10^{-14}$	$3.91 \cdot 10^{-13}$
	γ_{1641}	-2.050	-2.050 ± 0.160	2.07
	R.A.$_{\mathrm{B}}$ (°)	251.819	251.805 ± 0.037	251.682
	Dec$_{\mathrm{B}}$ (°)	-46.513	-46.519 ± 0.027	-46.513
	σ_{B} (°)	0.25	0.080 ± 0.021	0.25
	$\phi_{0,\mathrm{B}}$ (cm^{-2}s^{-1}TeV^{-1})	$2.0 \cdot 10^{-12}$	$4.638 \cdot 10^{-13} \pm 1.236 \cdot 10^{-13}$	$1.4 \cdot 10^{-12}$
	γ_{B}	-2.0	-2.182 ± 0.166	2.29
	R.A.$_{\mathrm{C}}$ (°)	252.443	252.410 ± 0.065	-
	Dec$_{\mathrm{C}}$ (°)	-46.155	-46.169 ± 0.045	-
	σ_{C} (°)	0.2	0.139 ± 0.035	-
	$\phi_{0,\mathrm{C}}$ (cm^{-2}s^{-1}TeV^{-1})	$2.0 \cdot 10^{-12}$	$5.906 \cdot 10^{-13} \pm 1.992 \cdot 10^{-13}$	-
	γ_{C}	-2.0	-2.120 ± 0.182	2.07
	$\phi_{0,\mathrm{BKG}}$ (cm^{-2}s^{-1}TeV^{-1})	1.025	$1.023 \pm 2.585 \cdot 10^{-3}$	
	γ_{BKG}	0.034	$0.033 \pm 2.591 \cdot 10^{-3}$	

Table 20: Start and fitted parameters for the background, HESS J1640-465 and HESS J1641-463 B and C of Model Vb.

Images for a comparison of Model 0 and Model Vb

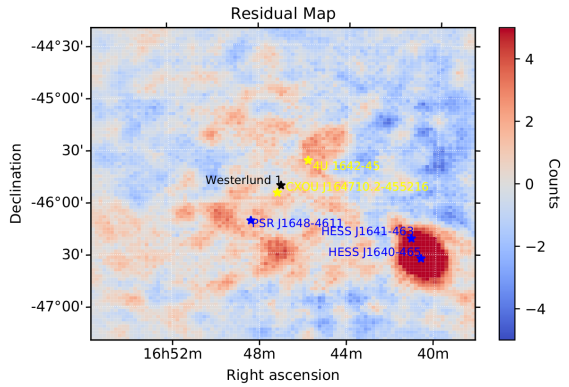

(a) Residual map of Model 0 in which only the background is taken into account.

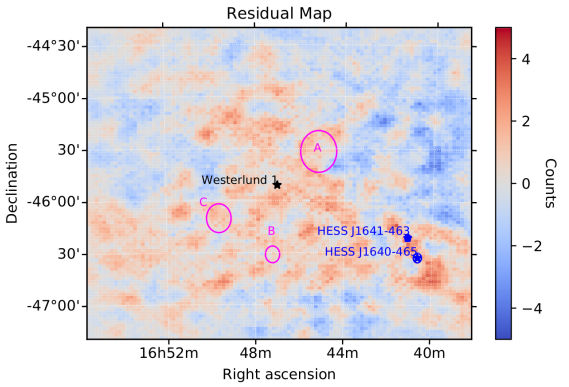

(b) Residual map of Model Vb in which HESS J1640-465, HESS J1641-463, A, B and C are modeled.

(c) Profile extracted along the green line for Model 0 in comparison to Model Vb.

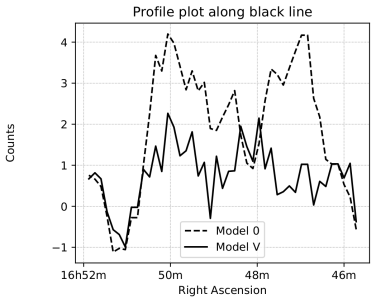

(d) Profile extracted along the black line for Model 0 in comparision to Model Vb.

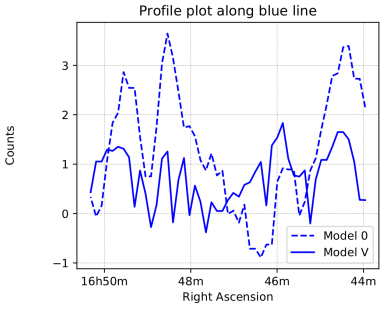

(e) Profile extracted along the blue line for Model 0 in comparision to Model Vb.

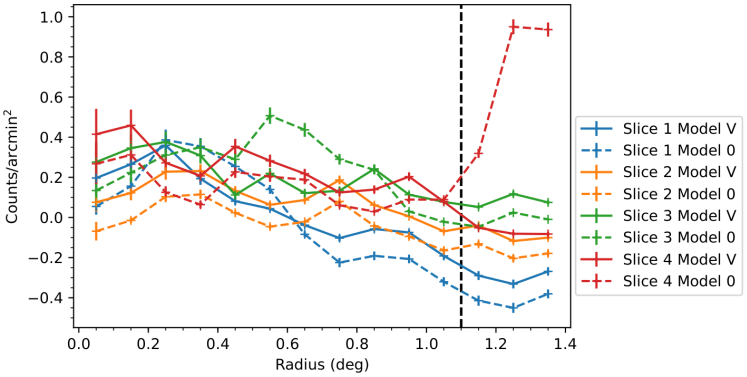

(f) Radial profile plots for Model 0 in comparison to Model Vb.

Figure 60: Residual map, profile and radial profile plots of the final model Model Vb in comparison to Model 0 (background only).

Table Model VI

Model	Component	Start	Fit	Publication
VI	R.A.$_{1640}$ (°)	250.163	$250.163 \pm 4.023 \cdot 10^{-3}$	250.171
	Dec$_{1640}$ (°)	-46.544	$-46.544 \pm 2.907 \cdot 10^{-3}$	-46.542
	σ_{1640} (°)	0.046	$0.046 \pm 2.568 \cdot 10^{-3}$	0.072
	$\phi_{0,1640}$ (cm^{-2}s^{-1}TeV^{-1})	$5.395 \cdot 10^{-12}$	$5.396 \cdot 10^{-12} \pm 0.382$	$3.3 \cdot 10^{-12}$
	γ_{1640}	-1.441	-1.440 ± 0.111	2.11
	E_{C} (TeV)	2.581	2.575 ± 0.349	6.0
	R.A.$_{1641}$ (°)	250.277	250.277 ± 0.022	250.259
	Dec$_{1641}$ (°)	-46.353	-46.353 ± 0.016	-46.304
	σ_{1641} (°)	0.032	0.032 ± 0.014	0.09
	$\phi_{0,1641}$ (cm^{-2}s^{-1}TeV^{-1})	$2.595 \cdot 10^{-13}$	$2.585 \cdot 10^{-13} \pm 0.818$	$3.91 \cdot 10^{-13}$
	γ_{1641}	$-.050$	-2.051 ± 0.161	2.07
	R.A.$_{\mathrm{A}}$ (°)	251.290	251.302 ± 0.042	251.370
	Dec$_{\mathrm{A}}$ (°)	-45.528	-45.481 ± 0.029	-45.585
	σ_{A} (°)	0.201	0.167 ± 0.027	0.35
	$\phi_{0,\mathrm{A}}$ (cm^{-2}s^{-1}TeV^{-1})	$4.634 \cdot 10^{-13}$	$1.245 \cdot 10^{-12} \pm 0.217 \cdot 10^{-12}$	$9.0 \cdot 10^{-12}$
	γ_{A}	-2.182	-2.130 ± 0.105	2.19
	R.A.$_{\mathrm{B}}$ (°)	251.805	251.806 ± 0.036	251.682
	Dec$_{\mathrm{B}}$ (°)	-46.519	-46.520 ± 0.025	-46.513
	σ_{B} (°)	0.080	0.075 ± 0.018	0.25
	$\phi_{0,\mathrm{B}}$ (cm^{-2}s^{-1}TeV^{-1})	$4.634 \cdot 10^{-12}$	$1.245 \cdot 10^{-12} \pm 0.217 \cdot 10^{-12}$	$9.0 \cdot 10^{-12}$
	γ_{B}	-2.182	-2.130 ± 0.105	2.19
	R.A.$_{\mathrm{C}}$ (°)	252.410	252.410 ± 0.065	-
	Dec$_{\mathrm{C}}$ (°)	-46.169	-46.169 ± 0.045	-
	σ_{C} (°)	0.139	0.139 ± 0.035	-
	$\phi_{0,\mathrm{C}}$ (cm^{-2}s^{-1}TeV^{-1})	$4.634 \cdot 10^{-13}$	$1.245 \cdot 10^{-12} \pm 0.217 \cdot 10^{-12}$	-
	γ_{C}	2.182	2.130 ± 0.105	-
	$\phi_{0,\mathrm{BKG}}$ (cm^{-2}s^{-1}TeV^{-1})	1.023	$1.024 \pm 2.538 \cdot 10^{-3}$	
	γ_{BKG}	0.033	$0.034 \pm 2.569 \cdot 10^{-3}$	

Table 21: Start and fitted parameters for the background, HESS J1640-465 and HESS J1641-463 A, B and C of Model VI.

Butterfly diagrams for Model VI

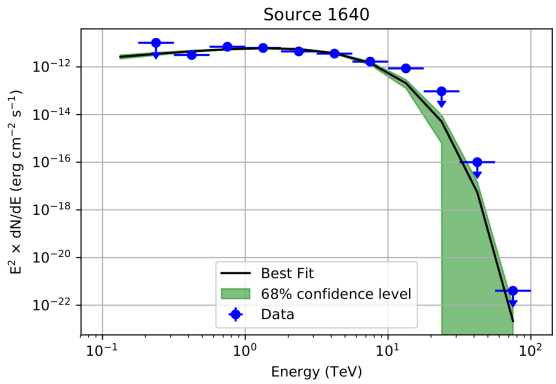

(a) Butterfly spectrum of source HESS J1640-465 for the Model VI.

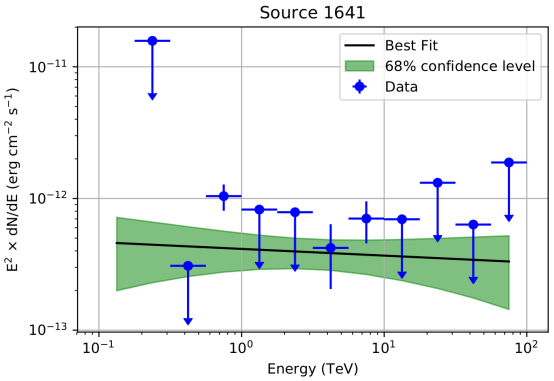

(b) Butterfly spectrum of source HESS J1641-463 for the Model VI.

Figure 61: Butterfly spectra for the sources HESS J1640-465 and HESS J1641-463 of Model VI.

Error estimation of the luminosity

$$E = \int_{\text{emin}}^{\text{emax}} S(E) E \mathrm{d}E = k_0 \left(\frac{E}{E_0}\right)^{\gamma} E \mathrm{d}E = \frac{k_0}{\gamma + 2} \left(\frac{E}{E_0}\right)^{\gamma} E^2 \Bigg|_{\text{emin}}^{\text{emax}}$$

$$\Delta E = \sqrt{\left(\frac{\partial E}{\partial k_0} \Delta k_0\right)^2 + \left(\frac{\partial E}{\partial \gamma} \Delta \gamma\right)^2}$$

$$\frac{\partial E}{\partial k_0} = \frac{1}{\gamma + 2} \left(\frac{E}{E_0}\right)^{\gamma} E^2$$

$$\frac{\partial E}{\partial \gamma} = \left(-\frac{k_0}{E_0^{\gamma}(\gamma + 2)^2} - k_0 \log(E_0) \frac{1}{E_0^{\gamma}(\gamma + 2)} + \frac{k_0 \log(E)}{E_0^{\gamma}(\gamma + 2)}\right) E^{\gamma + 2}$$

Diagnostic plots

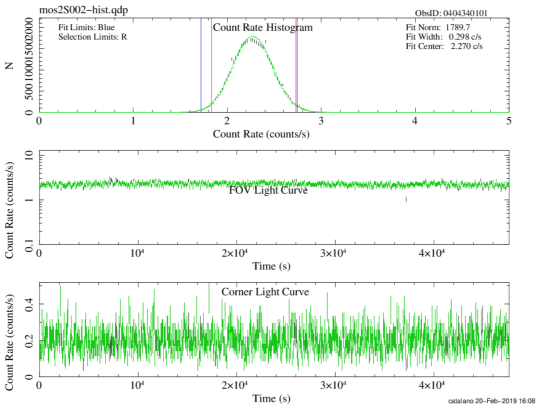

(a) Diagnostic plot for MOS2 of the Westerlund 1 observation.

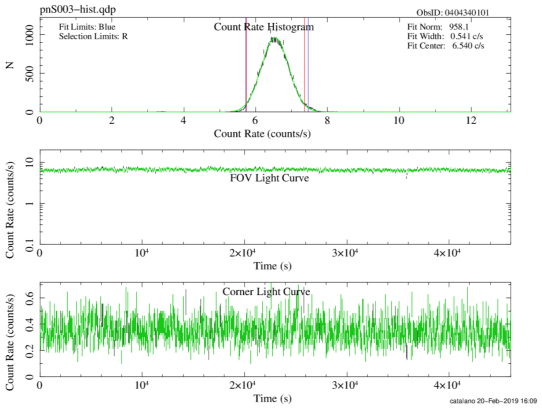

(b) Diagnostic plot for PN of the Westerlund 1 observation.

Figure 62: Diagnostic plots for MOS2 and PN of the Westerlund 1 observation.

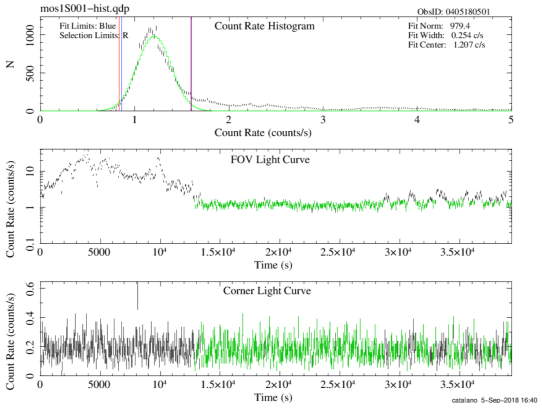

(a) Diagnostic plot for source 2c.

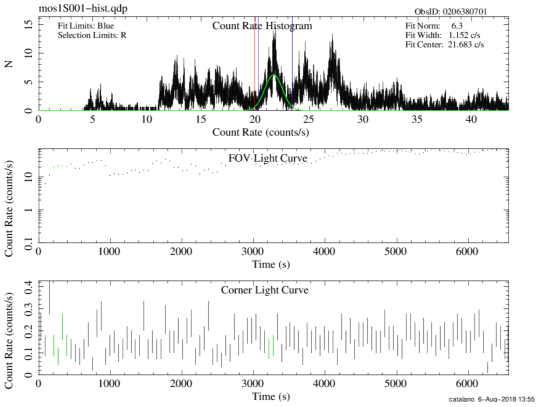

(b) Diagnostic plot for source 5b.

Figure 63: Diagnostic plots for the excluded observations 2c and 5b.

Stray light images

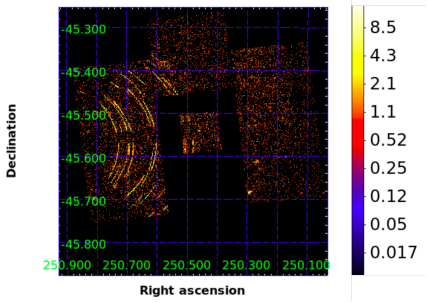

(a) Event image for source 2a.

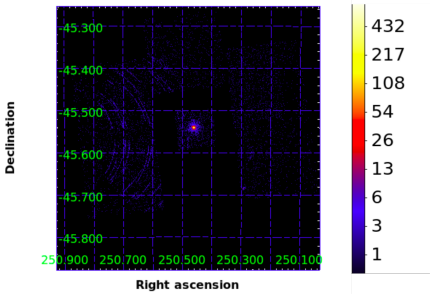

(b) Event image for source 2b.

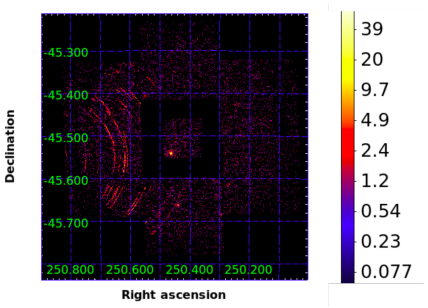

(c) Event image for source 3.

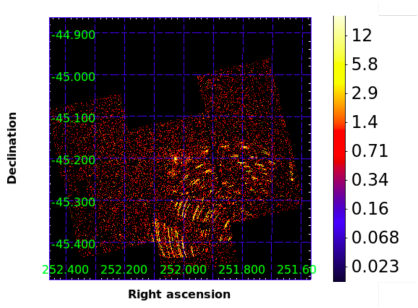

(d) Event image for source 4c.

Figure 64: Event images of the excluded observations 2a, 2b, 3 and 4c due to stray light. Shown for the MOS1 detector only because all of the images look basically the same.

Background images

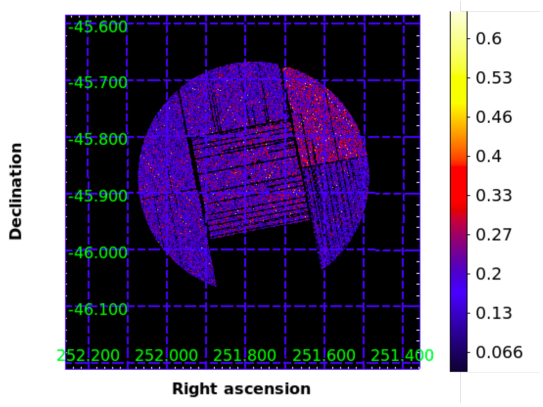

(a) Model particle background image in sky coordinates of MOS1.

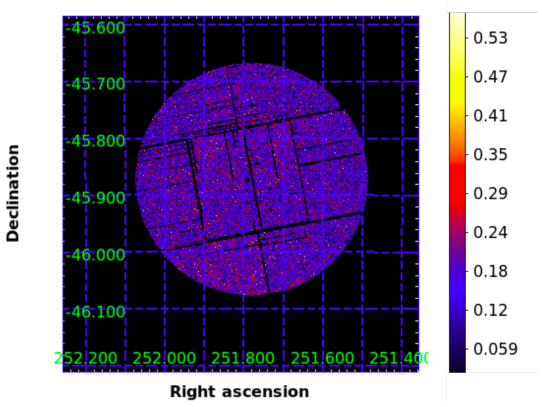

(b) Model particle background image in sky coordinates of MOS2.

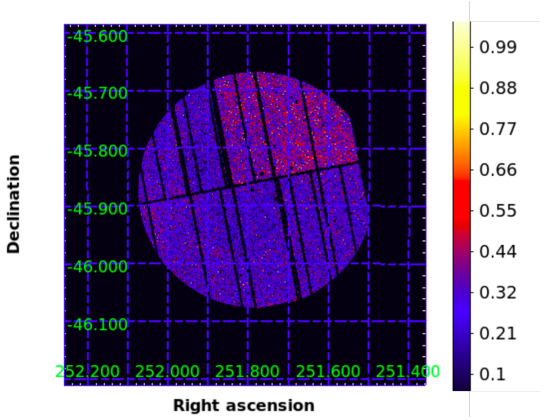

(c) Model particle background image in sky coordinates of PN.

Figure 65: Model particle background images of all detectors.

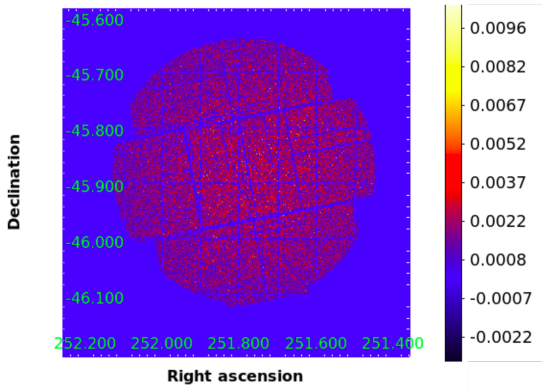

(a) Soft proton background image in sky coordinates of MOS1.

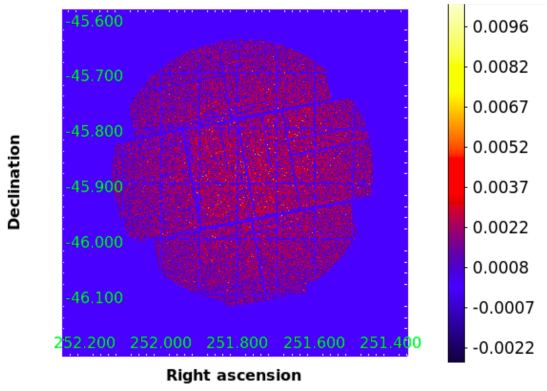

(b) Soft proton background image in sky coordinates of MOS2.

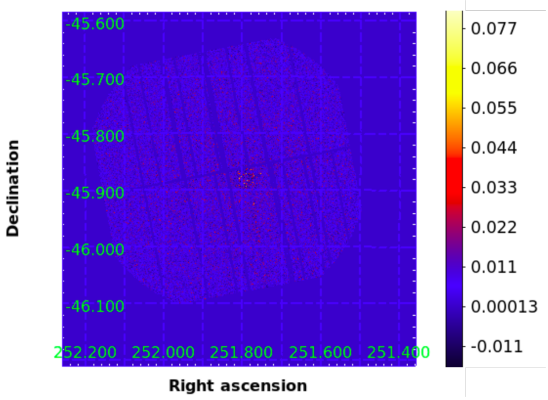

(c) Soft proton background image in sky coordinates of PN.

Figure 66: Soft protron background images of all detectors.

Hardness ratio plots

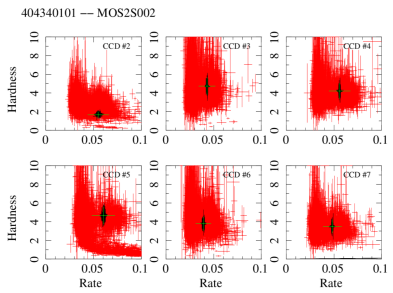

(a) Hardness ratio plot for MOS2 of the Westerlund 1 observation 1a.

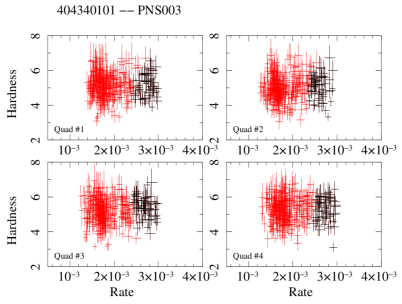

(b) Hardness ratio plot for PN of the Westerlund 1 observation 1a.

Figure 67: Hardness ratio plots for MOS2 and PN of the Westerlund 1 observation 1a.

Other X-ray observations

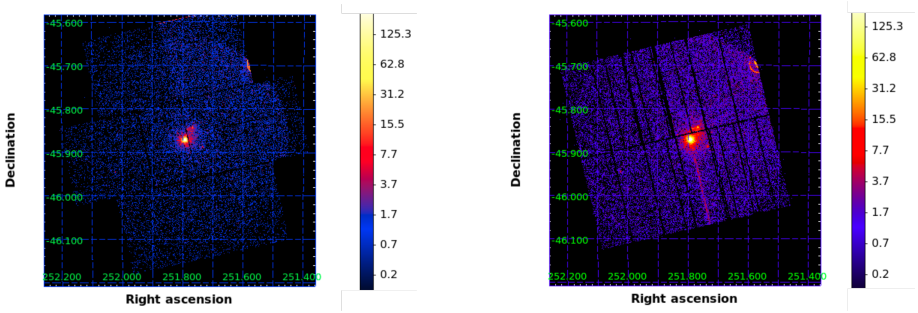

(a) Sky image of the other Westerlund 1 observation 1b for MOS2.

(b) Sky image of the other Westerlund 1 observation 1b for PN.

Figure 68: Sky images of the other Westerlund 1 observation for other detectors.

apec Model

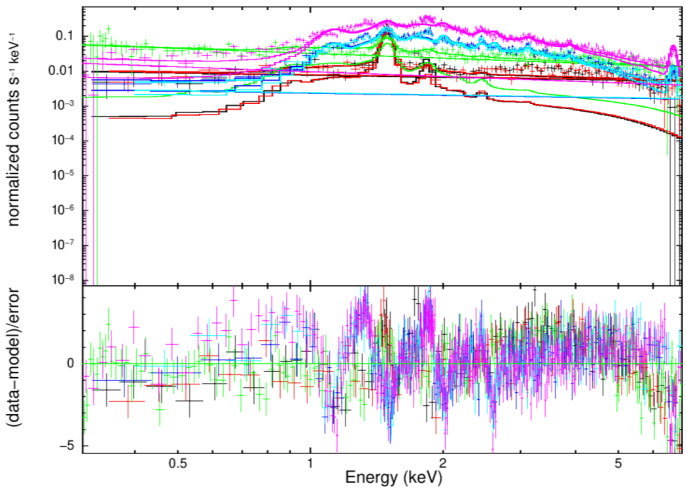

Figure 69: Spectrum modeled with one thermal plasma of temperature kT. The red, black and green lines indicate the MOS1/2 and PN detector for the background region and the blue, cyan and magenta lines display the MOS1/2 and PN detector of the source region. The lower plot shows the deviations from the data.

Model	Parameter	Value	χ^2/ndf
apec	N_H (10^{22}cm^{-2})	$1.76 \pm 2.61 \cdot 10^{-2}$	
	kT (keV)	$1.96 \pm 3.54 \cdot 10^{-2}$	
	A (10^{-4} arcmin^{-2})	$3.76 \pm 6.64 \cdot 10^{-2}$	2.35

Table 22: Fitted parameters of the apec model.

apec+apec Model

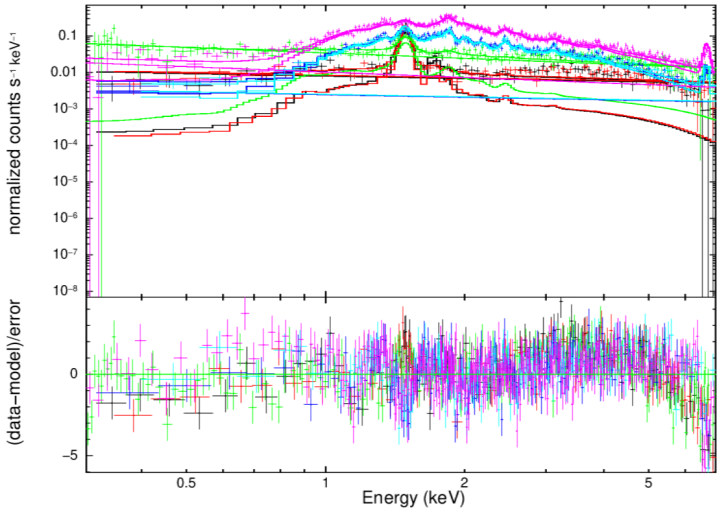

Figure 70: Spectrum modeled with two thermal plasmas of temperatures T_1 and T_2.

Model	Parameter	Value	χ^2/ndf
apec+apec	N_H (10^{22}cm^{-2})	$2.04 \pm 2.51 \cdot 10^{-2}$	
	kT_1 (keV)	$2.87 \pm 9.09 \cdot 10^{-2}$	
	A_1 (10^{-4} arcmin^{-2})	$2.44 \pm 8.85 \cdot 10^{-2}$	
	kT_2 (keV)	$0.79 \pm 2.78 \cdot 10^{-2}$	
	A_2 (10^{-4} arcmin^{-2})	3.36 ± 0.20	1.90

Table 23: Fitted parameters of the apec+apec model.

`apec+pow` Model

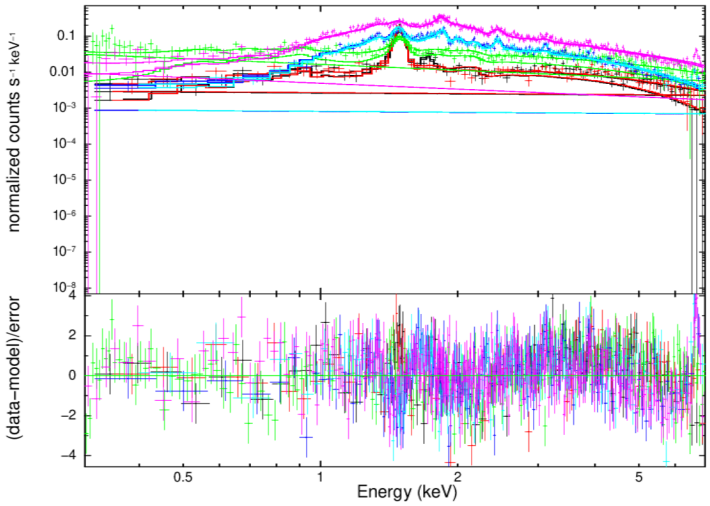

Figure 71: Spectrum modeled with one thermal plasma and an additional power law component also apparent in the background.

Model	Parameter	Value	χ^2/ndf
`apec+pow`	N_H (10^{22}cm^{-2})	$2.11 \pm 2.42 \cdot 10^{-2}$	
	kT (keV)	$0.84 \pm 2.23 \cdot 10^{-2}$	
	A (10^{-4} arcmin^{-2})	4.10 ± 0.21	
	Γ	$1.93 \pm 4.91 \cdot 10^{-2}$	
	A_{PL} (10^{-5} erg s^{-1} cm^{-2})	7.46 ± 0.56	
	A_{BKG} (10^{-5} erg s^{-1} cm^{-2})	$1.19 \pm 7.67 \cdot 10^{-2}$	1.45

Table 24: Fitted parameters of the `apec+pow` model including a power law component apparend in the background.

`nei` Model

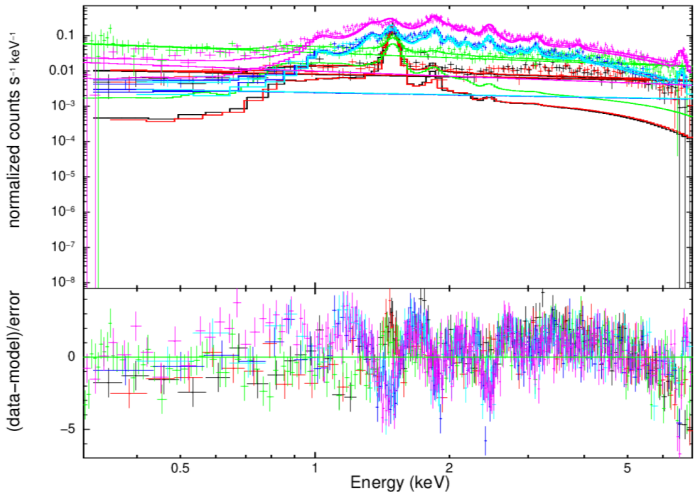

Figure 72: Spectrum modeled with one thermal plasma in non-equilibrium.

Model	Parameter	Value	χ^2/ndf
`nei`	N_H (10^{22}cm^{-2})	$2.23 \pm 2.06 \cdot 10^{-2}$	
	kT (keV)	4.34 ± 0.14	
	τ (10^{10} s cm^{-3})	4.44 ± 0.15	
	A (10^{-4} arcmin^{-2})	$2.09 \pm 3.81 \cdot 10^{-2}$	2.51

Table 25: Fitted parameters of the `nei` model.

`nei+nei` Model

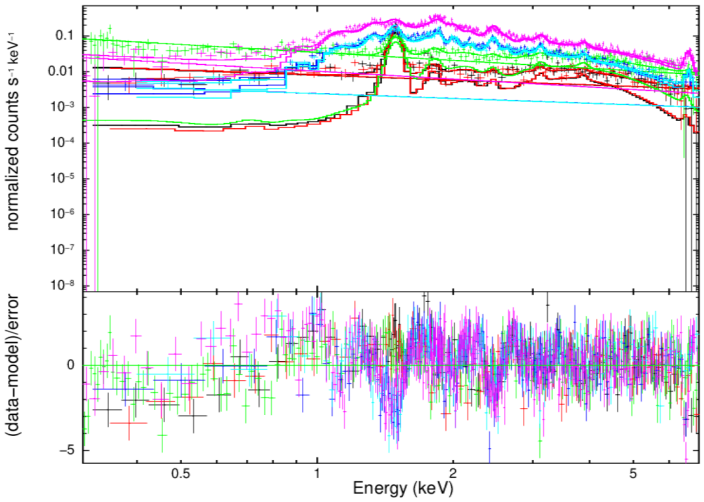

Figure 73: Spectrum modeled with two thermal plasmas in non-equilibrium.

Model	Parameter	Value	χ^2/ndf
`nei+nei`	N_H (10^{22}cm^{-2})	$3.06 \pm 6.99 \cdot 10^{-2}$	
	kT_1 (keV)	3.03 ± 0.12	
	τ_1 (10^{10} s cm^{-3})	8.22 ± 0.56	
	A_1 (10^{-4} arcmin^{-2})	2.90 ± 0.12	
	kT_2 (keV)	$0.18 \pm 5.27 \cdot 10^{-3}$	
	τ_2 (10^{10} s cm^{-3})	1.11 ± 0.13	
	A_2 (arcmin^{-2})	0.38 ± 0.13	1.81

Table 26: Fitted parameters of the `nei+nei` model.

`nei+pow` Model

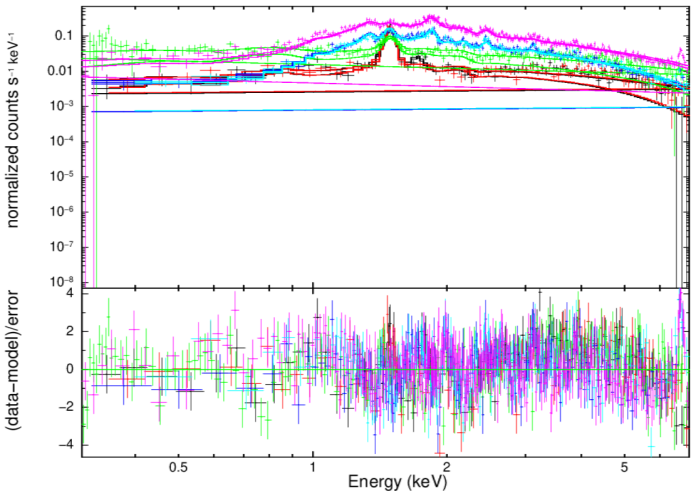

Figure 74: Spectrum modeled with one thermal plasma in non-equilibrium and an additional power law component also apparent in the background.

Model	Parameter	Value	χ^2/ndf
`nei+pow`	N_H (10^{22}cm^{-2})	$2.10 \pm 3.75 \cdot 10^{-2}$	
	kT (keV)	1.12 ± 0.18	
	τ (10^{10} s cm^{-3})	6.74 ± 2.98	
	A (10^{-4} arcmin^{-2})	1.91 ± 0.34	
	Γ	$2.25 \pm 3.71 \cdot 10^{-2}$	
	A_{PL} (10^{-5} erg s^{-1} cm^{-2})	7.46 ± 0.56	
	A_{BKG} (10^{-5} erg s^{-1} cm^{-2})	1.35 ± 0.13	1.52

Table 27: Fitted parameters of the `nei+pow` model.

`nei+nei+pow` Model

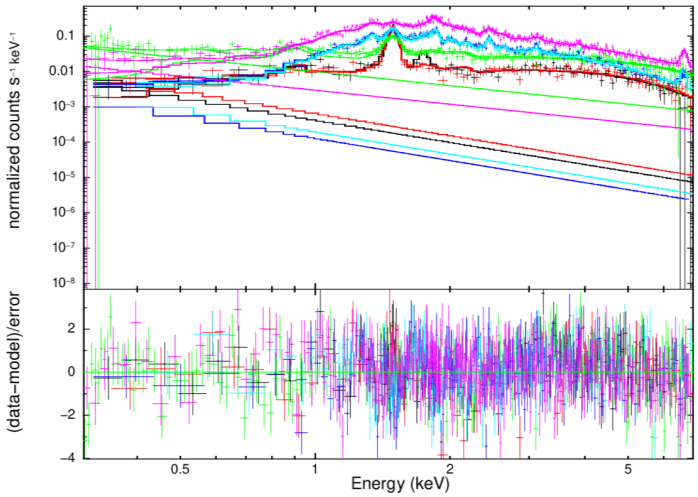

Figure 75: Spectrum modeled with two thermal plasmas in non-equilibrium and an additional power law component also apparent in the backgound.

Model	Parameter	Value	χ^2/ndf
`nei+nei+pow`	N_H (10^{22}cm^{-2})	2.09 ± 4.71	
	kT_1 (keV)	$2.04 \pm 7.68 \cdot 10^{-2}$	
	τ_1 (10^{12} s cm^{-3})	$4.42 \pm -$	
	A_1 (10^{-4} arcmin^{-2})	2.29 ± 0.12	
	kT_2 (keV)	1.46 ± 0.36	
	τ_2 (10^{10} s cm^{-3})	3.27 ± 0.82	
	A_2 (10^{-4} arcmin^{-2})	1.41 ± 0.28	
	Γ	$1.21 \pm 5.28 \cdot 10^{-2}$	
	A_{PL} (10^{-5} erg s^{-1} cm^{-2})	1.25 ± 0.20	
	A_{BKG} (10^{-6} erg s^{-1} cm^{-2})	7.66 ± 0.57	1.15

Table 28: Fitted parameters of the `nei+nei+pow` model.

`nei+apec+pow` Model

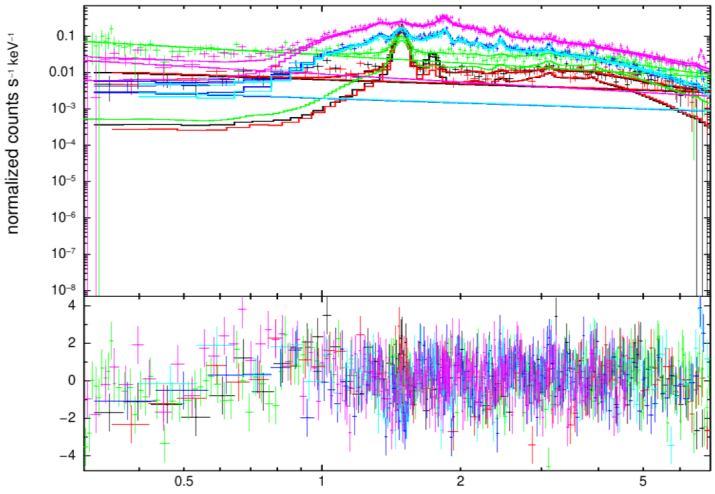

Figure 76: Spectrum modeled with two thermal plasmas one in non-equilibrium and an additional power law component also apparent in the backgound.

Model	Parameter	Value	χ^2/ndf
`nei+apec+pow`	N_H (10^{22}cm^{-2})	$1.94 \pm 3.07 \cdot 10^{-2}$	
	kT_1 (keV)	3.49 ± 1.24	
	τ_1 (10^{12} s cm^{-3})	1.41 ± 0.27	
	A_1 (10^{-5} arcmin^{-2})	4.17 ± 0.80	
	kT_2 (keV)	$0.90 \pm 3.99 \cdot 10^{-2}$	
	A_2 (10^{-4} arcmin^{-2})	1.72 ± 0.30	
	Γ	$2.29 \pm 8.39 \cdot 10^{-2}$	
	A_{PL} (10^{-4} erg s^{-1} cm^{-2})	$1.04 \pm 9.93 \cdot 10^{-2}$	
	A_{BKG} (10^{-6} erg s^{-1} cm^{-2})	7.98 ± 0.92	1.35

Table 29: Fitted parameters of the `nei+apec+pow` model.

`vnei+apec+pow` Model

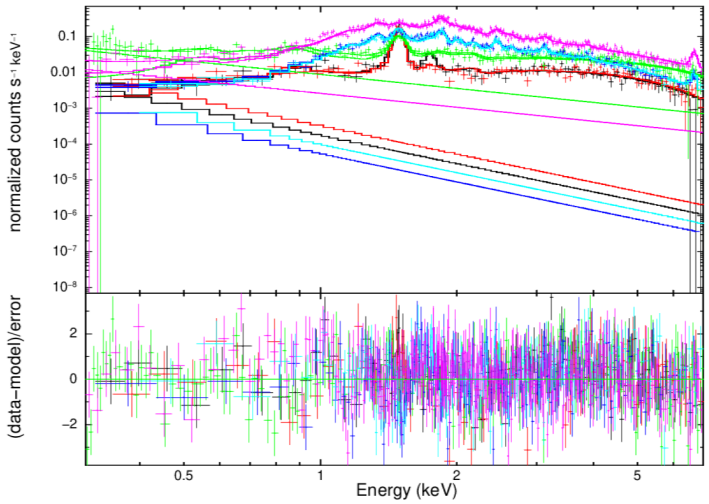

Figure 77: Spectrum modeled with two thermal plasmas one in non-equilibrium with some abundances free and an additional power law component also apparent in the background.

Model	Parameter	Value	χ^2/ndf
`vnei+apec+pow`	N_H (10^{22}cm^{-2})	$2.44 \pm 9.44 \cdot 10^{-2}$	
	kT_1 (keV)	0.96 ± 0.18	
	Si (Si$_\odot$)	$0.83 \pm 7.12 \cdot 10^{-2}$	
	Ar (Ar$_\odot$)	2.00 ± 0.81	
	Fe (Fe$_\odot$)	1.89 ± 0.28	
	τ_1 (10^{10} s cm^{-3})	6.70 ± 2.89	
	A_1 (10^{-4} arcmin^{-2})	2.97 ± 0.94	
	kT_2 (keV)	$1.90 \pm 7.09 \cdot 10^{-2}$	
	A_2 (10^{-4} arcmin^{-2})	2.47 ± 0.11	
	Γ	$1.31 \pm 6.03 \cdot 10^{-2}$	
	A_{PL} (10^{-5} erg s^{-1} cm^{-2})	1.66 ± 0.23	
	A_{BKG} (10^{-6} erg s^{-1} cm^{-2})	9.13 ± 0.81	1.13

Table 30: Fitted parameters of the `vnei+apec+pow` model.

`vnei+nei+pow` Model

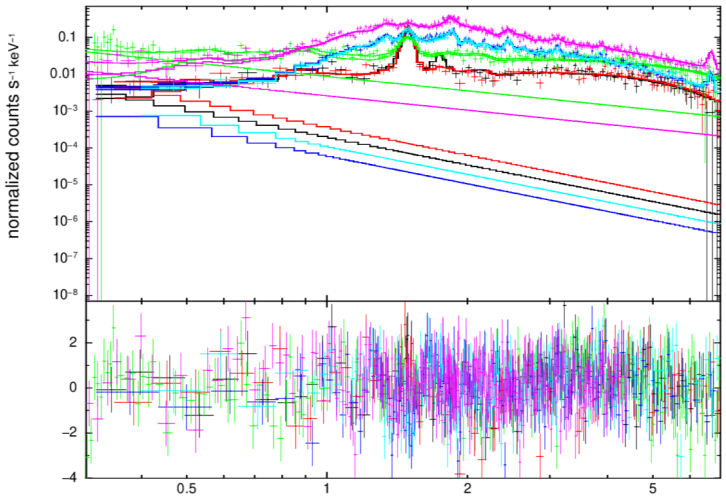

Figure 78: Spectrum modeled with two thermal plasmas in non-equilibrium with some abundances free for one of the `nei` models and an additional power law component also apparent in the background.

Model	Parameter	Value	χ^2/ndf
`vnei+nei+pow`	N_H (10^{22}cm^{-2})	$2.16 \pm 5.63 \cdot 10^{-2}$	
	kT_1 (keV)	$1.98 \pm 7.14 \cdot 10^{-2}$	
	Ar ($Ar_\odot$)	1.81 ± 0.30	
	Ca ($Ca_\odot$)	2.10 ± 0.38	
	τ_1 (10^{13} s cm^{-3})	$3.35 \pm -$	
	A_1 (10^{-4} arcmin^{-2})	2.33 ± 0.12	
	kT_2 (keV)	0.97 ± 0.21	
	τ_2 (10^{10} s cm^{-3})	6.15 ± 2.50	
	A_2 (10^{-4} arcmin^{-2})	2.20 ± 0.66	
	Γ	$1.24 \pm 5.41 \cdot 10^{-2}$	
	A_{PL} (10^{-5} erg s^{-1} cm^{-2})	1.45 ± 0.18	
	A_{BKG} (10^{-6} erg s^{-1} cm^{-2})	8.05 ± 0.63	1.14

Table 31: Fitted parameters of the `vnei+nei+pow` model.

References

Aghakhanloo et al. (2019). Inferring the distance to Westerlund 1 from Gaia DR2. *arXiv:1901.06582*.

Aharonian et al. (2006). Observations of the Crab Nebula with H.E.S.S. . *arXiv:astro-ph/0607333*.

An et al. (2012). Spectral and Timing Properties of the Magnetar CXOU J164710.2-455216. *arXiv:1212.0184v1*.

Andrieu et al. (2003). An Introduction of MCMC for Machine Learning. *Machine Learning*, 50:5–43.

Ansoldi et al. (2018). The blazar TXS 0506+056 associated with a high-energy neutrino: insights into extragalactic jets and cosmic ray acceleration. *arXiv:1807.04300*.

Arnaud et al. (03.03.2018). XSPEC - An X-Ray Spectral Fitting Package. `https://heasarc.gsfc.nasa.gov/xanadu/xspec/XspecManual.pdf`.

Berge et al. (2007). Background modelling in very-high-energy γ-ray astronomy. *arXiv:astro-ph/0610959*.

Bernlöhr, K. (25.01.2019). Atmospheric Cherenkov light. `https://www.mpi-hd.mpg.de/hfm/CosmicRay/ChLight/Cherenkov.html`.

Bignami et al. (1990). European Photon Imaging Camera for x-ray astronomy. *Proceeding 34th Annual International Technical Symposium on Optical and Optoelectronic Applied Science and Engineering,*, 1344.

Bonnefoy et al. (2017). Performance of the upgraded H.E.S.S. cameras. *arXiv:1708.04550*.

Boyle, W. S. and Smith, G. E. (1970). Charge coupled semiconductor devices. *The Bell System Technical Journal*, 49:587 – 593.

Brandner et al. (2008). Intermediate to low-mass stellar content of Westerlund 1. *arXiv:0711.1624*.

Cassé, M. and Paul, J. A. (1980). Local Gamma Rays and Cosmic-Ray Acceleration by Supersonic Stellar Winds. *The Astrophysical Journal*, 237:236–243.

Cherenkov Telescope Array Analysis Software Team (10.02.2019). ctools. http://cta.irap.omp.eu/ctools/index.html.

Cherenkov Telescope Array Observatory gGmbH (28.01.2019). A multinational initiative founded on its exceptional scientific potential. https://www.cta-observatory.org/about/.

Clark et al. (2005). On the massive stellar population of the Super Star Cluster Westerlund 1. *arXiv:astro-ph/0504342*.

Conti, P. S. (2005). *Observational tests of the stellar evolution theory*. Kluwer Academic Publishers.

Cowan, G. (1998). *Statistical Data Analysis*. Oxford University Press.

Crowther, P. A. (2007). Physical Properties of Wolf-Rayet Stars. *arXiv: astro-ph/0610356v2*.

Dame et al. (2001). The Milky Way in Molecular Clouds: A New Complete CO Survey. *arXiv:astro-ph/0009217*.

Degrange, B. and Fontaine, G. (2016). Introduction to high-energy gamma-ray astronomy. *arXiv:1604.05488v1*.

Eichler, D. and Usov, V. (1993). Particle Acceleration and Nonthermal Radio Emission in Binaries of Early-type Stars. *The Astrophyisical Journal*, 402:271–279.

ESA (11.05.2018b). The European Photo Imaging Camera (EPIC) onboard XMM-Newton. https://www.cosmos.esa.int/web/xmm-newton/technical-details-epic.

ESA (11.07.2018a). Stellar Processes and Evolution. http://sci.esa.int/education/36828-stellar-processes-and-evolution/?fbodylongid=1742.

European Space Agency (03.03.2019b). XMM-Newton Science Analysis System: User Guide. https://xmm-tools.cosmos.esa.int/external/xmm_user_support/documentation/sas_usg/USG/epicresponsefiles.html.

European Space Agency (29.01.2019a). XMM-Newton: A Technical Description. https://www.cosmos.esa.int/web/xmm-newton/technical-details.

European Space Agency (29.01.2019c). XMM-Newton Users Handbook. https://xmm-tools.cosmos.esa.int/external/xmm_user_support/documentation/uhb/.

Ferriére, K. (2015). Interstellar magnetic fields: from Galactic scales to the edge of the heliosphere. *Journal of Physics: Conference Series*, 577:012008.

Fioretti et al. (2016). Monte Carlo simulations of soft proton flares: testing the physics with XMM-Newton. *arXiv:1607.053191*.

Gaisser et al. (2016). *Cosmic Rays and Particle Physics*. Cambridge University Press.

Gamma-ray astronomy community Revision (13.02.2019). Data formats for gamma-ray astronomy. `https://gamma-astro-data-formats.readthedocs.io/en/latest/index.html`.

HESS Collaboration (2006). The H.E.S.S. survey of the Inner Galaxy in very high-energy γ-rays. *arXiv:astro-ph/0510397v1*.

HESS Collaboration (2011). Discovery of extended VHE γ-ray emissioin from the vicinity of the young massive stellar cluster Westerlund 1. *arXiv:1111.2043*.

HESS Collaboration (2014). Discovery of the hard spectrum VHE γ-ray source HESS J1641-463. *arXiv:1408.5280*.

Hofmann, W. (25.01.2019). The H.E.S.S. Telescopes. `https://www.mpi-hd.mpg.de/hfm/HESS/pages/about/telescopes/`.

Irrgang, A. (2018). Lecture on Principles of Stellar Evolution and Nucleosynthesis.

Israel et al. (2007). The Post-Burst Awakening of the Anomalous X-ray Pulsar in Westerlund 1. *arXiv:astro-ph/0703684*.

Joye, W. A. and Mandel, E. (2003). NewFeaturesof SAOImage DS9. *Astronomical Data Analysis Software and Systems XII ASP Conference Series*, 295:489.

Jung, I. (2016). Lecture on Data Analysis.

Kavanagh et al. (2011). Diffuse Thermal X-ray Emission in the Core of the Young Massive Cluster Westerlund 1. *arXiv:1106.2665v1*.

Kavanagh et al. (2019). Magnetic fiel estimates form the X-ray synchrotron emitting rims of the 30 Dor C superbuble and the implications for the nature of 30 Dor C's TeV emission. *arXiv:1809.01095*.

Knödelseder et al. (2016). GammaLib and ctools - A software framework for the analysis of astronomical gamma-ray data. *arXiv:1606.00393*.

Knies, J. (2019). Private communication.

Kothes, R. and Dougherty, S. (2007). The distance and neutral environment of the massice stellar cluster Westerlund 1. *arXiv:0704.3073*.

Kroupa, P. (01.02.2019). The Stellar Initial Mass Function. `http://www.cambody.org/notes/Cambody06_IMF.pdf`.

Lau et al. (2016). Interstellar gas towards the TeV gamma-ray sources HESS J1640-465and HESS J1641-463. *arXiv:1610.05444*.

Longair, M. S. (1994). *High Energy Astrophysics - Volume 2*. Cambridge University Press.

Longair, M. S. (2011). *High Energy Astrophysics - Third Edition*. Cambridge University Press.

MAGIC Collaboration (2019). Deep observations of the globular cluster M15 with the MAGIC telescopes. *arXiv:1901.04367*.

Miller et al. (2016). An Ultra-fast X-ray Disk Wind in the Neutron Star Binary GX 340+0. *arXiv:1604.03329v1*.

Ohm et al. (2013). γ-ray emission from the Westerlund 1 region. *arXiv:1306.5642*.

Oya et al. (2015). HESS J1641-463, a very hard spectrum TeV gamma-ray source in the Galactic plane. *arXiv:1509.08310*.

Parizot et al. (2004). Superbubbles and Energetic Particles in the Galaxy - I: Collective effects of particle acceleration. *arXiv:astro-ph/0405531*.

Petrosian, V. (2012). Stochastic Acceleration by Turbulence. *arXiv:1205.2136*.

Pogge, R. (11.07.2018). Lecture 17: The Evolution of High-Mass Stars. `http://www.astronomy.ohio-state.edu/~pogge/Ast162/Unit2/himass.html`.

Povh, Rith, S. and Zetsche (1999). *Teilchen und Kerne*. Springer.

Ramirez-Ruiz et al. (2001). Winds from massive stars: implications for the afterglows of $\gamma - ray\, bursts$. *Mon.Not.Roy.Astron.Soc.*, 327:829–840.

Ridpath, I. (2012). *Dictionary of Astronomy*. Oxford University Press.

Robrade, J. and Schmitt, J. H. M. M. (2006). XMM-Newton X-ray spectroscopy of classical T Tauri stars. *arXiv:astro-ph/0601234*.

Sakai et al. (2013). Discovery of Diffuse Hard X-ray Emission form the Vicinity of PSR J1648-4611 with Suzaku. *arXiv:1301.5940v1*.

Sasaki, M. (2017). Lecture on Interstellar Medium.

Shilon et al. (2018). Application of Deep Learning methods to analysis of Imaging Atmospheric Cherenkov Telescopes data. *arXiv: 1803.10698v1*.

Smith, N. (2012). Mass Loss: Its Effect on the Evolution and Fate of High-Mass Stars. *arXiv:1402.1237*.

Snowden, S. L. and Kuntz, K. D. (29.01.2019). COOKBOOK FOR ANALYSIS PROCEDURES FOR XMM-NEWTON EPIC OBSERVATIONS OF EXTENDED OBJECTS AND THE DIFFUSE BACKGROUN. `ftp://xmm.esac.esa.int/pub/xmm-esas/xmm-esas.pdf`.

Sobel, C. (2018). Development and Characterization of a Field-of-View Background Model for the High Energy Stereoscopic System.

SOC/SSC, X.-N. (17.03.2019). epatplot. `https://heasarc.gsfc.nasa.gov/docs/xmm/sas/help/epatplot.pdf`.

Stevens, Blondin and Pollock (1992). Colliding Winds from Early-type Stars in Binary Systems. *The Astrophysical Journal*, 386:265–287.

Strüder et al. (2001). The European Photon Imaging Camera on XMM-Newton: The pn-CCD camera. *Astronomy and Astrophyiscs*, 365:L18–L26.

Swinburne University of Technology (01.02.2019). Interstellar Reddenig. `http://astronomy.swin.edu.au/cosmos/i/interstellar+reddening`.

The Astropy Developers (28.02.2019). Tophat2DKernel. `http://docs.astropy.org/en/stable/api/astropy.convolution.Tophat2DKernel.html`.

Université de Strasbourg/CNRS (03.02.2019). GX 340+0. `http://simbad.u-strasbg.fr/simbad/sim-id?Ident=GX+340%2B0`.

Usov, V. V. (1992). Stellar Wind Collision and X-Ray Generation in Massive Binaries. *The Astrophysical Journal*, 389:635–648.

van Paradijs, J. and White, N. (1995). The Galactic Distribution of Low-Mass X-Ray Binaries. *Astrophysical Journal Letters*, 447:L33.

Wakely, S. and Horan, D. (18.02.2019). TeVCat FAQ. `http://tevcat.uchicago.edu/about.html#1`.

Weaver et al. (1997). Interstellar Bubbles. II. Strcuture and Evolution. *The Astrophysical Journal*, 218:377–395.

Weinstein, A. (2015). The Cygnus region of the galaxy: A VERITAS perspective. *SuGAR 2015 - Searching for the Sources of Galactic Cosmic Rays*, 105:04005.

Westerlund, B. (1961). A heavily reddened cluster in Ara. *Publications of the Astronomical Society of the Pacific*, 73:51.

Xin et al. (2018). HESS J1640-465 - A Gamma-Ray emitting Pulsar Wind Nebula? *arXiv:1802.03520v2*.

Yardley, J. (18.03.2019). The Cosmic Microwave Background. `http://planck.cf.ac.uk/science/cmb`.

Zabalza, V. (2015). naima: a Pyhton package for inference of relativistic particle energy distributions form observed nonthermal spectra. *arXiv:1509.03319*.

Ziegler, A. (2018). *A detailed study of the unidentified TeV source HESS J1826-130 in the search for Galactic PeVatrons with H.E.S.S.* PhD thesis, Erlangen Centre for Astroparticle Physics.

Acknowledgements

I would like to thank everyone supporting me during this thesis but a special thanks goes to:

- Prof. Dr. Christopher van Eldik and Prof. Dr. Manami Sasaki for giving me the opportunity to work on this amazing project in multiple wavelengths as well as for nice and fruitful discussions,
- Andreas Specovious, Domenico Tiziani and Jonathan Knies for helping me all the time regarding technical issues or answering questions,
- Lars Mohrmann for reviewing the thesis and also giving important advices,
- the whole Gamma Group for an awesome working atmosphere, having always an friendly ear for me and funny conversations,
- the people at the Dr. Karl Remeis Observatory in Bamberg for the nice discussions during lunch,
- my fiance Emanuel Freundl for supporting me all the time and being very patient when I was busy,
- my whole familiy for supporting me during my whole life and especially to my mum for believing in me that I fulfil my dreams.

THANK YOU ALL SO MUCH!

Statement of Authorship

I hereby certify that this thesis has been composed by me and is based on my own work,unless stated otherwise. No other person's work has been used without acknowledgmenting. All references and verbatim extracts have been quoted, and all sources of information, including graphs have been specifically acknowledged.

Erlangen, 28th of March 2019

Jacqueline Catalano